

# A Prototype for 3D Electrohydrodynamic Printing

*A thesis submitted in partial fulfilment of the requirements for the  
degree of*  
**Doctor of Philosophy**

By  
Shaikh Hafeez Hashimdeen

Department of Mechanical Engineering  
University College London  
Torrington Place, London WC1E 7JE  
UK



## Declaration

I, Shaikh Hafeez Hashimdeen, confirm that the work presented in this thesis is my own. Where information has been derived from other sources, I confirm that this has been indicated in the thesis.

.....  
Shaikh Hafeez Hashimdeen

**Abstract:**

Electrohydrodynamic direct writing is a flexible cost effective alternative technique that is capable of producing a very fine jet of liquid in the presence of an external electric field. This jet can then be used to pattern surfaces in an ordered and controlled fashion and offers a robust route to low cost large area micro and nano-manufacturing. Unlike other types of direct writing techniques, the liquid in electrohydrodynamic printing is subjected to both pushing and pulling forces. The pushing force is brought about by the constant flow rate that is maintained via high precision mechanical pumps while a pulling force is applied through a potential difference that is applied between the nozzle and the ground electrode and as a result a fine jet can be generated to pattern surfaces. The impracticality of use and the cost of building micrometre and sub-micrometre sized nozzles to print narrow line widths warrant an investigation into alternative means of dispensing printing inks using nozzles that are cheap to produce, easy to handle and consistent in delivery. The enormous capillary pressures that would have to be overcome in order to print highly viscous materials with micrometre and sub-micrometre sized nozzles may also limit the types of feed that could be used in printing narrow line widths. Thus, the initial work described is focused on improving print head design in an attempt to electrohydrodynamic print pattern narrow line widths using silk fibroin. This is followed by work where we attempt to design and construct of a new electrohydrodynamic printing machine with the sole purpose of expediting research in electrohydrodynamic printing in a flexible, feasible and user friendly manner. To achieve this, replicating rapid prototype technology is merged with conventional electrohydrodynamic printing phenomena to produce a EHD printing machine capable of print depositing narrow line widths. In order to validate the device the work also describes an attempt to print a fully formed human ear out of polycaprolactone. Finally, we investigate an approach to the electrohydrodynamic printing of nasal septal scaffolds using the microfabrication system that was developed and optimized in our laboratory. In these initial stages we were successful in showing the degree of control and flexibility we possess when manufacturing constructs out of a biodegradable polymer ( polycaprolactone) from the micro to macro scale through manipulation of just one process parameter (concentration). This work also features characterization of scaffold mechanical properties using a recently invented Atomic force microscopy technique called PeakForce QNM (Quantitative Nanomechanical Property Mapping).

**Publications:**

- 1) Hashimdeen S, Miodownik M, Edirisinghe M. 2013. Print head design and control for electrohydrodynamic printing of silk fibroin. *Materials Science & Engineering C-Materials For Biological Applications* 33:3309-18
- 2) Hashimdeen SH, Miodownik M, Edirisinghe MJ. 2014. The Design and Construction of an Electrohydrodynamic Cartesian Robot for the Preparation of Tissue Engineering Constructs. *PLoS ONE* 9:e112166
- 3) Hashimdeen SH, Thorogate R, Miodownik M, Edirisinghe MJ. 2015. Fabrication of bespoke nasal septal scaffolds. *Materials and Design* 90 (2016) 403–409

## **Acknowledgments**

First and foremost, I would like to thank my first supervisor Professor Mohan Edirisinghe for accepting me as a PhD research student at UCL and teaching me the art of research. His valuable guidance, continuous advice, remarkable patience and willingness to believe in my ideas contributed tremendously during my current research work.

My thanks are equally due to my second supervisor Professor Mark Miodownik for his great support, advice and enthusiasm during my work. He was always willing to help and his guidance always served to improve my work in many instances.

I am also thankful to Dr. Richard Thorogate and Dr. Philip Reardon for their invaluable assistance when characterizing my samples.

Last but not least, I would like to thank my family for their sacrifice, love, and support in numerous ways. They have worked hard to finance my studies when I struggled to pay for my own education. Their care and advice got me through rough patches over the course of the last four years. I would not be where I am today if not for them!

*To my beloved parents*

## Contents

<b>CHAPTER 1: INTRODUCTION.....</b>	<b>1</b>
1.1 Background .....	1
1.2 Aims and Objectives .....	2
1.3. Thesis Outline .....	2
<b>CHAPTER 2: LITERATURE REVIEW.....</b>	<b>5</b>
2.1 Introduction.....	5
2.2 Ink-Jet printing.....	5
2.3 Electrohydrodynamic printing .....	8
2.4 Electrohydrodynamic phenomena.....	9
2.5 The electrohydrodynamic modes .....	13
2.6 Cone-jet mode .....	14
2.6.1 Flow rate and Voltage .....	17
2.6.2 The effect of physical properties of the liquid .....	19
2.6.2.1 Electrical conductivity .....	19
2.6.2.2 Surface tension.....	20
2.6.2.3 Viscosity .....	21
2.7 The printing setup and nozzle design.....	24
2.8 Electrohydrodynamic high resolution printing through the pyroelectric effect .....	37
2.9 Electrohydrodynamic printing LCD screens.....	39
2.10 Biological applications of high resolution electrohydrodynamic printing.....	40
2.11 High resolution printing of conductive tracks using continuous jets .....	50
2.12 High resolution printing of conductive tracks, drug encapsulation using EHD drop on demand and EHDA ( Electrohydrodynamic atomization).....	52
2.13 Electrohydrodynamic atomization of ceramics and polymers .....	58
2.14 High resolution printing of transparent electrodes and meshes .....	59
2.15 Electrohydrodynamic printing of field effect transistors, ferroelectric memory devices and multi-layer interconnection structure .....	63
2.16 Electrohydrodynamic printing of Memristors.....	65
2.17 Electrohydrodynamic printing of transistors.....	67
2.18 Near field electrospinning .....	71
2.19 Mechano-electrospinning .....	74
2.19 Electrohydrodynamic jetting of melt extrusion.....	75
2.20. Scaffold design.....	79
2.21 Drawbacks of current printing technologies .....	81

<b>CHAPTER 3: EXPERIMENTAL DETAILS.....</b>	<b>84</b>
3.1 Materials .....	84
3.1.1 Regenerated silk fibroin .....	84
3.1.2 Polycaprolactone.....	85
3.1.3 Formic acid .....	85
3.1.4 Dimethyl carbonate.....	86
3.2 Solution preparation.....	87
3.2.1 Silk Fibroin Solution preparation.....	87
3.2.2 Polycaprolactone Solution Preparation.....	87
3.3 Equipment.....	88
3.3.1 The Electrohydrodynamic printer .....	88
3.3.2 The print heads.....	90
3.4 Characterisation of solutions.....	93
3.4.1 Electrical conductivity .....	93
3.4.2 Surface Tension .....	94
3.4.3 Density .....	94
3.4.4 Viscosity .....	95
3.5 Characterisation of printed products .....	95
3.5.1 Optical Microscopy.....	95
3.5.2 Differential scanning calorimetry .....	96
3.5.3 Fourier transform infrared raman spectroscopy .....	96
3.5.4 AFM peak force quantitative nanomechanical mapping.....	97
<b>CHAPTER 4.....</b>	<b>99</b>
<b>DESIGN AND CONSTRUCTION OF THE ELECTROHYDRODYNAMIC CARTESIAN ROBOT .....</b>	<b>99</b>
4.1 Overview .....	99
4.2 The Setup .....	102
4.3 Machine frame and axes .....	106
The fluid deposition .....	108
4.4 Cooling/humidity control system.....	109
<b>CHAPTER 5. RESULTS AND DISCUSSION.....</b>	<b>112</b>
5.1 Evaluation of the Print Heads .....	112
5.1.1 Reservoir, insulated shafted and pinhole print heads.....	112
5.1.2 Silk fibroin solution properties .....	119

5.1.3 Shafted and calligraphy print heads .....	123
5.2 Evaluation of the Cartesian Robot (human ear like construct) .....	126
5.2.1 Solution properties of Polycaprolactone .....	126
5.3 Evaluation of the Cartesian Robot (Nasal septal scaffolds).....	132
5.3.1 Solution properties of Polycaprolactone .....	132
<b>CHAPTER 6 CONCLUSIONS AND FUTURE WORK.....</b>	<b>144</b>
6.1 Conclusions.....	144
6.2 Future work.....	149
<b>REFERENCES: .....</b>	<b>153</b>

## Tables:

<i>Table 1: Modes of electrohydrodynamic jetting [27] .....</i>	14
<i>Table 2: Orifice dimensions of needles in each print head. In each case the needle supplying solution and generating the electric field was a shafted needle with an 800<math>\mu</math>m internal diameter. .....</i>	93
<i>Table 3: Physical properties of silk fibroin solutions used in the experiments. All % refer to weight.....</i>	119
<i>Table 4: Physical properties of silk fibroin solutions used in the experiments. All % refer to weight.....</i>	126
<i>Table 5: Physical properties of PCL solutions used in the experiments. All % refer to weight .....</i>	132

## Figures:

<i>Figure 1: A comparative illustration of the drop on demand and continuous ejection mechanisms in an ink jet print head a) piezoelectric ejection b) continuous ejection [8] .....</i>	7
<i>Figure 2: Images showing (a) a stable cone-jet [27]. (b) a geometric diagram of an axisymmetric liquid cone with a thin jet at its apex depicting forces acting on a cone-jet [35]. .....</i>	15
<i>Figure 3: Schematic of the E-jet printing setup [48].....</i>	25

<i>Figure 4: Electrohydrodynamic jet printing system designed to minimize cost (&lt;\$50,000), system dimensions, and set-up time, while maintaining high resolution E-jet printing .....</i>	26
<i>Figure 5 (a) Set-up of conventional ES apparatus with nozzle and high voltage power supply. (b) Wireless ES system made of three principle components: thermal source, LN crystal, and polymer drop.(d) Finite element simulation of sharp-cone electric field lines ((arrows) compared with (c) conventional ES field [90]. .....</i>	38
<i>Figure 6: Surface topography of PCL [99] .....</i>	44
<i>Figure 7: Schematic of an electrohydrodynamic system supplemented with a dispensing system, ethanol medium in the target bath, and a core/shell nozzle. An optical image of a single jet from the nozzle and SEM images of the deposited fibrous strut. .....</i>	47
<i>Figure 8: SEM micrographs of printed nanostructures with dimensionalities from 0D to 2D. (a) Gold nanopillar of diameter ~50 nm and aspect ratio of ~17 (Scale bar, 200 nm). (b) Top and (c) side view of nanopillars printed subsequently at 200 nm center-to-center distance (scale bar, 200 nm). (d) 80-nm wide dots printed into a 1-μm lattice constant array (1 μm scale bar). (e) Printed tracks with pitch sizes of 250, 200, 150, 100 and 75 nm (scale bar, 2 μm). The inset shows AFM(full black lines) and SEM(red dashed lines) profiles of 150-nm pitch size. The height of AFM profiles is given in nanometers. The SEM profiles are in arbitrary units. Tracks have reproducible heights of ~40 nm and are well separated [58]. ..</i>	57
<i>Figure 9: (a) Pictures of the fiber arrays realized by NF-ES. The dashed box highlights the region with nanofibers. (b)–(d) Confocal fluorescence micrograph of an array of emitting nanofibers made by NF-ES. (e) Single fiber confocal fluorescence image [164]. .....</i>	72
<i>Figure 10 : Schematic diagram illustrating the printing setup used to test the print heads ..</i>	89
<i>Figure 11: The electrohydrodynamic printer that was used to test the print heads: (a) the x, y and z axis printing stage which can move independently of the print head; (b) the print head assembly( scale bar 100mm) (c) the positions of the print head relative to the lower electrode (scale bar 100mm). .....</i>	89
<i>Figure 12: Reservoir print head: (a) in action, (b, c) design features .....</i>	90
<i>Figure 13: Pinhole reservoir print head: (a) in action (b, c) design features .....</i>	91
<i>Figure 14: Insulated shafted print head: (a) in action, (b) design features .....</i>	91
<i>Figure 15: shafted print head: (a) in action, (b) design features .....</i>	92
<i>Figure 16: Calligraphy print head: (a) in action, (b) design features .....</i>	92

<i>Figure 17: Comparison of A) intended printing path and B) actual printed path taken due to the tremors at sharp corners.....</i>	101
<i>Figure 18: The x-axis. A) internal view of the printer A(I)The X-axis and the components with respect to each other A(II) isometric view of the x-axis showing the drive belt and x-axis carriage A(III) side-on view of the x-axis showing how the stepper motor fits into the x-axis. (Scale bar =100mm) .....</i>	103
<i>Figure 19: Cross-sectional view of the printer revealing the Y and Z axis assembly within the printer. A(1) key components of Z- axis, gears, driving belt and needle holder A(II) side on view showing the positions of Y and Z axis in relation to each other. (Scale = 20mm) .....</i>	104
<i>Figure 20: The Cartesian robot. a) full setup b) y-axis cradle c) main circuit box d) cooling fan for the main circuit box e) Internal view, x and y axis positions can be seen in relation to each other.....</i>	105
<i>Figure 21: Polypropylene frame. 1) Top view showing contours of the internal box II) inward bending of wall III) floor bending downwards .....</i>	107
<i>Figure 22: Circuit diagram illustrating the connections between the microcontroller, humidifier, de-humidifier and the cooling mechanism. ....</i>	110
<i>Figure 23: The cooling/humidity control system. I) how the cooling mechanism works II) cross-sectional view illustrates the different components of the cooling/humidity control system. ....</i>	111
<i>Figure 24: A comparison of best print patterns produced by each print head as the applied voltage is increased from i) 10kV to vi) 20kV in increments of 2kV.....</i>	113
<i>Figure 25: Printed line width variation with applied voltage and silk concentration for both flow rates (1.5<math>\mu</math>l/min and 2.0<math>\mu</math>l/min). a) Reservoir print head b) Insulated shafted print head c) Pinhole reservoir print head d) Slanted shafted print head e) Calligraphy print head . The key in each graph indicates: Silk concentration in wt%, Flow Rate in <math>\mu</math>l/min.....</i>	118
<i>Figure 26:Transition in the intensity of mechanical buckling as concentration of the silk solution was increased resulting in (a) straight printed lines becoming (b) non-linear. Print head used was insulated shafted, the flow rate was 1.5<math>\mu</math>l/min and the applied voltage was set to 12kV. The silk concentration (wt %) was 15 in (a) and 22 in (b) .....</i>	121
<i>Figure 27: Print head designs tested in the work, (a) comparison of optimised silk concentration, flow rate, applied voltage and line width (b) comparison of highest resolution .....</i>	122

<i>Figure 28: The three-dimensional STL construct compared to the actual printed construct (scale bar =15mm).</i> .....	127
<i>Figure 29: The gradual evolution of the construct with respect to concentration, viscosity and density (scale bar 20mm).</i> .....	128
<i>Figure 30: A comparison of the shrinking observed in the constructs. a) width b) height</i> ...	129
<i>Figure 31: The printing operating envelope</i> .....	130
<i>Figure 32: Close up examination revealing key features of the construct. a) Live screen capture of the tool path taken during the print b) actual construct</i> .....	131
<i>Figure 33. The printing route from STL File to the final printed construct a) The three-dimensional STL construct b) Printing tool path for one layer c) The actual printed construct</i> .....	132
<i>Figure 34: A comparison of DMT modulus, deformation, dissipation, surface roughness and crystallinity (represented as Y and defined in the legend) as a function of concentration....</i>	134
<i>Figure 35. Differential scanning calorimetry traces illustrating the thermal history of scaffolds prepared.....</i>	136
<i>Figure 36: The variation in DMT modulus, deformation and dissipation for 15wt% with respect to the position along sample area. ....</i>	137
<i>Figure 37: The variation in DMT modulus, deformation and dissipation for 18wt% with respect to the position along sample area. ....</i>	138
<i>Figure 38: The variation in DMT modulus, deformation and dissipation for 23wt% with respect to the position along sample area. ....</i>	139
<i>Figure 39: A comparison of how PCL filament width (resolution) varies with PCL concentration .....</i>	140
<i>Figure 40: Typical two and three dimensional depictions of the height variation, DMT modulus and surface topography of the scaffolds prepared .....</i>	141
<i>Figure 41: The nasal septal scaffolds printed shown at different length scales.....</i>	142
<i>Figure 42: FTIR spectra highlighting key peaks detected.....</i>	143

# CHAPTER 1: INTRODUCTION

## 1.1 Background

The drive towards smaller, multifunctional, energy saving devices without compromise to quality and reliability has led many micro and nano fabrication industries to look for innovative and inexpensive direct fabrication techniques to meet the competition and allow for globalisation. These novel techniques are used to create electronic sensor devices and integrated power sources within the meso-nanoscale range. The process of depositing, dispensing or processing of different materials onto substrates according to a pre-defined pattern or layout is known as direct writing. As a consequence of the ability of direct-write to achieve both pattern and material transfer simultaneously, the process represents a change in the way integrated devices have been traditionally manufactured through lithographic means. This coupled with the extreme precision with which multiple materials can be dispensed to create functional devices or structures underpins the immense potential of the various direct write techniques.

Direct write technologies are revolutionising manufacturing processes across a broad range of industrial sectors by putting greater flexibility into the production process thus enabling product modification for the customisation of individual products in real time. Dedicated chemical vapour deposition systems, sputtering chambers, photolithographic techniques can be effectively eliminated so that electronic components and devices can be manufactured in high volume within clean environments under ambient conditions. They also offer lower development costs and improved inventory control. Manufacturing can take place without wastage and only when required. Re-tooling or mould re-shaping complications are

effectively eliminated. The printed products can reach the market much quicker because dedicated machines can be used to produce specific parts that have been ordered by the customer. It moves production to a more local environment and therefore directly impacts the supply chain bringing about a direct cost savings. Labour is no longer what makes production important but technical ability and skill takes prominence in better product design and performance with novel functionality.

## **1.2 Aims and Objectives**

The main goal of this project is to optimize a 3D printer for stable, high resolution electrohydrodynamic printing purposes. To achieve this three systematic progression objectives were set out

- 1) Optimize needle design for print depositing narrow line widths
- 2) Design and construction of a cheap, user friendly desktop 3D printer
- 3) 3D printing of simple structures

## **1.3. Thesis Outline**

### **Chapter 1:**

Introduces the project background with a brief historical overview and the impact of the direct writing technologies. Also the aims and objectives of this project are described.

## **Chapter 2**

Gives a literature review covering the fundamental principles and aspects of the various direct writing techniques that are presently in the market and their applications. A description of the physics governing electrohydrodynamic phenomena is discussed. This includes a description of the process parameters (voltage, flow rate) and solution parameters (surface tension, viscosity, electrical conductivity) that influence the phenomena. This is followed discussion on how electrical components are fabricated through EHD printing means with a particular emphasis on the effect of resolution on component performance. Biological applications of EHD printing are equally described.

## **Chapter 3**

In this chapter the materials and methods used for the experiments performed in this work are being described. The details about the materials (corresponding suppliers and properties) as well as the methods used to characterize the materials and solutions are reported. This is also includes details of the five print heads that were constructed for the study as well as the CNC printer that was used to print the lines.

## **Chapter 4**

Describes the design and construction of a 3D electrohydrodynamic printer that uses Rapid Replication technology. This includes a description of the electronics used to control the printer and the print process. Customized enhancements pertaining to the printer frame are outlined for the ideal functioning of RepRap technology in conjunction with EHD phenomena.

## **Chapter 5**

A description of the test results followed by an in depth discussion of the findings from all three studies.

## **Chapter 6**

Summarizes what has been achieved with this study and describes the future experimental plans.

## **CHAPTER 2: LITERATURE REVIEW**

### **2.1 Introduction**

Research in the biomedical field usually requires technology capable of rapidly depositing fixed volumes of liquids precisely onto flat substrates with varied geometries such as microwells which can be used for parallel experimentation in drug screening and gene activation. Ink-jet printing is a powerful technique that affords the user the ability to precisely deposit pre-determined amounts of functionalized materials on a variety of substrates to create either two dimensional surface features or three dimensional structures. Thermal, electrostatic or acoustic mechanisms are used to dispense droplets that are larger than the nozzle size [1-3]. The technique is able to handle pico-litres of samples efficiently and without wastage and is thus used widely in the fields of combinatorial chemistry and biology. The low risk of contamination coupled with gentle working conditions have led researchers to investigate its use in tissue engineering, in particular organ and cell printing [4-7]. This efficient handling of minute biological samples also allows the technique to print enzymes, micro-organisms and anti-bodies to create a variety of biological devices and functional biosensors, bioMEMs being the most popular one.

### **2.2 Ink-Jet printing**

Drop on demand inkjet printing exists in two different forms, thermal drop on demand and piezoelectric drop on demand. The inkjet cartridge used in most printers is a highly technical component of the inkjet system that features a highly integrated circuit that routes signals to the appropriate nozzles with high precision. In thermal drop on demand, each ink drop is

propelled by a short lived super-heated vapour explosion that lasts about  $2\mu\text{s}$  induced by a heating element inside the print head. Once the explosion collapses it draws more ink from the reservoir. The print head accurately and reliably delivers up to 36000 drops per second from each of the print heads microscopic nozzles. The small ink drops allow for accurate droplet placement up to 32 ink drops per colour drop on the substrate. The main drawback of the technique lies in the nature of solvent that could be used for printing. The solution should contain a volatile ingredient or be itself volatile to create a heated vapour explosion [8].

Similarly material transfer through the controlled deposition of a series of droplets generated by the application of a temporary undulating pressure induced by a piezoelectric actuator is called piezoelectric drop on demand inkjet printing. The droplets are created when they are required so material wastage is minimised. Subsequent processing steps on the deposited material as the solvent evaporates are possible. This printing technique usually functions with an array of tiny nozzles on the main print head, each firing when required [8].

Continuous inkjet print heads always have a continuous stream of ink running through the print head. This type of direct writing exploits the Plateau-Rayleigh instability to create a steady stream of droplets through the disruption of a continuous jet as it leaves the nozzle due to the action of surface tension forces. This disruption is initiated and assisted through cyclic agitation introduced by a piezoelectric transducer that is in contact with the ink in the main chamber operating at frequency of about 75 kHz. Droplets with a diameter twice that of the jet are generated and then made to pass through a charging electrode that charges each droplet. The charged droplets are then deflected to their designated positions on the substrate

by an electric field created by the deflectors. Drops that fail to be deflected are collected in a gutter and recycled back [8].

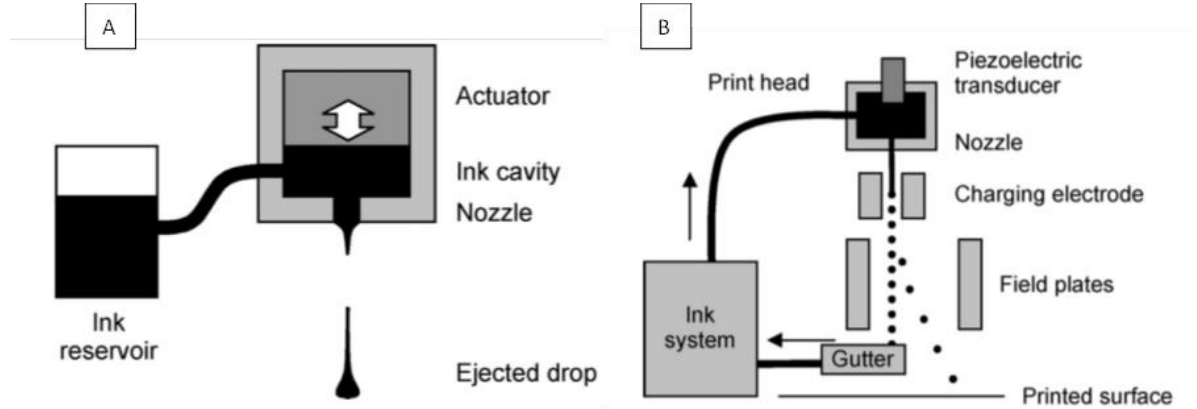


*Figure 1: A comparative illustration of the drop on demand and continuous ejection mechanisms in an ink jet print head a) piezoelectric ejection b) continuous ejection [8]*

The limitations of the technology depend and vary on the mechanism of droplet generation. The resolution, range of shear forces within the nozzle and the rheological properties of the ink used are some of the key limitations. In conventional ink-jet printing, low viscosity ink (less than 30 mPa s) is used to allow for stable flow through the nozzles without the risk of clogging. In terms of resolution, the inkjet printing technique is limited to dispensing the printing solution in the form droplets that are in the range of tens of micrometres. Similarly the nozzle dimensions need to be sufficiently large enough to allow for particles, macromolecules and isolated cells used in the ink to flow through the aperture without accumulating at the orifice [9, 10]. These drawbacks have led researchers to techniques like electrohydrodynamic (EHD) jet printing as a solution to the problems.

## 2.3 Electrohydrodynamic printing

Electrohydrodynamic printing is a new and versatile non-contact direct fabrication technology that is capable of printing at a much higher resolution when compared to conventional ink jet printing [9]. This is made possible by virtue of a large ratio of jet diameter to nozzle diameter which is achievable when an electric field is used to pull out thin continuous micrometre sized jets from a meniscus suspended from the end of the nozzle in the cone-jet mode [11-14]. The two main process control parameters of electrohydrodynamic printing are the applied voltage which is directly proportional to the electric field and the flow rate of the material to be printed, a solution or a suspension of it. The flexibility and processing speed of the technique allows it to compete on cost with conventional lithographic patterning techniques with deposited resolutions reaching the submicrometre and nano-scale dimensions [9].

High resolution printing machines are at the forefront of most fields of flexible electronics and bioengineering. Choi and Smith were the first ones to patent EHD printing technology in 1998 under US Patent 5838349 (Natural Imaging Corporation). Initial work outlined in this patent described its use for dispensing inks of different colours into even patterns which could be easily attempted by conventional 2-dimentional inkjet printers could easily do this at the time. They did not fully discuss the possibility of using this technology for high resolution droplet formation using different materials. The first considerable leap in this direction was made in January 2009 when researchers at the University of Illinois were awarded a patent (WO2009/011709) for designing and manufacturing a high resolution EHD

printing machine that was capable of printing a variety of functional devices at submicron resolutions.

## 2.4 Electrohydrodynamic phenomena

Since the turn of the last century, electrohydrodynamic phenomenon has been documented and has attracted considerable interest from a fundamental point of view. The pioneering work by Zeleny in 1914 [15] with a needle carrying liquid and a ground electrode set up subjected to a high voltage that marked an important breakthrough into this exciting field of research. However, the existence of the steady state mode has not been satisfactorily explained and reported until 1964 [16]. Taylor initially derived the conditions necessary for a meniscus to exist in equilibrium while still maintaining the conical configuration due to the competing forces of electric field and surface tension. He then went on to investigate the break-up of a droplet by using glycerine and glycerine-water mixture when an electric field is applied to the capillary tube carrying the liquid. He established that the liquid does not vibrate before spraying but would rather adopt a conical shape when a liquid possess conductivity. He also measured the conical shape to be having a sharp tip at a semi-vertical angle that identified to be equal to  $49.3^{\circ}$ . This has since then been referred to by the technical term ‘Taylor Cone’. This is the angle at which a conical meniscus of a conducting liquid can exist in equilibrium under an applied electric field.

Since then, a number of studies were carried out to investigate the influence factors to this steady state mode aiming at utilizing this phenomenon as a processing technique. [17] found

that electrical dispersion of a jet of kerosene into spray of monodisperse droplets could only be achieved within a certain range of applied voltage and the droplet size is almost independent of voltage however a function of liquid flow rate. Studies in [18] stated that the steady state mode only exist if the conductivity of the liquid between certain limits. Later in 1980, it was found that the decrease in droplet diameter can be achieved via increasing the applied potential by [19]. This finding suggested the necessary conditions for producing smaller droplets. Furthermore, [20] carried out a study on the effect of the liquid physical properties, such as conductivity, surface tension and viscosity, on the process, which will be discussed in the following sections in details.

Based on the previous pioneered studies, more systematic and quantitative studies were carried in 90s. The classification of functional modes of electrohydrodynamic processing was described by [21]. For constant liquid properties and flow rate electrohydrodynamic processing presents through several visual and measurable differences with increasing applied voltage. These differences were defined as spray modes; the particular spray mode achieved depends on the operation conditions. They also described the specific characteristics of each mode. Thereafter, [22] characterised and defined the modes of electrohydrodynamic processing, which provide the fundamental science for utilizing such phenomenon as a deposition technique that is used in the biomedical engineering.

[23] described a set of scaling laws that refer to the innate pulsation of a liquid jet that takes shape at the very end of sharp needles under fluid flows that are electrohydrodynamically induced. They also pointed out when the print head was positioned in either the horizontal or

vertical configurations; the effect of gravity played a minor role when compared to the other overriding effects of forces like the surface tension and tangential electrical stresses. The break-up of the jets into different droplet sizes can be regulated through the fluid flow rate, applied potential difference, needle dimensions and alignment. Also included, are the standoff height (distance from the substrate), the printing ink's rheological and electrical properties. These are known as the process parameters.

The scaling laws are established for characterising a defined electrohydrodynamic processing. It enables the produced droplet size and emitted current to be better correlated with the factors involved in the processing. It provides better understanding of the mechanisms involved in the process. Basically, the droplet size and the emitted current are given by liquid physical properties (electrical conductivity, density, viscosity, surface tension and dielectric constant) and liquid flow rate.

The scaling laws derived by [24] and [10] well correlate the liquid physical properties with the droplet size and emitted current. Before stating these scaling laws, the conditions for classical electrohydrodynamic processing to take place are given below. This is the inequality criteria established by [10]. They established the criteria that the hydrodynamic time ( $t_h = LD^2/Q$ ) should be much greater than the electrical relaxation time ( $t_e = \beta \epsilon_0 / k$ ) as a condition that should be satisfied to have a steady state cone-jet structure.

$$t_h \gg t_e$$

$$LD^2/Q > \beta \epsilon_0 / k$$

Where  $Q$  is the flow rate,  $D$  is the jet diameter and  $L$  is the axial length of the jet.  $\beta$  is the relative permittivity while  $\epsilon_0$  and  $K$  are the vacuum permittivity and electrical conductivity.

Consequently, the liquids having electrical relaxation time higher than the hydrodynamic time cannot be electrohydrodynamically processed unless their electrical relaxation time is modified well below the hydrodynamic time with the use of some additives [10]

Research work by [25] attempted to outline ideal operating regimes by optimizing six dimensional parameters using model Newtonian fluids (ethanol, terpineol) that would enable users to achieve the cone-jet mode consistently for a fixed needle diameter of (300 $\mu\text{m}$ ) and length (25mm). They pointed out that the supplied flow rate played a vital role in maintaining steady jetting and in turn was dependant on the properties of the fluid. Numerical simulations were used to determine cone-jet stability by computing the electrical normal and tangential stresses ( $\tau_{E,n}$ ) ( $\tau_{E,t}$ ) on the charged meniscal surface of the cone. The findings pointed to a possibility for a ratio of the normal and tangential electrostatic forces to be used as a new parameter in determining jet stability.

For conventional electrohydrodynamic jetting to be established the fluid flow process must be sufficiently slow such that any intermediate state can be considered as an equilibrium state. This permits short electrical charge relaxation times and hence the condition of  $T_e/T_h < 1$  is possible. The thickness of this meniscal charge is referred to as the charge relaxation length which is replenished by charge conduction determined by the dielectric and conductivity properties of the printing ink. The charge relaxation length and the applied voltage were

pointed out to be key factors in cone-jet stability. They also suggested that it was possible to predict the diameter of the cone jet by using the charge relaxation length since both values were near unity in the cone jet mode. The material properties can thus be manipulated to adjust the charge relaxation length which in turn affects the jet diameter and hence the eventual printing resolution thereby offering the user a route to predicting printing resolution from the material properties.

## 2.5 The electrohydrodynamic modes

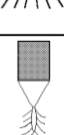
A number of studies have endeavoured to define criteria to categorize the different modes of EHD spraying. Work shown in [26] investigated the several ejection modes by direct-current pulsed electrohydrodynamic printing using diethylene glycol. The modes of electrohydrodynamic processing are characterised and defined by two criteria [27]:

- (1) The geometrical form of the liquid at the outlet of the capillary (drop, spindle, jet)
- (2) The type of the jet behaviour in its disintegration into droplets

Based on such criteria, the spraying modes can be divided into two groups. The first group comprises of the modes in which only fragments of liquid are ejected from the capillary without a continuous jet, including the dropping, micro-dripping, spindle, multi-spindle, and ramified-meniscus modes. The second group belongs to the modes, in which the liquids characteristically issues a capillary in the form of a long continuous jet which disintegrates into droplets after travelling to a distance, usually a few millimetres. The stable cone-jet, precession, oscillating-jet, multi-jet and ramified-jet modes are included in this group. The meniscus and the jet can be stable, vibrate, and rotate spirally around the capillary axis in the

second group. For the purposes of EHD printing the cone jet mode or microdripping mode are usually considered.

*Table 1: Modes of electrohydrodynamic jetting [27]*

Dripping mode		Cone-jet mode <i>(Ideal for EHD Printing)</i>	
Microdripping mode		Oscillating-jet mode	
Spindle mode		Precession mode	
Multispindle mode		Multijet mode	
Ramified-meniscus mode		Ramified-jet mode	

## 2.6 Cone-jet mode

The bulk solution in the meniscus is electrically neutral but as the applied electric field strength increases, more ions arrive and the surface charge builds up. The droplets that form and break off then start to morph into spindle shaped projections with a small jet disrupting into smaller droplets. This is known as the spindle mode and appears only in some solutions. The build-up of charges results in columbic repulsion between mutually repulsive ionic charges which in turn introduce tangential electrostatic stresses on the hemispherical meniscus which compete with opposing surface tension forces that try to restore the original hemispherical shape. Once the electrostatic forces overcome the opposing surface tension

forces, the meniscus distorts into a conical shape from which a thin jet emerges. This change is referred to as the cone-jet transition.

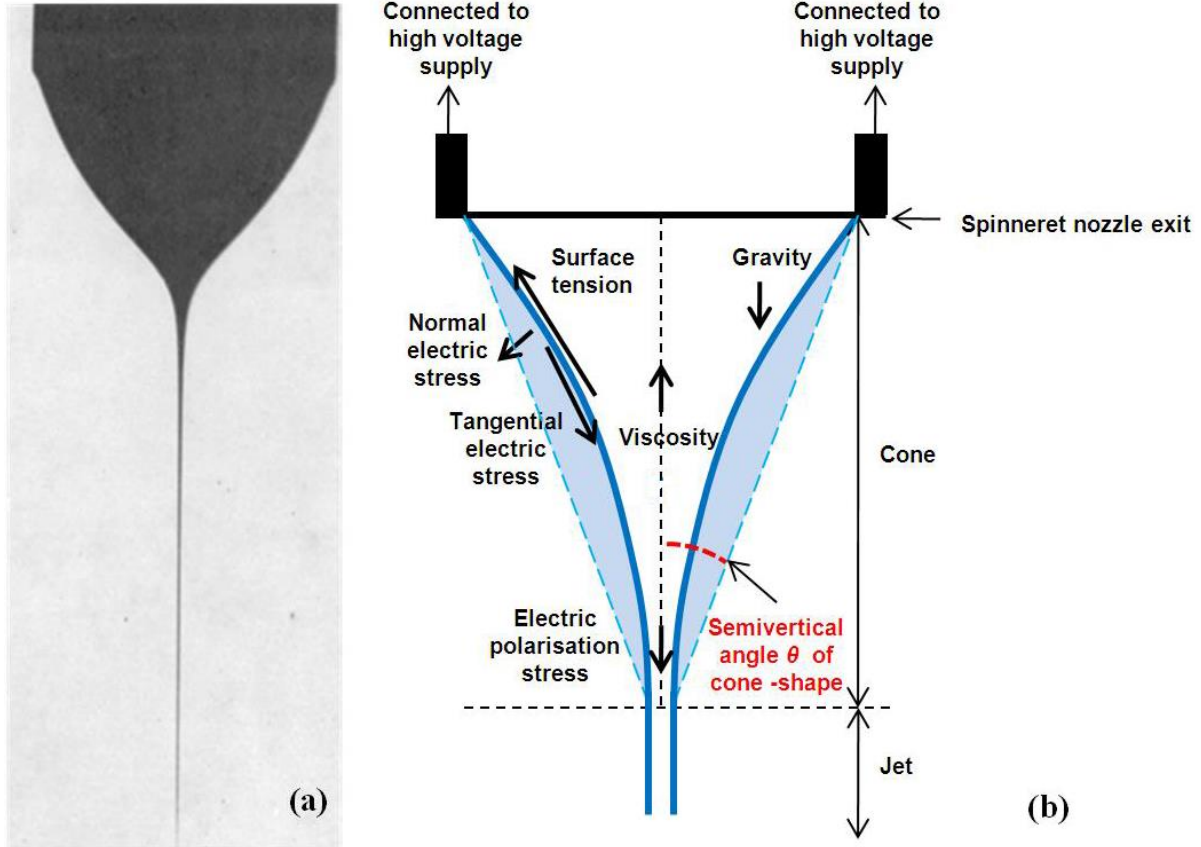


Figure 2: Images showing (a) a stable cone-jet [27]. (b) a geometric diagram of an axisymmetric liquid cone with a thin jet at its apex depicting forces acting on a cone-jet [35].

With the increasing applied voltage, a stable cone-jet mode can be achieved from the unstable cone-jet mode. In such mode, the liquid issues from the capillary in the form of a regular, axisymmetric cone with a thin jet (10 – 100  $\mu\text{m}$  in diameter) at its apex, stretching along the capillary axis [27]. The end part of the jet undergoes instabilities of two types, varicose and kink. In the case of varicose instabilities, the waves are generated on the surface of the jet, but the jet does not change its linear position. The wave contracts in the nodes, and the jet disintegrates into droplets, which further flow close to the capillary axis. In the case of kink

instabilities the jet moves irregularly off the axis of the capillary, and breaks up into fine droplets due to electrical and inertial forces. The aerosol is spread out off the axis, but nearly uniformly in the spray cone of the apex angle of about 50 - 60°.

The jet remains stable on the length of a few millimetres from the capillary exit due to the weak lateral electric field. The field generated by sprayed droplets is nearly symmetrical and the lateral forces on the jet remain the equilibrium. The space charge in the cone-jet mode is much more stable than in other spraying modes since the droplets are smaller and of lower mobility, which is one of the most attractive advantages of such spraying mode.

Hartman and co-workers established a physical model to assist the understanding of the stable cone-jet mode of the electrohydrodynamic process [28]. In this model, the stable cone-jet mode has been divided into three stages: (1) Acceleration of the liquid in the liquid cone; (2) jet break – up (Droplet production); (3) evolution of spraying after droplet production. The stable liquid cone is formed as result of the balance of liquid pressure, liquid surface tension, liquid viscosity, gravity and electric stresses in the liquid surface. This conical shape (also called Taylor cone), which balanced the surface tension and the electric stress, was firstly analytically calculated by Taylor in 1964. A Taylor cone forms when the outward stress due to applied electric field balances the inward stress due to liquid surface tension. The main drive of the cone-jet mode formation is the electric force, and therefore electric field. Thus the creation of a permanent stable jet requires a penetration of the electric field lines in the liquid, therefore the liquid must not be a perfect conductor. Only this penetration allows the appearance of a component of the electric field tangential to the liquid surface,

which is acting on the surface charges, creates a force which drives the liquid and accelerates the jet downstream [21].

### **2.6.1 Flow rate and Voltage**

Electric field and applied voltage share an intricate relationship. Increases in electric field strength causes the cone to contract back into the nozzle but does not reduce jet diameter. The jet diameter which is directly related to the resolution of printing can be manipulated by changing the flow rate at which the ink is pumped. High flow rates lead to a higher flow of charges to the meniscus which compromises jet stability. The same effect on jet stability can be seen at low flow rates and high electric field strengths.

The jet break-up process is also called droplet production process in electrospraying [28]. There are two mechanisms that can lead to the emission of liquid from the tip of a Taylor cone. In one mechanism, ions, neutral atoms and droplets are emitted from the liquid surface due to instabilities brought on by the intense electric field at the tip or in the other mechanism; liquid is ejected via the formation of jet of liquid which breaks into droplets after some length due to surface instabilities [29]. The second mechanism is most commonly observed. At the bottom of the cone, the charges are mainly conducted through charge convection. All conductive solutions have a minimum flow rate below which a stable cone-jet mode cannot be achieved. At this minimum flow rate the jet breaks up due to axisymmetric instabilities. The instabilities are also called varicose instabilities. At high flow rate, the current through the liquid cone increases. With increasing current, the surface charge on the jet also increases. Above a certain critical surface charge density the jet break-up will also be

influenced by lateral instabilities of the jet. These instabilities are also called kink instabilities.

The instabilities negatively impact the droplet size distribution by bringing about a more heterogeneous distribution as the effects become greater [30], which is preferable for processing uniform coatings. There exists a minimum and a maximum flow rate for each given applied voltage that seems to be related to the meniscus stability. The stable cone-jet mode morphs in to the multi-jet mode when the flow rate is below the minimum flow rate, and also may change to microdripping mode when the flow rate is above the maximum value at the certain applied voltage [31]. Such characteristics determine that the stable cone-jet mode can only be achieved within well-defined flow rate ranges for a specific liquid, beyond which other electrohydrodynamic modes will manifest. This is the mode that is of most use in most applications related to electrohydrodynamic direct writing. The main reason being that the jet produced is about two orders of magnitude smaller than the needle orifice and as a result paves the way for high resolution patterning of substrates.

Ironically the technique's main strength is also its main drawback in terms of jet stability. Maintaining and controlling jetting in the cone jet mode is challenging and prevents EHD printing from being applied in a commercial setting. Varicose and whipping i.e, axisymmetric and non-axisymmetric instabilities and capillary break-up limit the use and effectiveness of the technique. Significant gains have been made recently by [32] in controlling capillary jets of glycerol and polyethylene oxide (PEO) through the partial neutralization of the surface charges on the jets brought about by the ionization of the gas in the immediate vicinity of the

cone-jet. They also reported that the ions produced had a contribution to the final measured current values at the counter electrode [32-34].

## **2.6.2 The effect of physical properties of the liquid**

As afore-introduced, apart from the processing parameters, such as flow rate and applied voltage, the physical properties of the liquid also have a big impact on achieving the stable cone-jet mode. The following sections are going to discuss the effect of the core physical properties of the liquid on the stable cone-jet mode electrohydrodynamic processing to pave the way towards the systematic investigation of utilizing such technique for biomedical applications.

### **2.6.2.1 Electrical conductivity**

Electrical conductivity is the most important liquid physical property in controlling both the stability of the cone-jet mode when printing or electrospraying. For the hemispherical meniscus at the nozzle capillary exit to deform into a conical shape, sufficient electrical conductivity in the liquid is necessary. If the electrical conductivity is too low it cannot be processed in the stable cone-jet mode as there is not enough charge build up in the liquid. If it's too high the processing is not possible as the electrical discharge (corona discharge due to the surrounding air) would occur before attaining the required applied voltage for the stable cone-jet mode [35]. A number of studies have been carried out on the effect of such liquid property. Findings in [17] and [18] suggest that the liquid electrical conductivity required for stable electrospray can vary in the range of  $10^{-3}$   $\text{Sm}^{-1}$  to  $10^{-5}$   $\text{Sm}^{-1}$ . Liquids with low

conductivity (insulators), e.g., olive oil, cannot be subjected to electrohydrodynamic atomization, although they can be electrosprayed in cone-jet mode by artificially increasing their conductivities with additives such as ethanol [36].

This phenomenon was explained by Cloupeau and Prunet-Foch in 1989 [30]. They stated that the electrical conductivity is the most important for the stable cone-jet mode electrohydrodynamic processing since a liquid with too low conductivity cannot be atomized due to lack of tangential stress caused by the charges. This was established as the driving force responsible for forming the jet. Their investigation proved that electric conductivity as the most important physical property in maintaining the stability of the cone-jet when electrospraying or EHD printing.

#### **2.6.2.2 Surface tension**

In order to form and maintain a stable cone-jet mode, the surface tension has to be overcome by the electric stresses. The higher the surface tension, the more intense an electric field (higher applied voltage) is required. In doing so, there is a greater probability of electrical discharge occurring as the surrounding air is ionized in the presence of a highly intensified electrical field. The onset applied voltage for the stable cone-jet spray increases as the surface tension of liquid increases [20]. The stable cone-jet mode may not be achieved when the liquid surface tension is too high, as the electric field required exceeds that for the electric breakdown in the gas surrounding the cone [37]. Typical surface tension values of printing inks that can be used can range from  $0.022\text{-}0.073\text{ N m}^{-1}$ .

### 2.6.2.3 Viscosity

With regards to the drop on demand electrohydrodynamic printing technique, viscosity is a vital liquid property which plays a significant role in the jet break-up (droplet formation) process and influence the droplet size. An increase in viscosity can lead to a lower dominant wave number, and the lower dominant wave numbers will lead to the increase of the droplet size in electrohydrodynamic processing [38]. It was found that liquid viscosity significantly influences the number of satellite droplets. During droplet formation process, the high viscosity had been demonstrated to be important in two aspects. First, high viscosity enhances the damping of the initial oscillations of the interface remaining meniscus at the capillary immediately following the detachment of the previous drop. Second, viscosity plays a key role in keeping the primary droplet nearly spherical in shape as it's detaching from the capillary. Furthermore, investigations were carried to study the effect of viscosity on the relic size produced by electrohydrodynamic processing by [39] [40] [41]. Typical viscosities of printing inks that can be used can range from 0.4-1500 mPa s .

Work described in [42] studied how the electrohydrodynamic jets are affected as a function of the pulse voltage shape using low viscosity solutions. They were able to identify and conclude that in the case of drop on demand printing applications the fall in voltage to zero after reaching the maximum applied voltage bias needs to happen instantaneously without any delay in time before the next pulse initiating signal in order to maintain a stable pulsatile jet. Consequently, the time taken for the voltage to increase from zero to the maximum allowed voltage bias brings about a measured increase in the meniscal height as it deforms

and elongates. The use of long voltage rising times leads to a longer time period for each pulse wave and thus a lower frequency of jetting. The part of the voltage pulse where the maximum applied voltage is maintained is known as the  $t_{\text{dwell}}$  and can neither be too short ( $<100\mu\text{s}$ ) or too long ( $>1000\mu\text{s}$ ). If  $t_{\text{dwell}}$  is too long, the ink will drip intermittently without resuming pulsatile mode. On the contrary, if  $t_{\text{dwell}}$  is too short, no jetting will be possible and hence a compromise needs to be achieved to effective pulsatile jetting which they outlined in their published work in form of a range of  $t_{\text{dwell}}$  times. Based on their findings, the ideal  $t_{\text{dwell}}$  time recommended is  $300\mu\text{s}$ . They also suggested the use of  $t_{\text{dwell}}$  times as an effective means of increasing jetting frequency by reducing the time spent on that particular segment of the wave pulse. Additionally, when choosing values for  $V_{\text{pulse}}$  and  $V_{\text{dc}}$ , Kye-Si Kwon et al determined that stability was achievable only when the  $V_{\text{pulse}}$  was 1.2–3 times greater than the  $V_{\text{dc}}$ .

Studies by [43, 44] investigated if it was possible to modulate the cone jet in a cyclic manner through a series of interruption caused by superimposing a pulsed voltage on to a dc voltage bias. In doing so they showed that the superposition of the pulsed voltage brought about a periodic shrinking of the meniscus but did not prevent a stable cone jet from forming. The cyclic perturbation was of importance in drop on demand printing as it offered a route to control space distribution of the droplets produced which in sequence leads to better control over the distribution of droplet relics. Work described in [45] studied the height of the meniscus as a function of the each timed pulse sequence to understand meniscus deformation while droplet ejection was investigated by varying the pulse voltages and frequencies. They pointed out that increasing the frequency brought about a decrease in the droplet size under

the same applied voltage conditions but for an increase in pulse voltage, the droplet size increased at low frequencies and decreased in size at high frequencies.

Investigations by [46] studied how ethanol, diethylene glycol and octanol with various concentrations of dissolved aluminium particles ranging from 1-10% behaved in response to applied pulsed voltage. They determined that drop generation was mainly influenced by the electrical and rheological properties of the inks rather than the concentration of the micro-sized aluminium particles. An increase in applied voltage brought about a reduction in droplets generated while an increase in voltage frequency led to higher droplet velocity. The droplets also detached completely from the meniscus at shorter lengths from the meniscus at higher frequencies. Solvents such as diethylene glycol with a high viscosity and surface tension experienced complete droplet detachment further away from the meniscus when compared with solvents such as ethanol. They struggled to produce a steady continuous stream of droplets with the solvent octanol and this was attributed to the incongruous surface tension (27.6 mN/m) and viscosity (8.4mPa s) properties of the solvent for steady droplet generation. They also pointed out that very low viscosity and surface tension solvents were more receptive to droplet generation and as a result were more likely to form satellite droplets and relicts upon impact with the substrate. Equally, solvents with high viscosity and surface tension were less responsive to the applied pulse voltage due to a dampening effect. Drop on demand investigations by [47] using ethylene glycol with dissolved methylene blue revealed that for regular droplet generation the pulse duration needs to be longer than the characteristic time for the formation of a Taylors Cone.

## 2.7 The printing setup and nozzle design

A surge in demand for high throughput in the design and manufacture of complicated parts in a highly precise manner has paved the way for the development of advanced machinery that facilitates precision, control and consistency in production of these components. Computer Numerically Controlled (CNC) machines employ the use of advanced electromechanical systems that work synergistically to achieve this purpose. The hardware required to make this technology a reality has been gradually developing over the course of the last 30 years since the advent of the personal computer.

A typical electrohydrodynamic printing setup consists of a chamber that holds the printing ink, a pressure supply that could either be mechanical or gas assisted, a conductive printing head that is connected up to high voltage supply and finally a conductive substrate which is controlled by a cartesian positioning system. For E-jet printing, an applied voltage potential is generated between a conducting nozzle and substrate. The investigation carried out in [48] involved custom building their electrohydrodynamic printer using off the shelf parts in an attempt to reduce costs and produce a cheap desktop EHD printer. It consisted of an electronic positioning system for the x and y axes while the z- axis was kept manual. The printing ink was pumped to the nozzle via back pressure that is applied by the pressure pump while the substrate is kept in place by a vacuum pump that acts as the mount for the substrate. Images are provided via high resolution camera that is attached to a rotary axis with a fibre optic light source. The entire setup sits within a breadboard glass chamber. The design included further customizations like a multi-nozzle holder that enables multiple inks to be

printed. The holder sits on a rotary axis that can be manually adjusted to change the ink to be printed. Each nozzle on the holder has an independent high voltage electrical connection.

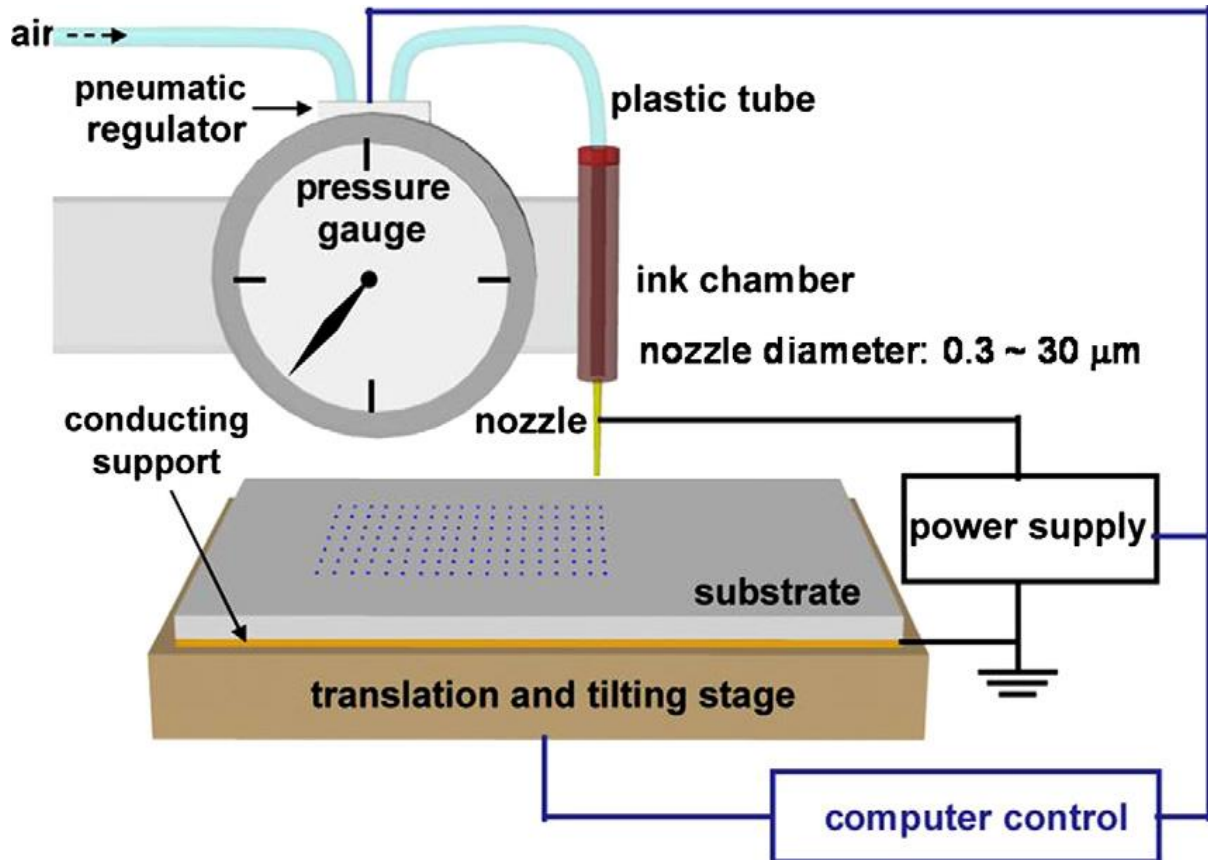
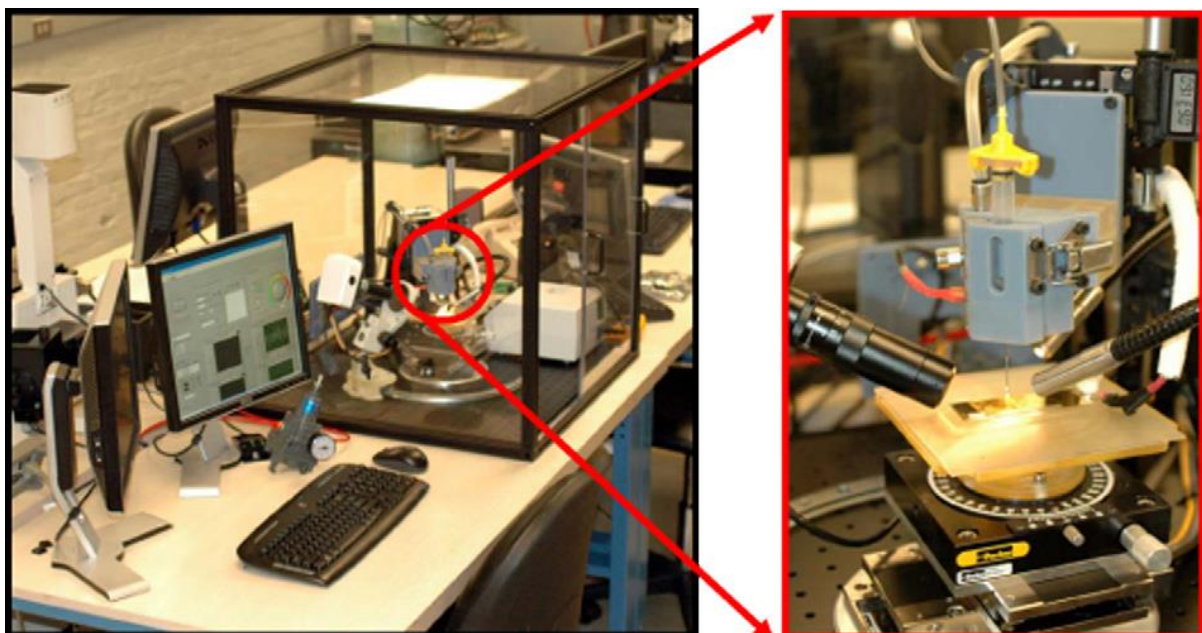


Figure 3: Schematic of the E-jet printing setup [48]

A micro-pipette with diameters that range from 300nm to 10 $\mu$ m was connected to a leur lock syringe to dispense the printing ink. The micro-pipette tip has a metal coating to ensure good electrical conduction along the micro-pipette while a hydrophobic coating prevents the printing ink from being drawn along the pipette through capillary action. The work in [49] demonstrated how the multi-nozzle could be used to dispense multiple optically unique materials to create optical waveguide multiplexers, refractive index diffraction gratings and

microlens arrays. The high voltage amplifier that was used to generate the high electric fields needed to create the fluid flows necessary for electrohydrodynamic printing was connected to linear positioning system through a Labview software which was designed to integrate both systems. The two systems can be controlled by the user through graphical user interface where the user is able to control the hardware components as well as monitor the applied voltage between the nozzle and the substrate. [50, 51] investigated the deposition characteristics of an array of double and triple nozzles on near field electrospun nanofibers. Their findings showed that the polar identical, mutually repulsive jet depositions from both needles widen as the spacing between the needles increased. Similarly increasing the standoff height and the applied voltage contributed to the lateral dispensing of fibres on the substrate.



*Figure 4: Electrohydrodynamic jet printing system designed to minimize cost (<\$50,000), system dimensions, and set-up time, while maintaining high resolution E-jet printing*

Work attempted by [52] used a similar setup but they had a three axis motorised positioning system with a pressure regulated pneumatic syringe that is capable of delivering the printing

ink at pressure of up to 5 psi. The setup also included a vibration isolation table to reduce vibrational noise. The axes on the printer are capable of 100nm minimum translations in all three directions on a stage with a 100 × 100 × 50mm printing area. They also used an aluminium coated borosilicate glass capillary with an inner bore diameter of 250 $\mu$ m as the nozzle for printing. A function wave form generator was used to produce the modulated ac voltage. [53] designed and constructed a desktop EHD printer that merged EHD phenomena with the popular open source Replication Rapid prototyping technology (RepRap). They also made an attempt to reproduce a replica of the human ear using polycaprolactone.

Researchers in [54] used nozzles 2  $\mu$ m and 500 nm glass capillaries for their experiments. The nozzle was made conductive with 30nm layer of gold/palladium adhesive along with a 50nm gold coating. To prevent the external parts of the glass capillary tip from getting wet with printing ink a hydrophobic self-assembled monolayer (1H,1H,2H,2H-perfluorodecane-1-thiol). They used also used compressed air to pump the liquid at 2psi to the tip of the glass nozzles. They used air- bearing translational stages that are driven by noncontact linear brushless motors to minimize friction through the use of air bearings to ensure that small steps are taken accurately and at a smooth velocity. A cooled CCD camera (Infinity 3, Lumenera Corp.) and long working distance optics provided an ability to view the printing process at high magnification.

Work done by [55] showed that hardware modifications need to be made to optimize the printing process for specific purposes. While using the drop on demand process to fabricate patient specific drug units they used an insulating inner electrode encased within an outer

conductive nozzle thus effectively preventing electrochemical reactions from taking place at the fluid-electrode interface. Under gentle pressure the drug loaded solution is pumped to the tip of the nozzle until it forms a drop. The pressure is intentionally kept low to avoiding the dripping mode. Upon application of a pulse which consists of two symmetrical phase alternating short signals, the drop extends towards the substrate and forms a liquid bridge. This bridge is unstable and breaks up into two drops, one drop remains on the substrate while the other is at the tip of the nozzle.

In a similar effort to produce microdrug reservoirs containing micrograms of active drug molecules, [56] configured their EHD printing apparatus in a slightly different manner by placing an inverted microscope (IX51, Olympus, Japan) under a transparent glass printing substrate thus ensuring a target specific deposition. This adaptation not only provided live video footage of the printing process but also could be used alongside a micromanipulator to adjust and correct for droplet placement errors during drug deposition at micrometre accuracies. A syringe pump (Fusion 400, CHEMYX, Republic of Korea) was used to pump the solution containing the drugs into transparent 30G conductive needles with internal orifices measuring at 140 $\mu$ m. The controlled deposition of the drugs into the microreserviors was done at a standoff height of 0.5–4.0 mm. Power supply used to produce the strong electric fields ( 2.5-8kv) was the B135, Korea Switching, Republic of Korea. The modified printer was shown to be capable of both continuous and drop on demand deposition of drugs in to microreserviors.

Khalid Rahman et al [57] used a commercially available electrohydrodynamic printing machine (NPexpert, Enjet Inc) for their studies. The z-axis nozzle holder and the x-y axis printing stage had a minimum resolution of  $1\mu\text{m}$  with a maximum acceleration of  $5\text{mm/s}^2$  and a velocity of  $600\text{mm/s}$ . They also installed a heating element under the printing stage. To generate the DC pulses for the drop on demand printing, a function generator was used in conjunction with a high-voltage amplifier (TREK, 609E-6). The ink was supplied to the tip of the nozzle via a syringe pump (Harvard, NEW PHD ULTRTM Nanomite). The nozzle used for printing was made by pulling a glass tube measuring  $750\mu\text{m}$  down to an internal diameter of  $60\mu\text{m}$  using a micropipette puller (P-97, Shutter Instrument). To provide the positive voltage for printing a thin copper wire was inserted into the glass capillary.

Researchers in [58] produced plasmonic nano-antennas with features sizes down to  $50\text{ nm}$  by employing the use of a printer with a 3D piezo-electric stage capable of nano-meter precision of  $10\text{nm}$ . The hardware was acquired from MadCityLabs and coupled with electrical equipment necessary for pulse generation in drop on demand printing. The nanostructures produced were viewed through an optical microscope operating in the iSCAT mode32 which permitted very precise detection of the printed nanostructures while also enabling steady focussing which was found to be useful when controlling the nozzle standoff height from the substrate. Multiple nozzles with internal diameters that ranged from  $550\text{ nm}$  and  $1,300\text{ nm}$  were made using the Sutter P-97 pipette puller. The nozzles underwent further modifications to make them fit for electrohydrodynamic purposes by coating the outer regions of the glass capillaries with a  $10\text{nm}$  adhesive layer of titanium followed by a  $100\text{nm}$  gold coating. Work in [59] and [60] was attempted using glass capillary nozzles made by pulling glass tubes into

tubes with diameters of 500nm, 1, 2, 5 and 10 mm which were sputter coated with gold/palladium in a (Denton, Desk II TSC) to make them conductive before being coated with a hydrophobic solution (0.1% perfluorodecanethiol in N,N-dimethylformamide). Printing ink is pumped through the nozzles and they are printed with for about 10 minutes. The nozzles are removed and immersed in a N,N-dimethylformamide solution for about 10 seconds before being air dried.

Work described in these studies [61, 62] was attempted by purchasing an EHD printer (NP-200, ENJET) from the company Enjet for their research work. Yonghee Jang et al used it to prepare a grid of electrodes made out of silver. The Silver ink used for the studies was also purchased from the same company. In this study [63] the researchers designed a printer that combined both the electrohydrodynamic effects as well as piezoelectric agitation to generate fine droplets at high frequency. Specialized piezoelectric nozzles (50 $\mu$ m internal diameter) were manufactured by micro-electromechanical system (MEMS) technique to facilitate this study. These nozzles consisted of silicon placed on wafers with pyrex glass. Their findings showed that they could control the droplet velocity without changing the volume of the droplets. In this system the meniscus is deformed by mechanical perturbations and not by the applied electric field.

Upon application of a driving waveform pulse via the driving-waveform generator (Softmecha) the piezoelectric actuator distorts to push the liquid out of the nozzle where the meniscus is then deformed into a cone form. The liquid is expelled through a jet that is formed because of the applied electric field after which the Taylor cone collapses back into

the nozzle to form the original meniscus. The modified jetting mechanism was observed by a high-speed camera (Motion Pro HS-4, Redlake Inc.) with a stroboscope that was in tune with the triggered with drive signal. They attributed this tight control of meniscus height to high frequency jetting that was made possible as result of this configuration.

Sukhan Lee et al.[64] described the use of a ring shaped gated electrode to focus electric field lines around the nozzle to bring about a reduction in satellite spray that is caused by electrohydrodynamic jetting. They identified the optimum ratio of outer nozzle diameter to the nozzle- ring gate electrode distance to be 2.5-5 times that of the outer nozzle diameter for maximum reduction in satellite spray.

Most circuit boards and functional films are fabricated using diverse materials and therefore the need for the rapid deposition of more than one material on a substrate has led to work described in [49]. They went further with the design reported by [48] and automated the multiunit print head by attaching a DC motor to the rotor axis. The printer featured a novel system that permitted micro and macro accurate placement of individual print unit nozzles through feedback loops during a multi-material print.

Researchers in [65] investigated the effect of ground electrode diameter on the resolution of printed patterns using a nanoparticle suspension of aluminium oxide. A pin to pin configuration was setup for the printing where a 920 $\mu$ m stainless steel nozzle was placed in-line with a sharp pin ground electrode. Three ground electrodes with diameters of 1, 100 and 1000 $\mu$ m were used in the investigation. They observed a decrease in printed line width

resolution from 25 $\mu\text{m}$  to 60 $\mu\text{m}$  as the ground electrode diameters increased from 1 $\mu\text{m}$  to 1000 $\mu\text{m}$ . They attributed the difference to the reduction in radial electric potential between the centre line and in any radial direction when using ground electrodes with small diameters (1 $\mu\text{m}$ ). In contrast, the use ground electrodes with large diameters brought about a randomized distribution of droplets and therefore wider lines. Researchers in [66] found a way to restrict backflow of the printing ink brought about by the effects of surface tension. They introduced a steel pole (diameter 0.2mm) into the printing nozzle which they claimed improved taylor cone creation by reducing the hysteresis time. Studies in [67] reported on precision droplet positioning through droplet collection on a conductive hydrophobic surface. Investigations in [68] used a similar pin to pin set-up to electrospin polycaprolactone nanofibrous rectangular mats (425-525nm) along defined geometries. A hollow cylindrical side electrode was used in conjunction with a sharp tip ground electrode to focus the electric field and direct the electrospun fibres onto a (x-y) movable dielectric stage.

In an effort to increase control over the printing process [69] wrote up their own customized version of a graphical user interface application using the C#.NET platform to control their printer. A H128 Motorized Stage was purchased from Prior scientific to be used as the substrate for controlled movements in the x and y directions. The motorized stage could make accurate movements to within 1 $\mu\text{m}$ . The specialized graphical user interface was used to control the stage and also allow the user to make changes to the acceleration and speed during the print. In addition to this the graphical interface application also controls a Firgelli L12 100 mm 210:1 servo linear actuator that is connected to a needle which is used to puncture a hole in the hemispherical meniscus to initiate the printing process. The authors claimed that it

offered a highly intense and localized electric field at low applied voltages that could be used to start fibre generation from the puncture site on the meniscus. The printing was conducted within an enclosed box so that they could control the humidity. A Phidgets 1125 humidity/temperature sensor was used as part of a feedback loop to maintain the humidity inside the enclosure at a pre-determined value within a  $\pm 3\%$  range.

Investigators in [70] developed an addressable triple nozzle device from silicon that is capable of being independently controlled to dispense multiple inks in the cone-jet mode without interference or distortion from adjacent nozzles. The system described was modulated by the supply of solution to the individual nozzles through dedicated syringe pumps and since this is impractical on a large scale. Work described in [71] recommended a multi nozzle addressable system based on a multi-level voltage method (MVM) where all the nozzles are supplied with printing ink through a reservoir and applied air pressure. The array of nozzles is connected to a pulse voltage while a series of rings placed under each nozzle is supplied with DC voltage to initiate and control jetting. They showed that through control of the applied potential to each ring they could reduce interference and distortion during jetting and achieve consistency in the dimensions of dispensed droplets. Research in [72] reported similar work with ring shaped extractors when they attempted to print continuous conductive lines. Studies in [73] investigated the effect of nozzle tip design in an attempt to improve the printed line width of silk fibroin. They successfully proved that wide nozzles (800 $\mu\text{m}$ ) could be used to deposit lines as narrow as one 1 $\mu\text{m}$ .

The controlled deposition of various materials with nano-scale dimensions using nozzles with small orifices has been reported by quite a few research groups with varying degrees of success. Work in [74] generated line widths reaching close to 700nm using a nozzle with a 1  $\mu\text{m}$  internal diameter. They predicted that improved nano-scale resolutions would be achievable if nozzle dimensions were further reduced. They also speculated that the electric field concentration brought about by the sharp tips of the nozzles could help reduce lateral distribution of the jet deployment provided that stand-off heights and applied voltages were kept low. Furthermore, [75] were successful in depositing nano dots with diameters close to 200 nm. They also went onto deposit these dots in close succession to produce lines with nanometer widths. This was done using nozzles with sub-micrometer dimensions.

Apart from reducing nozzle dimensions or using specialized equipment there is very little work reported on investigating nozzle design. They [76] performed a systematic study into the effect of needle tip geometry on the electrohydrodynamic spraying process and reported that the size distribution and liquid relic size significantly reduced with a reduction in needle tip angle. While researchers in [77] controlled the jetting frequency by designing a novel retractable needle that was able to deposit both dots and “beads on a string” structures. They varied the flow rate, concentration of polymer and the frequency of needle oscillation during the printing and established that the jetting frequency shared a close relationship with the retractable frequency of the needle.

The studies in [78] showed the effect of modifying the applied electric field through the use of conical electrohydrodynamic lens. They determined that a slim conductive electrohydrodynamic lens with a hollow conical configuration produced intensified closely

packed electric field lines. The conical configuration was reported to produce a printed line width of 80-100 $\mu$ m when printing with silver nanoparticles and was postulated to be able to limit jet break up due to field focusing effects. Researchers in [79] also studied the effect of electrode configuration on electrohydrodynamic droplet dispensing between two parallel plates (electrodes) for use in DNA microarrays. Three test electrodes were fashioned in a circular, planar and needle shape to test the volume that could be dispensed along with spot size of the droplet dispensed. Additionally, the surfaces of the electrodes were modified with silicon-oil and Teflon film to further understand droplet behaviour after ejection. DNA solutions were prepared with concentrations ranging from (1-10,000nM) containing the oligonucleotide FITC-RQC3 (Operon Biotechnologies, AL, USA) recognized from the Hepatitis C virus (HCV). They were able to conclude that the needle shaped electrode produced droplets with the highest resolution (200 $\mu$ m). The Circular (950  $\mu$ m) and Planar (970 $\mu$ m) shaped electrodes produced similar droplet resolutions. They found that the surface coating played a key role in improving droplet resolution. The most hydrophobic layer (Teflon) seemed to induce high contact angles for the deposited droplets and as result led to an improvement in resolution. Droplet resolution was affected by humidity levels through solvent evaporation rates while changing the concentration seemed to have a negligible effect on resolution.

In order to validate their system [48] performed a validation study where they reported printing an image with average droplet sizes of 2.8 $\mu$ m using a micropipette with an orifice diameter of 5  $\mu$ m under an applied DC voltage. Their results show that they are able to use the EHD phenomena to surpass conventional inkjet drop on demand resolutions of 20  $\mu$ m to

print at high resolution. They also reported difficulties in controlling droplet placement but did not offer a solution to the problem. Investigators in [52] offered an innovative solution to the problem by introducing a modulated AC-pulse voltage instead of a steady DC voltage and claimed that the same high resolution droplets could be produced with far more placement accuracy. They attributed the lack of accuracy to the residual charge that is deposited on an insulating substrate which consequently generates its own electrostatic field which in turn causes subsequent droplets to deviate off course. The use of a modulated AC-pulse voltage results in both positively and negatively droplets being produced alternatively thus effectively cancelling out the residual charge after one AC sinusoidal wave is completed. This makes this technique more robust when compared to the single polarity DC voltage ehd printing since regardless of the type of substrate material used the resultant printed charge is zero.

They noted a decrease in droplet diameter from 30 to 10 $\mu\text{m}$  as the pulse frequency increased from 25-350Hz. Work described in [80] studied the effect of AC voltage on direct writing nano and microstructures (10-40  $\mu\text{m}$ ) on to polyethylene terephthalate substrates. They claimed that the use of AC voltage (0-1000 Hz) modified the charge transfer characteristics on the continuous jet and as a result brought about a reduction in coloumbic repulsion which was linked to jet stability. The printed lines became wider as the applied frequency was increased from 0-750 Hz after which further increases in frequency brought about a decrease in line width. Similarly, [81] also studied the effect of AC pulse voltage and the process parameters on morphology, frequency of droplet deposition and droplet diameter. Their droplet resolutions were much lower compared to previous work (100-300 $\mu\text{m}$ ) at a deposition frequency of (25-5 Hz). They claimed that the positive voltage segment of the applied AC pulse caused the meniscus to stretch out in to fine jet until the negative segment of the pulse

set in and retracted the jet. This retraction caused the jet into microdroplets. Deposition frequency was also reported to increase with an increase in AC voltage frequency which subsequently led to finer droplets.

## **2.8 Electrohydrodynamic high resolution printing through the pyroelectric effect**

They [82] employed the use of a pyroelectric effect whereby a lithium niobate crystal substrate is placed near a target substrate and is heated using a focused infrared laser to produce high voltages in the kV range. These voltages elicit an electrohydrodynamic response from a reservoir of solution placed near the target substrate thus drawing out attolitre droplets in the form of a fine jet. They were able to deposit many advanced materials with printed line widths reaching 100nm. The technique overcomes many of the issues relating nozzle dimensions to the ability to print at nano-scale. Creation of a virtual nozzle not only makes nano-scale patterning a realistic possibility but also eliminates the need for specialized capillaries or nozzles that are more often than not fragile and prone to clogging up [82-84].

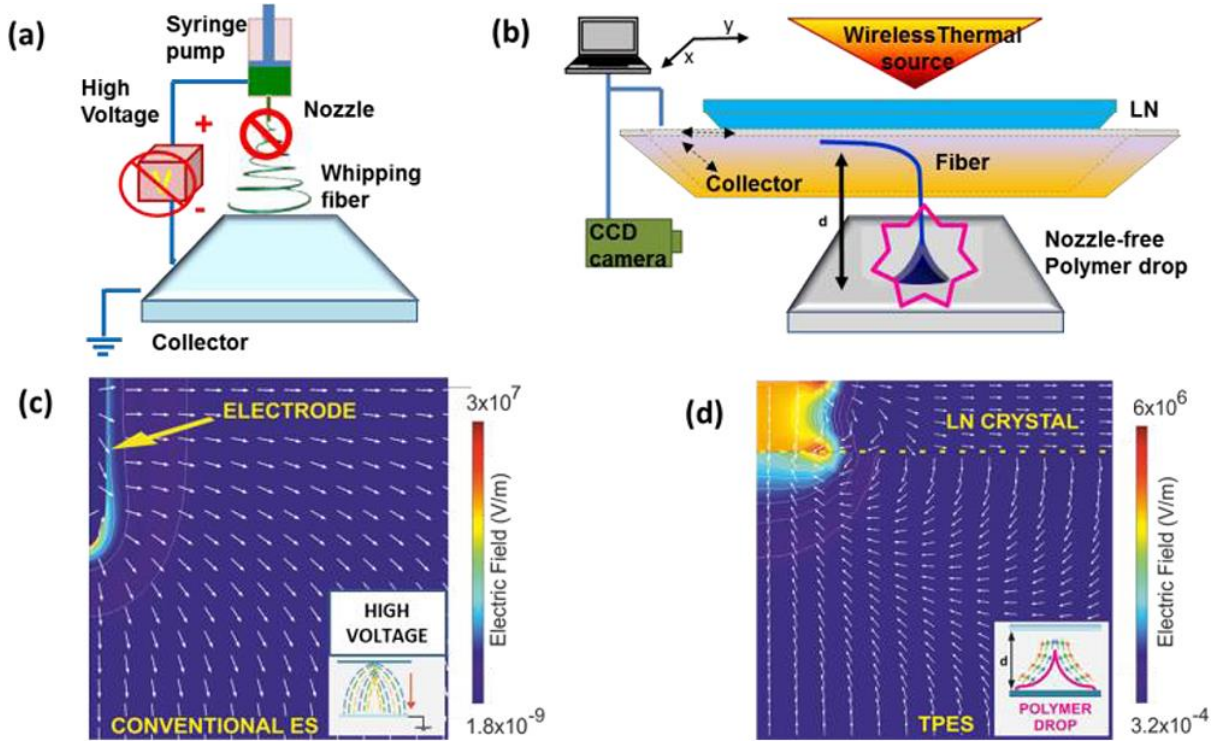


Figure 5 (a) Set-up of conventional ES apparatus with nozzle and high voltage power supply. (b) Wireless ES system made of three principle components: thermal source, LN crystal, and polymer drop. (d) Finite element simulation of sharp-cone electric field lines ((arrows) compared with (c) conventional ES field [90].

Also [85,86] used the same pyroelectric phenomena in a modified form of the technique where a 500 $\mu$ m thick ferroelectric lithium niobate crystal and the heated end of a soldering iron was used to generate electric field strengths that ranged between  $2.7 \times 10^7$  V m $^{-1}$  and  $5.5 \times 10^7$  V m $^{-1}$ . They successfully produced micro lenses from droplet reservoirs of PMMA (polymethylmethacrylate). Similar work attempted by [87] showed that they could produce an array of 10 microlenses with a focal length of 1.5–3mm using PMMA as the material. Further work by [88] using PMMA revealed that the technology was strongly dependent on the viscosity of the polymer used in the Pyro-Ehd technique and that as the polymer viscosity increased the diameter of the microlens printed also increased. They were able to produce microlens with a diameter of 20 $\mu$ m with a focal length of 1.6mm. They determined that the overall geometry and focal properties of the microstructure could be altered by varying the

ratios of the solvent mixtures and the surface energy of the substrate thereby influencing the wetting angle of the dispensed drops of PMMA. Additionally [89, 90] brought to light how the electrodeless technique could be used for high throughput commercial purposes through the generation of self-assembled multiple jets. This included the printing of interspersed multiphase materials through liquid multi-jets.

## 2.9 Electrohydrodynamic printing LCD screens

Electrohydrodynamic drop on demand printing technology is capable of print depositing at high resolution. This includes materials with a surface tension and viscosity much higher than those of the inks used in inkjet printing 1-20mPa.s and 30mn/m<sup>2</sup> as compared to 1000mPa s. The versatility of the EHD allows for the droplet size to be easily managed depending on the needs by just changing the applied voltage and thus changing the mode of operation. For example [91] investigated the possibility of using EHD multi-jet mode to lay down a layer of polyimide on indium tin oxide coated glass for its use as a liquid crystal alignment layer in LCD's. A high viscosity solution of 56cps was used to create an even 50nm thick layer of polyimide at an applied voltage of 7 kV and a hydraulic pressure of 0.27 KPa. In order to equally align the liquid crystal statements, the PI layers were rubbed along a single direction at a rubbing strength of 300mm. subsequent AFM results also showed that rubbing brought about a decrease in surface roughness as indicated by the RMS values which were 2.063 nm for the EHD printed polyimide layer and 2.327 nm for the spin coated polyimide layer. These results represent a decrease in surface roughness which is the same for both of the cases considered thus proving that EHD printing neither improves nor degrades liquid crystal

alignment. Further tests on the optical transparency of the liquid crystal cells also revealed that both spin coated and EHD printed polyimide layers had the same optical transparency. Transmittance was also measured by pre-tilting the liquid crystal cells in the vertical plane by  $\pm 70^\circ$  to show that liquid crystal alignment was not affected by the rubbing. There were minor differences between spin coated and EHD printed liquid crystal cells. The authors concluded that EHD printing could serve as a suitable viable alternative to spin coating when it came to making twisted nematic liquid crystal cells for LCD screens.

## **2.10 Biological applications of high resolution electrohydrodynamic printing**

Investigations in [60] described the use of the electrohydrodynamic printing technique to print single distinct protein molecules such as ( $\gamma$ -globulin, streptavidin and IgG, fibrinogen) as well as a combination of different protein molecules in patterns on the same substrate rapidly over a large scale using multiple and single nozzles depending on the particular application with exceptional control over spatial dimensions. They showed that they could pattern conventional substrates like plane silica in addition to the more unconventional structured plasmonic crystals for the study of nano and micro arrays. A streptavidin protein array was constructed by patterning the protein on to an epoxy-silane-modified  $\text{SiO}_2/\text{Si}$  substrate was shown to still poses biological functionality after being EHD printed with the ability to identify and combine with biotin-modified DNA. Research in [92] demonstrated the versatility of the technique but electrohydrodynamically printing, spinning and spraying both PU and PMSQ (poly(methylsilsesquioxane)) polymer. In doing so they illustrated how a wide range of 3D structures could be fabricated. Complex protein macromolecules such as silk fibroin are known for their mechanical properties and biocompatibility. The material offers

many opportunities in the fields of controlled drug delivery and scaffolds and a recent study conducted by [93] highlighted the potential for depositing silk fibroin using electrohydrodynamic printing. They successfully printed a variety of intricate patterns at resolutions that varied between 3 and 40  $\mu\text{m}$  depending on the chosen set of parameters. The solution viscosity was identified to be the most important parameter when it came to printing with a flatbed print head

Studies in [94] used the electrohydrodynamic cone-jet mode to deposit bacterial cells (*Escherichia coli* cells) in the form of droplets along well-defined 160 $\mu\text{m}$  wide lines on nutrient membranes. The growth of the bacterial cell colonies post printing resulted in printed lines with a measured height of 50 $\mu\text{m}$ . The cells were printed in a solution composed of ethylene glycol, phosphate buffer and sodium chloride. Increasing the concentration of ethylene glycol from 20% to 40% by volume led to a finer line width while further increases to 80% and 100% of ethylene glycol resulted in a random scattering and ordering of droplets for 80% ethylene glycol. No patterns were observed at an ethylene glycol concentration of 100% and this was attributed to the bacterial colonies consolidating within the printing ink. Further work by [95] involved optimizing the electrohydrodynamic print technique to print collagen onto agarose coated glass plates. By varying the applied voltage (3.5-9.5kV) and stand-off height (1.2 -1.4 mm) they were able to pattern the glass plates with the dripping, multidrip, cone jet and contact mode. Straight lines were produced with a line widths measuring  $170 \pm 10\mu\text{m}$  in the cone jet mode. The dripping mode resulted in collagen droplets varying between 50-500 $\mu\text{m}$  while the contact mode led to straight 500 $\mu\text{m}$  wide lines of

collagen. HeLa and HEK293 cells were shown to grow and proliferate well on collagen patterned substrates.

Similar work reported by [54] further validated the findings as they used a similar electrohydrodynamic DNA printer to print many kinds of DNA in the form of droplets within the submicrometer range. They showed that fluorescence binding assays were not affected by this particular printing technique. Intricate geometries possessing submicrometer sized characteristics printed at sizeable scales were also shown to be possible. These patterns could be used to create adenosine biosensors and selective templated assisted nanoparticle assembly. The technique can be used to print patterns of DNA aptamers in immobilized form for the selective sensing of various analytes such as proteins, molecules and cells. DNA microarrays printed with commercially available piezoelectric inkjet printers fall short when it comes to the spacing between the printed dots which stand at a maximum resolution of 10 $\mu$ m. Drop on demand electrohydrodynamic printing overcomes this barrier with dot spacing's of 100nm thus highlighting its potential use in DNA microarray technology.

Work described in [96] showed for the first time that they could use the electrohydrodynamic printing technique in both pulsed and continuous jet mode to accurately lay down extracellular creating matrix proteins (Fibronectin and rabbit Immunoglobulin-G) at resolutions of less than 5 $\mu$ m onto pliable substrates (polyacrylamide hydrogels) for cell culturing purposes. The resolutions at which the functional inks were printed at represent a scale that is smaller than the average cell sizes and thus paves the way for improved mechanobiology studies. Investigators in [97] successfully showed that they could use the

electrohydrodynamic printing technique to print colloidal suspensions of  $2\mu\text{m}$  sized polystyrene particles in form of bands of parallel lines to give rise to colloidal crystal arrays on to rotating silica glass substrates.

Likewise, [59] were able to demonstrate how high resolution electrohydrodynamic printing technology could be used in the semiconductor industry by printing block co polymers to generate Block-Co-polymer thin films. They were able to manipulate and control the periodicity, size and morphology of the patterns of BCP printed. Droplets of BCP inks as small as  $100\text{nm}$  were deposited in varied geometries with varied molecular weights and compositions. The molecular weight determines the periodicity of the Block-Co-polymer film while BCP patterned structures could be arranged such that the spacing's range from  $20\text{nm}$  to several centimetres. Further work by [98] involved print depositing narrow line widths of copolymers composed of varying quantities of P(S-ran-MMA) and methyl methacrylate with end functional groups along user defined geometries to produce polymer brushes that can be used to direct nanoscale domain geometry.

Researchers in [99] and [100] showed that the continuous jet EHD printing technique could be used to fabricate 3D scaffolding out of a biocompatible polymer (Polycaprolactone) for cartilage regeneration. Layered mat scaffolds (20-200 layers) were produced with a pore size of  $500\mu\text{m}$  and a strut diameter of  $20 \pm 1.9 \mu\text{m}$ . Their studies showed that after modifying the surface of the scaffold for hydrophilicity there was good attachment of chondrocytes. The chondrocytes were able to sustain their phenotypes and were responsible for the presence of high levels of type II collagen and sulphated glycosaminoglycan. The composition of the

scaffolds were analysed using Fourier infrared transform transmission which revealed that the solvent (acetic acid 99% purity) that used to process the PCL into solution was not present in the scaffolds after they were printed.

Alternatively, [101] offered a contrasting approach to electrohydrodynamically printing polycaprolactone whereby they printed in the continuous jet mode into a polyethylene oxide solution bath using low polymer concentrations (15wt %) dissolved in a slow evaporating solvent (dimethylformaldehyde) with a high boiling point of 153°C. When compared to [99] and [100], high concentrations of (70% w/v) polycaprolactone were dissolved in a comparatively fast evaporating solvent (acetic acid 99%) boiling point of 118°C. The low concentrations used by [101] meant that the applied voltage used was at 10kV which is approximately three times higher than that used by [99] and [100] which is 3kV.

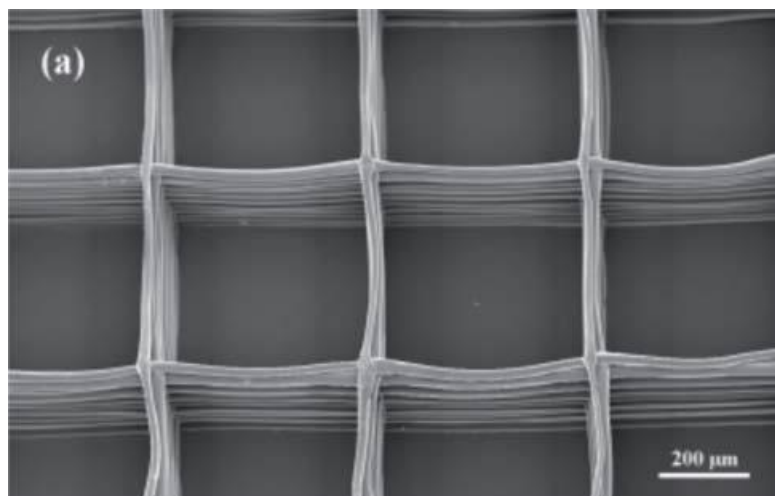


Figure 6: Surface topography of PCL [99]

The PCL solutions in both sets of work were pumped through nozzles with the same inner diameter of 510 $\mu$ m with low flow rates and back pressures reported at 1 mL h<sup>-1</sup> for [101] and 1.5 bar for [99] and [100]. The polyethylene oxide bath served a dual purpose of allowing the individual printed struts enough time to adhere to each other while also permitting stable movement of each deposited layer such that three dimensional structures could be formed through layer by layer sedimentation. The uniqueness of the scaffold lay in the rough surface topography of the scaffolds struts which encouraged cell adhesion and proliferation. Nevertheless they struggled to maintain control over both the micro and nano-sized struts which had a reported width of 253  $\pm$  27  $\mu$ m and a scaffold pore size of 347  $\pm$  86  $\mu$ m. When the scaffolds were seeded with osteoblast-like cells (MG63) they were shown to have significantly higher water absorption capabilities (400% increases) with much improved cell viability(x20) and enhanced alkaline phosphatase activity, mineralization (x6).

Studies in [102] alternatively showed how a combination of process (flow rate) and solution parameters (PCL weight fraction) including additional parameters like the surface tension of the collection media could be used to induce microfiber entanglement and produce scaffolds consisting of microfiber struts embedded within a weave of tangled microfibers using a single printing nozzle. A series of collection media solutions were prepared by varying the compositional ratio of ethanol to water in order to vary the surface tension from 22.1 to 39.8 mN/m. They observed a transition in deposited PCL from microsized struts (123 $\mu$ m) to microfibers (3.3 $\mu$ m) as the surface tension of the collection media was reduced from 39.8 to 22.1 mN/m. They hypothesized that this occurred due to rapid mass exchange taking place while the surface tension of the printing ink (dimethylformamide + methylene chloride +

PCL) repressed surface charges and overcame the surface tension of the collection media which led to microfibers being produced when printing in the continuous jet mode (10-14 kV) . Limiting the rate of mass transfer by either changing the amount of collection media or by altering the PCL flow rate / PCL weight fraction led to the outline of processing diagrams for the synthesis of both stable and unstable fibrous constructs. Cell studies showed good cell attachment and proliferation of preosteoblasts.

Building up on earlier published work [103] attempted to introduce control in the fabrication of PCL scaffolds in terms of porosity, mechanical property and shapability. This was made possible through the co-axial printing of low and high concentrations of polycaprolactone into an ethanol bath such that scaffold struts with a solid inner core, enveloped by a fibrous outer layer of polycaprolactone were printed. They were successful in altering strut microstructure through simple manipulation of flow rate and concentration. The scaffolds were coated with collagen-I to perform in-vitro cell studies with preosteoblast MC3T3-E1 cells. The studies revealed enhanced cellular activities with the fibrous hybrid scaffold when compared to their previous work.

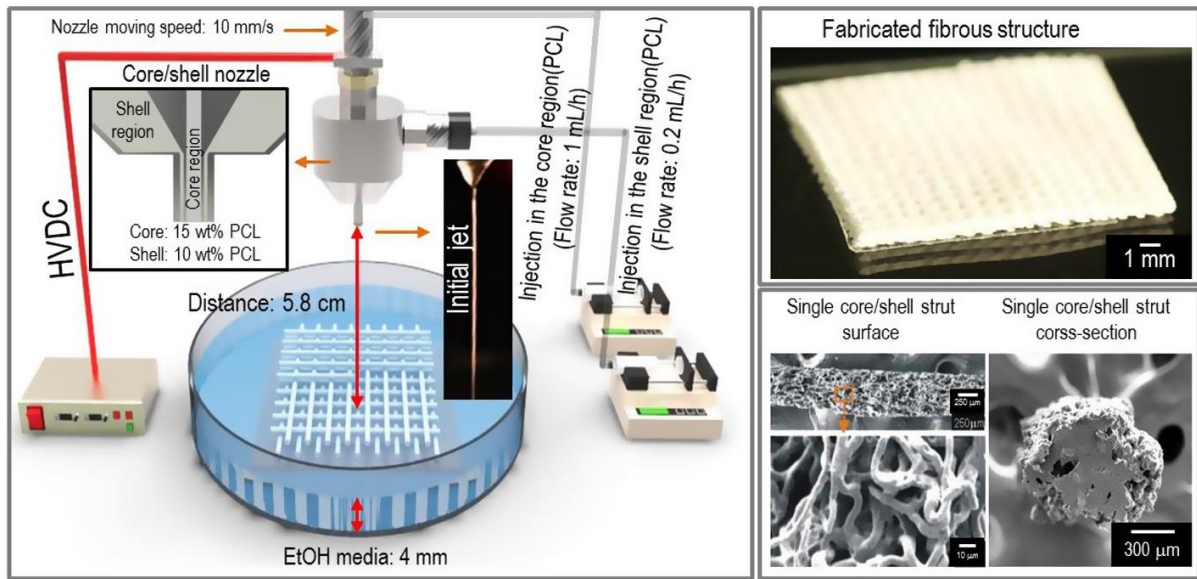


*Figure 7: Schematic of an electrohydrodynamic system supplemented with a dispensing system, ethanol medium in the target bath, and a core/shell nozzle. An optical image of a single jet from the nozzle and SEM images of the deposited fibrous strut.*

In further work by [104], used the hybrid technique of electrohydrodynamic melt plotting to print scaffolds that were composed of alternating layers of perpendicular struts and roughened micro-sized EHD deposited threads. They were able to demonstrate that the scaffolds had excellent water absorption and biological activity in terms of cell site activation, proliferation and differentiation with (MG63) osteoblast cells. Also, additionally they found out that it was possible to control the mechanical properties of the scaffolds by changing the design of the scaffold. They concluded that the mechanical properties were mainly determined by the layers that were melt printed rather than the EHD printed micro-threads.

Here researchers [105] combined the melt extrusion technique with electrospinning to produce hybrid scaffolds in a two-step fabrication route that resulted in scaffolds with two levels of alternating architecture. The extruded polycaprolactone scaffold with a fibre

diameter of (713 $\mu$ m) was enmeshed within an electrospun woven mesh of microfibrous PCL with a fibre diameter of (2.7 $\mu$ m). The fibrous component of the scaffold was reported to improve the cell attachment and offer higher surface area to induce interactions with proteins while also offering enhanced cellular activities (calcium deposition, cell proliferation and ALP activity). The hybrid scaffolds were also proven to possess similar mechanical properties to pure extruded scaffolds.

Work conducted in [106] described the electrohydrodynamic printing of PCL-80,000 with nHA powder mixed into it (15 wt. % of the polymer) along pre-defined paths to generate three dimensional constructs with an average width of 50 $\mu$ m and a 200 $\mu$ m gap width between the struts. Density mapping analysis of the constructs showed that regions containing calcium were more prevalent in structures that were printed with hydroxyapatite (PCL-nHA) when compared to those without hydroxyapatite powder. The finding was further corroborated by elemental analysis which revealed peaks for calcium and phosphorous on the PCL-nHA constructs while being absent on the constructs with only polycaprolactone. In addition to controlling architecture shape, porosity, shape width, polymer; the active components in such structures can also be modified to deliver a desired response. In order to demonstrate the potential bioactivity of the composite structures containing nHA, a simulated Body Fluid (SBF) solution was prepared (two weeks of incubation under suitable conditions).

The printed structures comprising of pure PCL polymer (50 $\mu$ m wide), PCL-nHA (50 $\mu$ m wide) and PCL-nHA (5 $\mu$ m wide) showed clearly the formation of apatite in the composite structures. Cruder prints of 50 $\mu$ m were demonstrated clear apatite formation. The same effect

was observed with the higher resolution prints ( $\sim 5\mu\text{m}$ ). When printing PCL without any bioactive agents, there was no apatite formation on the surface and there was some evidence of polymer degradation. This method of preparing ordered structures demonstrated the ability to incorporate order, chemical aspects, and surface morphology into topographic and engineering structures.

Further work by [107] involved the study of the behaviour of fibroblast L929 cells in response to ordered printed topographies of PCL microfibers measuring (3-5  $\mu\text{m}$ ). The cell biomaterial interaction was studied using time lapse microscopy that revealed a dynamic interaction between the cultured cells and the printed PCL microfibers that involved the adherence and disunion of cells to and from the microfibers. The tendency for cells to adhere to the microfibers reduced with distance from the microfibers. The cells were also observed to traverse along the microfiber once it latches on while other cells were seen to drift to regions underneath the PCL microfibers that came loose.

Researchers in [108] electrohydrodynamically printed two polymers (nonbiodegradable polyhedral oligomeric silsesquioxane-poly (carbonate-urea) urethane) and (biodegradable polyhedral oligomeric silsesquioxane-polycaprolactone-poly (carbonate-urea) urethane) along controlled predefined architectures. The macroporous structures produced had polymer fibres with diameters that ranged from 15-50 $\mu\text{m}$  with scaffold porosity of 250 $\mu\text{m}$ . They reported that the fibre diameter was highly dependent on the needle-substrate standoff height, polymer viscosity and applied voltage. Printing on ethanol led to the rapid precipitation of polymer and made it possible for them to remove the scaffold for further analysis which was

not possible when printing on glass substrates. They struggled to increase the thickness of the scaffolds beyond 0.5–1 mm and this was attributed to the flow rate from the needle tip where the polymer would solidify through solvent evaporation after five printed layers. They suggested that better infusion equipment would improve results.

## **2.11 High resolution printing of conductive tracks using continuous jets**

The same continuous E-jet printing technique was used by [109], [110], [111], [112], [113], [114] to print conductive lines for use in the circuit boards and flexible electronics in electronic manufacturing industry. Work in [115] showed how electrohydrodynamic printing can be used in the repair of flat panel displays. They were able to electrohydrodynamically print using a continuous jet, fine 3 $\mu$ m wide and 230nm thick silver lines on hydrophilic non-conductive pyrex glass slides. The printing technique was merged with in-situ laser sintering using a 100mW, 532nm spot laser. Subsequent electrical resistivity measurements revealed that the sintered silver lines had a resistance of 163 $\Omega$  with a resistivity of 17.48  $\mu\Omega$  cm which was pointed out to be lower than 20  $\mu\Omega$  cm that is usually needed for flat panel displays. Similarly, [114] work in electrohydrodynamic printing of nanoparticle silver lines on polyimide substrates generated coarse line widths of 200 $\mu$ m with line thicknesses of 300nm. The wider conductive lines meant that the measured impedance values were much lower (18 $\Omega$ ) when compared to [115]. The calculated resistivity values were reported at 4.8 $\mu\Omega$ .cm which is three times higher than the bulk resistivity of silver but lower than the resistivity values reported by [115].

This study [110] was carried out using a much larger nozzle (50 $\mu\text{m}$ ) when compared to the drop on demand studies by [109] and [112] to dispense 30% wt silver ink in the continuous jet mode on to silicon substrates to produce lines with a reported minimum width of 6 $\mu\text{m}$ . The novelty of the study was in the way the nozzle was oriented with respect to the moving substrate. They tilted a hypodermic nozzle and pumped the 30wt% silver ink at a flow rate of 0.1 $\mu\text{l}/\text{hr}$  from a stand-off height of 3mm and at an applied voltage of 3000V. They suggested that tilting the nozzle enhanced the electric field strength in the axial plane without any increase in the radial plane which reduced the diameter of the cone-jet resulting in a stable fine jetting. Their research also revealed that using this tilted configuration allowed for similar resolutions when compared to resolutions achievable by EHD drop on demand. Yet these printing resolutions were obtainable by using higher flow rates, voltages and stand-off heights. Khalid Rahman et al [113] showed that it was possible to print conductive copper lines by using a colloidal solution containing copper nanoparticles to pattern a silicon substrate. Conductive copper lines 84nm thick and 12 $\mu\text{m}$  wide were produced with resistivity's that fluctuated from  $5.98 \times 10^{-8} \Omega\text{m}^{-1}$  to  $2.42 \times 10^{-7} \Omega\text{m}^{-1}$  depending on the width of the printed copper lines.

Researchers in [113] and [112] used the cone jet mode to deposit continuous copper conductive tracks form solutions containing copper nanoparticles. [113] used 100 $\mu\text{m}$  sharp tipped nozzles and reported a lower printed line widths of 32 $\mu\text{m}$  with higher resistivity of 6.8 $\mu\Omega\text{.cm}$  while [112] went a step further and used a much finer nozzle (60 $\mu\text{m}$ ) and printed their copper tracks at a much narrower line widths of 12 $\mu\text{m}$  and much lower resistivity of

$2.42 \times 10^{-7} \Omega \text{m}$ . [109] printed  $70\mu\text{m}$  continuous silver lines with a line thickness of  $150\text{nm}$  by reducing the standoff height to  $50\mu\text{m}$  between the printing nozzle and the silicon substrate. This was done to suppress the jet disintegration that is normally experienced when using high voltages to generate a jet with a highly conductive printing ink like silver. Furthermore due to the high conductivity of the silver, the printing ink was not pumped into the  $20\mu\text{m}$  aluminium nozzle. Researchers in [116] were able to use the electrohydrodynamic continuous cone-jet mode to align  $40\text{ nm}$  wide silver nanowires and print deposit them. The nanowires were dispersed within in a solution mixture made up of polyethylene oxide /ethanol/ deionized water. Investigators in [117] manufactured flexible conductive heaters by electrohydrodynamically printing a network of conductive silver nanoparticle lines ( $<10\mu\text{m}$  in width) through a  $100\mu\text{m}$  nozzle on to a graphene/PET substrate. The substrate was composed of a monolayer of graphene that was hot pressed onto a transparent PET film. The silver/graphene hybrid electrode contributed to high electron mobility and as a result enhanced the heating effect when a voltage was applied. While studies in [118] led to the generation of conductive fibres and films through near field electrospraying with silver nanoparticles and silver nanowires.

## **2.12 High resolution printing of conductive tracks, drug encapsulation using EHD drop on demand and EHDA ( Electrohydrodynamic atomization)**

When the procedure was repeated in the drop on demand mode by applying a pulsed voltage the printed line width reported was much lower at  $35\mu\text{m}$ . The printed tracks yielded a good low resistivity of  $(2-4) \times 10^{-8} \Omega \text{ m}$ . In further work done by [119][120][121] showed that in the drop on demand mode at close printing distances of  $125\mu\text{m}$  they were able to print

circular organo-metallic pads with diameters that ranged from 125 $\mu$ m to 185 $\mu$ m as the pulsed voltage was increased from 500 V to 800 V with an average thickness of 200nm. Reducing the stand-off height further to 95 $\mu$ m resulted in circular pads with diameters of 88  $\mu$ m. Continuous lines that were 150 $\mu$ m wide and 150nm thick were printed by carrying out the same dispensing but on a continuously moving substrate which reduced the distance between individual circular metallic pads until they merged to form a single continuous silver line. A silver rectangle was printed to determine the resistance of the lines which was 30.6  $\Omega$  with a resistivity of  $3.9 \times 10^{-8} \Omega \text{ m}$ . Three dimensional structures were also attempted by repeatedly printing over the same line and they concluded that the line width increased very slightly in the lateral plane but rather accumulated as five layered structures were produced. Studies in [122] led to an investigation into the effect of viscosity of silver nanoparticle suspension on electrohydrodynamically printed silver lines. They printed with a low (5 mPa s) and high (112 mPa s) viscosity suspension of silver nanoparticles and showed that by increasing the viscosity of the printing ink finer line widths (580 $\mu$ m) could be produced when compared to the line widths generated from low viscosity suspensions (1120 $\mu$ m). They also noted a 95% drop on sheet resistance ( $0.037 \Omega/\text{m}$ ) for lines printed with high viscosity. Wang et al [123] showed that in addition to silver ink, colloidal gold nanoparticles can be dissolved in solution and disbursed via voltage pulse modulated deposition. They reported print patterning rows of gold circular drops less than 10 $\mu$ m in diameter using 20 $\mu$ m sized nozzles at voltages that ranged from 800 V to 1000 V.

Jaeyong Choi et al [124] introduced an innovative print head design for drop on demand electrostatic inkjet printing of commercial nano silver ink. The print head consisted of a glass

capillary nozzle measuring 100 $\mu$ m in diameter with a ring shaped electrode placed at the end of it. Embedded within the glass capillary is a platinum wire that acts as the ground for the circuit. They found that at low voltages of 1.5kV and a jetting frequency of 40Hz, the droplets produced were large ( $520 \pm 16\mu$ m) which sharply decreased to ( $30\mu$ m) with an increase in voltage and jetting frequency to 2.1kV and 900Hz. Both glass and PET substrates were printed with silver dots and lines. The droplets coalesced to form lines measuring ( $205\pm5\mu$ m) in width.

Using the same drop on demand technology [125] were successful in electrohydrodynamically deposit silver nanoparticle ink on to a flexible polyethylene terephthalate (PET) substrate in an effort to fabricate micro temperature sensors on large scale using R2R system. At a jetting frequency of a 100Hz, an uninterrupted steady stream of droplets was generated to print a set of parallel full lines at a line width of 30 $\mu$ m. A measured resistivity for the device was reported at 25.35  $\mu\Omega\cdot\text{cm}$  with a temperature resistance coefficient of  $0.0007687\text{ }^{\circ}\text{C}^{-1}$ . In their study [126] on the elastic and viscous properties of poly(ethyleneglycol) diacrylate hydrogels employed the use of drop on demand to precisely deposit controlled droplet volumes(nano-gram scale) of hydrogel multifunctional monomer at accurate separation distances of 40-60 $\mu$ m on to micromechanical resonant sensors. Once the sample was cured they were able to gauge the micromechanical properties of the hydrogel.

Studies carried out in [127] were able to print pattern silver ink in EHD drop on demand mode on untreated glass slides. A glass capillary with a 10 $\mu$ m internal diameter was used to

deposit drops with diameters of  $3.6\mu\text{m}$  at a stand-off height of  $250\mu\text{m}$  which is a much than those used by Wang et al their studies. Nevertheless, the higher stand-off height used was offset by application of a gentle back pressure of  $0.5\text{kP}$  to the printing ink which was never used by [119][120][121] in any of their studies. The researchers reported that they did observe a similar in trend droplet diameter vs applied voltage. As the voltage was increased from  $950\text{V}$  to  $1600\text{V}$  the droplet diameters generated increased from a minimum of  $7\mu\text{m}$  to a maximum of  $13\mu\text{m}$ . The droplets were then printed in close succession such that they overlapped to produce continuous printed lines with a minimum width of  $6.5\mu\text{m}$ . These lines had measured resistivity's that ranged from  $62.5\mu\text{m}$  for the widest lines ( $31.3\mu\text{m}$ ) to  $111\mu\text{m}$  for the narrowest printed line ( $6.5\mu\text{m}$ ). The researchers in [128] were able to repeat the work done by [127] and [119][120][121] to deposit identical less than  $10\mu\text{m}$  sized silver dots in periodic rows.

Work done by [129] using silver ink resulted in much larger droplets sizes that ranged between  $45\text{-}55\mu\text{m}$  using a  $110\mu\text{m}$  wide nozzle. However, they went on to fabricate simple electronic components like resistors composed of poly(3,4-ethylenedioxothiophene):poly(styrenesulfonate)/poly(vinylpyrroli-done) films. The resistance was varied by changing the ratios of the two polymers resulting in resistance values from ( $10^1$  to  $10^6\Omega$ ). Conductive tracks measuring  $60\text{-}70\mu\text{m}$  wide were interlinked to form capacitors with a capacitance of  $6\text{pF}$ . Similarly, spiral inductors ( $0.6\mu\text{H}$ ) were also printed with a regular spacing of  $220$  and  $110\mu\text{m}$ . They also noted similar observations when it came to the effect of applied voltage on droplet size. Increasing the voltage from  $1.2$  to  $2.2\text{ kV}$  resulted in larger droplets coupled with

significant droplet scattering that they attributed to increased columbic repulsion to due to the high electrical conductivity of silver.

Another variant of the same technology is EHDA ( Electrohydrodynamic atomization) which was used by [130] to produce a fine dispersion of drops which is then guided to a targeted destination on the silicon substrate. Under a specific set of conditions of low flow rate (nanolitres/min) and the use of nozzles with internal diameters that are in the tens of microns – a mode called nano-electrospray can be achieved. When operating in this mode, nano-droplets can be generated and deposited. Thus this mode can be exploited to achieve resolutions within the realm of nanometers. Novel work reported in [58] used the same nanodripping mode to deposit (3-7nm) gold nanoparticles onto a substrate in the form of 50nm wide and 200nm tall gold nano-pillars. The gold ink was pumped through glass capillaries with internal diameters of the order of  $1\mu\text{m}$  at standoff heights of  $5\mu\text{m}$ . This dispensing height was chosen to eliminate the electric field in the lateral plane thus ensuring that the nano-drops that form are guided to their target site. The curved bulge created due to the growth of the nano-pillars also introduced an auto focussing effect that served to attract the incoming droplets. By such means [58] showed that a diverse range of plasmonic nanostructures can be fabricated for various purposes which include nano-antennas, gas sensing and graphene photovoltaics.

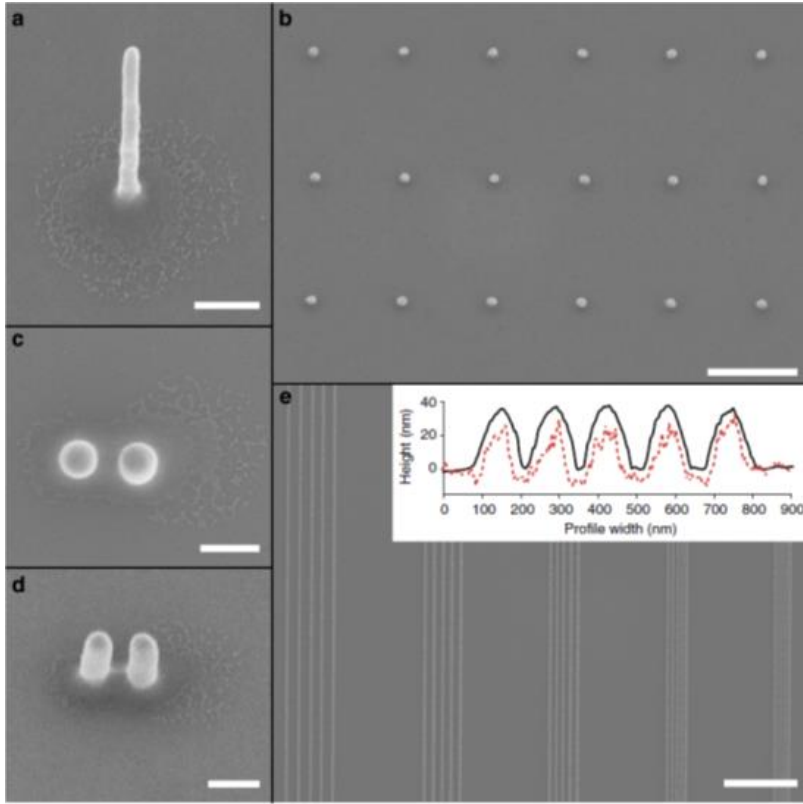


*Figure 8: SEM micrographs of printed nanostructures with dimensionalities from 0D to 2D. (a) Gold nanopillar of diameter ~50 nm and aspect ratio of ~17 (Scale bar, 200 nm). (b) Top and (c) side view of nanopillars printed subsequently at 200 nm center-to-center distance (scale bar, 200 nm). (d) 80-nm wide dots printed into a 1-μm lattice constant array (1 μm scale bar). (e) Printed tracks with pitch sizes of 250, 200, 150, 100 and 75 nm (scale bar, 2 μm). The inset shows AFM (full black lines) and SEM (red dashed lines) profiles of 150-nm pitch size. The height of AFM profiles is given in nanometers. The SEM profiles are in arbitrary units. Tracks have reproducible heights of ~40 nm and are well separated [58].*

Similarly, [131,132] were successful in electrohydrodynamic atomization in the cone jet mode to deposit gold nanoparticles along 110 $\mu$ m lines which then aggregated into 75 $\mu$ m wide sub-tracks within the primary printed line. The observation was attributed to the Bénard–Marangoni effect. Innovative work described in [133] combined heated extrusion with drop on demand electrohydrodynamic printing to generate high resolution, high aspect structures with wax. The wax was heated to 110 °C and extruded through a 50 $\mu$ m nozzle whereupon; a waveform generator was used to induce microdroplet formation from the wax meniscus and deposited onto a substrate 130 $\mu$ m away from the tip. The droplet size was found to decrease

from 15 $\mu\text{m}$  to 7 $\mu\text{m}$  as the voltage increased (800-850v) while the printing frequency increased from 6 to 22Hz. Further build-up of the pillar like structures was inhibited by electric field distortion which was linked to the small standoff height of 130 $\mu\text{m}$ .

Alternatively, [56] used the drop on demand electrohydrodynamic printing technique to precision load drug micro-reservoirs made of PDMS with picograms/micrograms of drugs at high resolutions of 20 $\mu\text{m}$  by means of a microscope oriented in an overturned position to allow for accurate distribution into an array of micro-reservoirs measuring 8 pico-litres in volume. They were able to control the amount of drug they could load by varying the concentration of the printing ink or by changing the flow rate (0.25 to 0.5  $\mu\text{l min}^{-1}$ ) at which the ink was pumped into the needle. Increasing the flow rate brought about an increase in droplet diameter from 80 to 150  $\mu\text{m}$  at a fixed applied electric field strength of 1.5 Kv /mm. Varying the electric field strength from (2.5 to 4.5kV) at a fixed flow rate of 3  $\mu\text{l min}^{-1}$  revealed an inverse relation between droplet diameter and electric field strength. The droplet resolution drop from 400 $\mu\text{m}$  to 25-30 $\mu\text{m}$  as the electric field strength intensified from 1.2 to 1.6 kV/mm.

## **2.13 Electrohydrodynamic atomization of ceramics and polymers**

Researchers in [134] were able to spray pattern 100 layers of zirconia suspensions in a controlled manner to form a wall that measured 5mmx1.2mmx0.14mm (before sintering). The wall thickness after sintering was measured to be 100 $\mu\text{m}$  with further droplet depositions

being hindered by dielectric effect as the ceramic structure was built up vertically. Worked reported in [135] used electrohydrodynamic atomization to print pattern 50 $\mu$ m continuous lines of carbon nano-suspension. Further work by [136] showed that it was possible to simultaneously electrohydrodynamically coaxial print two silica suspensions that contained two monodisperse sized nanoparticles- one 20nm while the other six times larger at 120nm. They were successful in printing 80 $\mu$ m wide lines using a continuous jet in the cone jet mode. Transmission electron microscopy of the printed lines revealed that the solutions mixed in a tumultuous manner while engaged in the cone jet mode which led to irregular particle orientation along the printed silica line.

Studies in [137] reported work with nano hydroxyapatite and outlined the process parameter confines within which either electrospray mode or electrohydrodynamic printing mode is dominant. They pointed out that as the deposition height was reduced from 20mm to 0.5 mm, a shift in mode was observed from electrospraying at 20mm to printing at 0.5mm. The various transient modes (dripping, microdripping, and rapid micro-dripping, unstable and stable jetting) that exist between the electrospraying mode and electrohydrodynamic printing mode were also studied. Additionally, [138] also described in further work how PMSQ and PEG could be used to create structures and varied in situ during the printing process. Co-axial direct write of encapsulated structures was also demonstrated.

## **2.14 High resolution printing of transparent electrodes and meshes**

Traditionally transparent electrodes were made out of metal oxides at high temperatures inside vacuum chambers. These oxides made the transparent electrodes brittle and along with

the cost of fabrication within a vacuum led to the pursuit of cheaper more efficient substitute methods. Studies in [61] proposed an alternative method for the manufacturing of transparent electrodes which are vital components of most optoelectronic devices. They fabricated a transparent electrode by EHD printing a fine grid measuring less than 10 $\mu\text{m}$  in width out of silver nanoparticle ink. The gap between consecutive grid lines was varied to study the effect of gap distance on the resistance and optical properties of the printed grid. They identified that a line to line gap distance of 150 $\mu\text{m}$  was necessary for an appropriate compromise to be reached between good optical properties and favourable electrical properties for the sheets of transparent electrodes that were printed.

The optical transmittance results revealed that as the line-to-line gap reduced from 300 $\mu\text{m}$  to 50 $\mu\text{m}$  the transmittance fell from 86% to 67% at a single visible wavelength of 550nm. Nevertheless at gap distances of 150 $\mu\text{m}$  the transmittance values were consistently at 80%. The printed silver sheets were 8.9 $\mu\text{m}$  thick and had a resistivity of 78.2 $\mu\Omega\text{cm}$  (4.87 $\Omega\text{sq}^{-1}$ ). The also authors noted that predicted optical transmittance values and electrical resistance values for the printed transparent electrodes digressed slightly from measured values due to minor variations in width (7.5 $\mu\text{m}$ ) and height (1.46 $\mu\text{m}$ ) of the silver lines printed which was attributed to the electrohydrodynamic technique being a liquid based technology. Transparent grids were also printed with the piezoelectric inkjet printing technique to illustrate the clear advantage the electrohydrodynamic printing technique has over traditional patterning techniques. The grids had a line width of 50 $\mu\text{m}$  and were observable to the human eye which was in contrast to the less than 10 $\mu\text{m}$  lines produced by the EHD technique.

Similar work was attempted [139] with silver ink and invisible metal meshes for electromagnetic shielding purposes. They reported similar printed line widths of less than  $10\mu\text{m}$  ( $9.72\mu\text{m}$ ) with a printed line height of ( $1.04\mu\text{m}$ ). Yet the difference in their work lay in the optimum line to line gap distance of  $300\mu\text{m}$  which is twice as much when compared to the proposed  $150\mu\text{m}$  by [61]. Their silver meshes also had optical transmittance values that were slightly higher at (88%) while those printed by [61] were capable of an optimum of 80%. The electrical resistance properties of the silver meshes printed by [139] were also dissimilar at reported values of less than  $7\Omega\text{sq}^{-1}$  while those of [61] were  $4.87\Omega\text{sq}^{-1}$ . The difference also extended to the printing conditions which were markedly different for both studies. Novel work in [140] described a hybrid approach to the fabrication of transparent electrodes in optoelectronic devices where EHD jet printing was used along with brush painting. A silver grid (pitch= $300\mu\text{m}$ ) with a measured printed width of  $7.5\mu\text{m}$  was rooted within a film of indium tin oxide nanoparticles (average particle size =  $20\text{nm}$ ) that was brush painted on. This resulted in a sheet resistance of ( $1.4\Omega/\text{square}$ ) with a resistivity of ( $4.2010^{-5}\Omega\text{-cm}$ ) while maintaining high values of optical transmittance at (83.72%).

The investigations [139] and [61] used similar materials (Ag 70% nanoparticle content printing ink) at a viscosity of  $4300\text{cP}$ . The printing ink was pumped into the print head at a flow rate of  $150\text{ nl/min}$  in both studies but [61] used a much larger printing head nozzle ( $150\mu\text{m}$ ) while [61] used a smaller nozzle of  $100\mu\text{m}$ . Despite the larger nozzles, [139] printed at low standoff heights of  $1\text{mm}$  and at a low applied voltage of  $1\text{kV}$ . In addition to thin printing nozzles, [61] operated at double the applied voltage of  $2\text{kV}$  at a standoff height that was five times higher ( $5\text{mm}$ ) than those used by [139]. The substrates that the silver meshes

were printed on was also different for both studies, [139] printed their meshes on polyether sulfone (PES) while [61] printed on glass substrates.

High viscosity silver ink (10,000 mPas) containing 78.9wt% of silver nanoparticles was used by [61] to print 84 silver electrodes with a high aspect ratio for use in the manufacture of solar cells via a non-contact printing technique. The 20 $\mu$ m wide, 0.81 $\mu$ m high electrodes were printed in the continuous jet mode under an applied voltage of 1.8 kV and a flow rate of 0.5 $\mu$ l/min on the pure silicon wafer surface. To study the effect of surface energy and contact angle, printing was done on three different surfaces that included two hydrophobic surfaces 1) a silicon wafer with Hexamethyldisilazane treatment, 2) a silicon surface with Decyltrichlorosilane treatment and 3) a bare silicon wafer. They printed twice over the silver electrodes in an attempt to increase the height of the electrodes while keeping the width to a minimum. At a printing speed of 4000mm/min, the bi-fold printing resulted in an increase in line width from 20 $\mu$ m to 47.9 $\mu$ m with a 3.5 fold increase in the printing height to 2.9 $\mu$ m for the SW-DTS surface while the opposite was true for the SW-HDMS surface electrodes where the same height (2.9 $\mu$ m) was reported with three fold increase in width to 60.9 $\mu$ m. Despite the novel approach, the electrohydrodynamically printed solar cells had similar open circuit voltage (Voc) and short circuit current density (Jsc) values of 0.61, 32-33 mA/cm<sup>2</sup> which is comparable to solar cells manufactured through conventional means. Moreover, the electrohydrodynamically printed solar cells behaved less efficiently.

Findings in [141] acknowledged the failings in electrohydrodynamically printed solar cells and attributed it to the quality of the silver printing paste used which results in either a low packing density or a high contraction in printed volume. To investigate this they prepared a silver paste that consisted of two distinctly different silver particles sizes. The small particles measuring (0.13–0.35  $\mu\text{m}$ ) would permit an even flow of the silver paste through the printing nozzle but would hinder the effective contact between the silver electrodes and the emitter layer of the crystalline solar cell. To offset this, large silver particles measuring (0.9–1.4  $\mu\text{m}$ ) were uniformly mixed in to the paste. They were able to successfully print silver electrodes (60 $\mu\text{m}$  wide and 51.50 $\mu\text{m}$  high) with a height to width aspect ratio of 0.86 and reported a solar cell efficiency of 16.72% which is slightly more than the solar cells printed with diluted commercially available silver paste (13.7%). The emitter sheet had a resistance of 60  $\Omega/\text{sq}$  with open circuit voltage (Voc) and short circuit current density (Jsc) values of 616.8 mV and 34.61 mA/cm<sup>2</sup>.

## **2.15 Electrohydrodynamic printing of field effect transistors, ferroelectric memory devices and multi-layer interconnection structure**

In the field of organic integrated devices [62] were recently successful in producing organic field effect transistors by electrohydrodynamically print patterning a number of surface modified substrates in the microscale with Poly (3-hexylthiophene). The substrates had their surfaces modified with five different thin film polymers and self-assembled monolayers (CH3-terminated SAM (ODTS), F-terminated SAM (F-SAM), PVP with crosslinking (cPVP), and cyclic olefin copolymer (COC)) treatment to investigate the effect of surface energy on printed line width. They showed that depending on the type of surface treatment, a

decrease in surface energy brought about an increase in contact angle for dispensed Poly (3-hexylthiophene) which resulted in narrower EHD-printed lines. Under a printing flow rate of (0.5 $\mu$ L/min) and an electric field of ( 1.85kV) at a printing speed of 25mm/sec, a CH<sub>3</sub> terminated self-assembled monolayer proved to be the best surface onto which Poly (3-hexylthiophene) could be printed with a reported line width of 47 $\mu$ m using a print head with a 100 $\mu$ m wide nozzle. Researchers in [142] produced their field effect transistors with a single directly written semiconducting Zinc oxide nanofiber onto flat gold electrodes embedded on a silicon substrate. They showed further direct write versatility by direct writing the same zinc oxide nanofibers (500-1500nm) across two vertical micro pillars. They claimed that this technique could be used to incorporate both organic and inorganic nanofibers into micro-electro-mechanical structures and microelectronics devices. Studies in [143] described the fabrication of n- and p-type graphene channel FETs (Field Effect Transistors) and junctions on a single substrate by near field electrospinning functional polymers PEI (Polyethylene imine) which was responsible for n-type doping and PEO (Polyethylene oxide) for p-type. The electrospun fibres are used to pave the nano-sized p and n type graphene channels in addition to acting as doping agents. The fibres are subsequently removed with deionized water. Work reported in [144] described the printing of an array of copper nanowire electrodes measuring 710nm in width with an electrical resistivity of 14.1  $\mu$  $\Omega$  cm and went on to produce field effect transistors using these electrodes. They reported a maximum field-effect hole mobility of 0.16 cm<sup>2</sup> V<sup>-1</sup> s<sup>-1</sup> and an on/off current ratio of  $7.5 \times 10^6$

Studies in [145] successfully developed ferroelectric memory devices with positional addressable semi conducting polymer (poly (3-hexylthiophene) nanowires for use in flexible and foldable organic devices. A strong electrostatic field was used to deposit and align the organic nanowires in a controlled and precise manner in the continuous jet mode. The

technique permitted between 1-16 nanowires to be printed in arrays between the source and drain electrode that measured 300nm in diameter. Similarly, [146] patterned silicon substrates with polydiacetylenes embedded polystyrene nanofibers. The diacetylene monomers were dispersed in polystyrene inks and patterned at nanofiber width that varied from (57.32 - 167.49nm) depending on the concentration, applied voltage and standoff height. They reported that increasing the concentration and reducing applied voltage led to poor fibre width. Alternatively, [147] patterned a photonic crystal surface with micron sized droplets of (NOA74) an optical light-curable adhesive. This was done to achieve an unbroken adhesive layer between the photonic crystal and glass cover.

Work described in [148] demonstrated how multiple materials could be electrohydrodynamically direct written to construct a multilayer interconnection electrical component that consists of an insulator (PVP) sandwiched in between a lower and an upper conductive track that are printed perpendicularly with respect to each other. The silver tracks measuring (288 $\mu$ m) wide were electrohydrodynamically printed alternately with measured resistance values of  $1.33 \times 10^8 \Omega \cdot \text{m}$  for the bottom silver track and  $1.39 \times 10^7 \Omega \cdot \text{m}$  for the top track.

## **2.16 Electrohydrodynamic printing of Memristors**

Similar work conducted by [149] showed that devices such as memristors could be manufactured using this method to replace the traditional transistor. Though the proposed

hybrid approach to the fabrication of these low powered, non-volatile devices which differed slightly from the approach adopted by [148]. The fabrication route outlined in [149] involved spin coating the semiconductive zinc oxide layer on to the lower conductive track which was then subsequently electrohydrodynamically printed upon with the upper silver conductive track. In addition they were able to print their bottom silver electrodes at much higher line width (84 $\mu$ m) when compared to (288 $\mu$ m) reported by [148]. The upper electrode was intentionally printed at a much lower line width of (370 $\mu$ m) using different operating parameters. Electrical characterization of the memory device revealed a measured variation in the voltage-current characteristics which points to behaviour which is indicative of bipolar resistive switching thus showing applicability in analogue computation.

Further work by [150] was attempted with zirconium oxide nanostructures as the spin coated thin film sandwiched in between two EHD printed silver electrodes. The device demonstrated resistive switching behaviour within a +5 to -5V range and a possible explanation for the resistive switching behaviour was offered. They claimed that on application of a positive voltage to the top positive electrode, mobile silver ions are generated which then travel through the zirconium oxide layer towards the lower negative electrode leading to the formation of thread like conductive conduits through the zirconium oxide layer. They linked these pathways to the oxidation – reduction reactions that take place at the interface between the zirconium oxide and silver electrode. The high resistance (ON) and low resistance (OFF) states of the device are determined by these reactions. Researchers in [151] used the same materials (zirconium oxide and silver) when fabricating flexible memristors but instead of spin coating the zirconium oxide they electrohydrodynamically sprayed it on top of the

electrohydrodynamically printed silver lines. They reported resistive switching behaviour for their device within a +3 to -3V range. Similarly, [152] fabricated memristors with ITO as the lower electrode and electrohydrodynamically spraying the active layer (zirconium oxide). They stated that their device could operate at a number of operational voltages that were less than  $\pm 10V$  with a high ON/OFF ratio of greater than 100000:1. Alternatively [153] attempted to fabricate a memristor (Cu/  $TiO_2$ /Ag memristor ) with metal electrodes from two different materials (Silver and copper) with a  $TiO_2$  thin film electrohydrodynamically sprayed uniformly in between the two EHD printed electrodes.

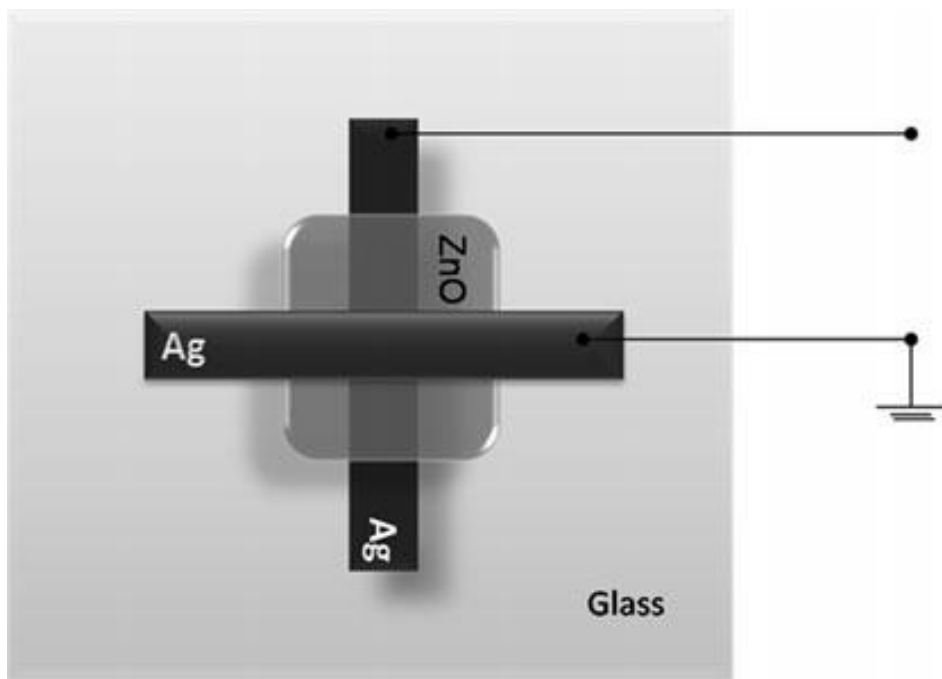


Figure 5. Device structure of memristor [149]

## 2.17 Electrohydrodynamic printing of transistors

Investigators in [154] also adopted the same hybrid approach to produce thin film transistors by combining both electrospray and electrohydrodynamic inkjet printing. The conductive tracks were electrohydrodynamically printed while the semiconducting dielectric layers ( $ZnO$  and  $SiO_2$ ) were electrosprayed. The source, drain and gate electrodes were printed in the continuous jet mode on to glass substrates to yield silver lines measuring  $50\mu m$  in width pre-sintering and  $70\mu m$  post sintering. Embedded between the source, drain and gate electrode is a  $300nm$  thick layer of  $SiO_2$  coupled with a  $100nm$  thick layer of  $ZnO$ . The irregularity in thicknesses of the respective semiconductive layers was linked to the non-uniform particle size. An attempt is also made at improving print head design to minimize disturbances caused by conductive electrodes placed inside glass capillaries. Instead they suggested the use of a hollow conductive electrode to be inserted into  $80\mu m$  sized tapered glass capillaries.

An approach in [155] described the fabrication of a thin film transistor by electrohydrodynamic printing and thermal evaporation. A continuous electrohydrodynamic jet was used to deposit a  $60\mu m$  wide Zinc-Tin Oxide lines onto a  $300 nm$  thick  $SiO_2$  gate insulator using a  $100\mu m$  sized needle. They pointed out that in addition to applied voltage the temperature and printing speed are important parameters to be considered when trying to obtain highly resolved printed lines. At a fixed printing speed of  $5000\mu m/s$ , the highest substrate temperature ( $75^\circ C$ ) produced the finest line width and this was ascribed to the increased diffusion and evaporation of the solvent. For a fixed temperature of  $50^\circ C$  the substrate speed was found to have the greatest influence on printed line width with a  $8000\mu m/s$  substrate speed yielding a  $60\mu m$  line width. Investigation of the electrical properties of the EHD printed thin film transistors revealed that there was a threefold increase in mobility

( $9.82 \text{ cm}^2/(\text{V s})$ ) when compared to conventional spin coated ZTO TFT with 50nm channel thickness and also higher than most inkjet printed versions which have a mobility in the range of ( $2.60\text{--}4.98 \text{ cm}^2/(\text{V s})$ ). Additionally, the ZTO TFT exhibited good ohmic contact and hysteresis behaviour. Researchers in [156] were able to fabricate thin film transistors by patterning SiO<sub>2</sub>/Si wafers with a transparent semiconductor material (indium zinc oxide) and an optoelectronic semiconductor material (gallium nitride) at much higher line widths ( $1.5\mu\text{m}$ ) than previously reported. The current mobility measured to be  $3.7 \text{ cm}^2\text{V}^{-1}\text{s}^{-1}$ .

Investigators in [157], printed both high (25,000 mPas) and low viscosity (10–17 mPas) silver nano-ink on four different substrate materials (Glass, PVP coated glass, Polyethylene terephthalate (PET), polyethylene naphthalate (PEN film)) to produce an array of 300 transistor source and drain pads. Continuous droplets were produced by the application of a 5ms switching, 100Hz alternating voltage to electrohydrodynamically print continuous conductive lines. They found that printing lines with low viscosity silver ink on glass slides led to wide lines and this was linked to the hydrophilic property of the glass slide that promotes spreading. Ink spreading was not observed when the same low viscosity ink was dispensed onto PVP coated a glass slide which was believed to possess a surface roughness that prevented spreading thus leading to lines measuring 75–80  $\mu\text{m}$ . Conversely, printing with high viscosity silver ink led to wide, straight lines (110  $\mu\text{m}$ ) on the glass substrates and much narrower lines on the PVP coated slides (40–50  $\mu\text{m}$ ). Line printing on plastic substrates proved to be better in terms of reproducibility and resolution as they were able to produce lines measuring 50–55  $\mu\text{m}$  on PET and 20–25  $\mu\text{m}$  on PEN films. The fine printed lines on PEN films were attributed to the low surface energy of polyethylene naphthalate which

restricts wetting and thus spreading when compared to Polyethylene terephthalate and PVP. In general, low viscosity silver ink required low AC voltage but resulted in wide lines while high viscosity generated the narrowest line widths. The work in [158] used a high molecular weight polymer (polyethylene oxide) dissolved in a fast evaporating solvent (ethanol) to build micro-sized three dimensional spiral coils (n-3-50)(loop diameter = 4-60 $\mu$ m). They exploited the whipping instability that usually inhibits the stability of the electrified EHD jet to lay down concentric layers of polyethylene oxide to generate the fibrous coils. They were able to control the periodicity of the looping by increasing the collector speed which resulted in less number of deposited loops. Increasing the concentration led to thicker jets with a fewer number of coils but with wider ellipsoidal diameters.

Furthermore [159] described how nano-silver ink could be used in EHD drop on demand technology to engineer new age materials such as metamaterials. These composite materials are used to achieve tetrahertz frequencies. They were able to sandwich EHD printed 'I' shaped silver electrodes between two layers of polyimide. The printed electrodes were 180nm thick with a length of either 160 $\mu$ m (0.5 THz) or 110 $\mu$ m (0.7 THz) depending on the intended resonant frequency. They proved that they could reproduce these electrodes consistently at individual electrode gap distances of 5 $\mu$ m. At a pulse width of 1ms and an EHD jetting frequency of 100Hz, the applied voltage of 0.5kV resulted in continuous stream of droplets that coalesced to form unbroken lines on the silicon wafer. The metamaterial produced had a high refractive index of 18.4.

Studies described in [160] showed how EHD drop on demand can be used in the manufacturing of LCD screens by EHD printing su8 spacers to separate out the liquid crystal

cells as means of replacing conventional silica beads or column spacers. A function generator was used to create a square wave at an applied pulsed voltage of 1.75kV. At frequencies of 2 kHz, 35 $\mu$ m sized droplets were produced at 0.5ms cycles. The printed spacers were 35 $\mu$ m wide with a inter spacer distance of 200 $\mu$ m. Characterization of the liquid crystal cells using the EHD printed su8 spacers indicated a distinct advantage over conventional twisted nematic liquid crystal cells manufactured with silica beads when voltage-transmission and response times were compared.

## **2.18 Near field electrospinning**

Near field electrospinning is capable of generating and spatially aligning nanofibers for a variety of applications, some of which include (self-powered sensing elements MEMS) [161], (energy harvesters composed of ordered poly(vinylidene fluoride) (PVDF)/poly(g-methyl L-glutamate) (PMLG) composite fibres that are direct written onto poly(ethylene terephthalate) substrates [162] , near field electrospun polyaniline nanofibers to create ammonia gas sensors while in further work they doped polyaniline nanofibers with palladium nanoparticles to generate hydrogen chemresistor sensors [163], (light emitting prototype conjugated polymer nanofibres poly[2-methoxy-5-(2-ethylhexyloxy)- 1,4-phenylenevinylene] (MEH-PPV) ) [164]. Near field electrospun silver nanowires embedded within Polyvinylpyrrolidone (PVP) to form composite PVP/silver nanowire fibres for potential use as transparent electrodes [165].

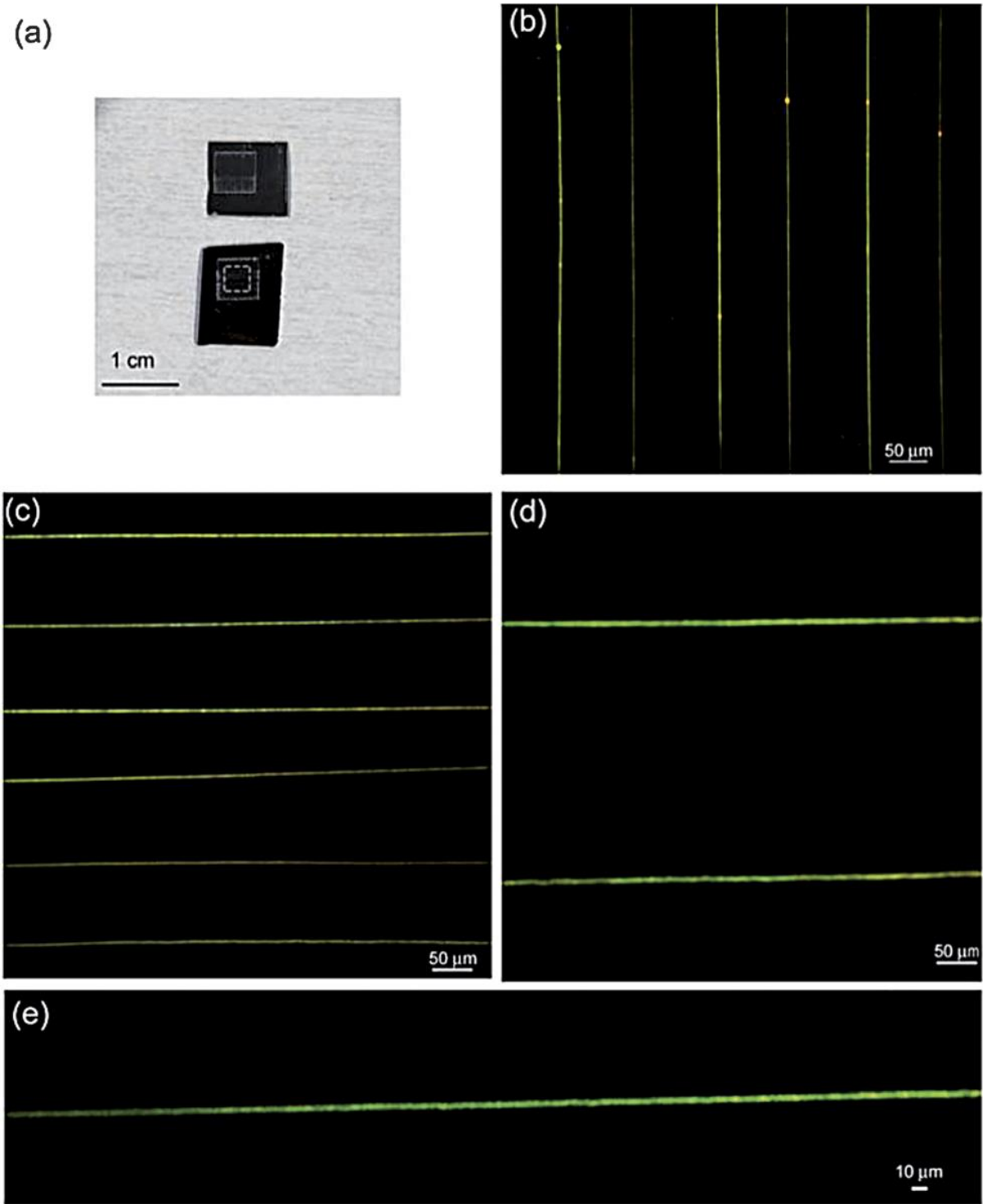


Figure 9: (a) Pictures of the fiber arrays realized by NF-ES. The dashed box highlights the region with nanofibers. (b)–(d) Confocal fluorescence micrograph of an array of emitting nanofibers made by NF-ES. (e) Single fiber confocal fluorescence image [164].

An attempt in [166] described a modified form of near field electrospinning where the jetting is initiated by a sharp tungsten probe that is used to jab a droplet of the printing ink to extract a thin strand of the printing ink which is then subsequently sustained through the applied electric field. They were successful in printing depositing PVDF in a variety of configurations in the micro and nano scale using this technique. Similarly, [167] employed the same technique as they constructed dielectric-loaded surface plasmon polariton waveguides (DLSPPWs) through near field electrospinning of polyethylene oxide nanofibers onto gold substrates.

Researchers in [168] explored the potential use of electroactive polymeric materials such as PVDF to generate microstructures for the large scale manufacturing of sensors and actuators. A successful attempt was made by [169] to near field electrospun polyvinylidene fluoride (PVDF) piezoelectric nanofibers which had multiwalled-carbon nanotubes (MWCNT) mixed in. The deposited fibres were investigated for actuation deformation when subjected to numerous electric fields. They found that degree of polarization and morphology of the piezoelectric fibres could be regulated by through the printing standoff height, speed of the stage and applied DC voltage. They [170] were successful in near field electrospinning amorphous titanium dioxide nanofibers (200–400 nm) onto a silicon wafer covered by a film of silicon dioxide. Additionally, [171] described the use of near field electrospinning to deposit crack-less titanium dioxide nanofibers (300-500nm) in the fabrication of nitrogen dioxide sensors with a detection limit as low a 1ppm

## 2.19 Mechano-electrospinning

Researchers in [172] described the use of a technique called mechano-electrospinning to direct write piezoelectric polyvinylidene fluoride (PVDF) on to pre-stressed elastomeric substrates. The nanofibers were deposited at stand-off heights that ranged from 4-10mm from needles with orifices measuring 260 $\mu$ m at an applied voltage of 1.5kV. They claimed that they could achieve better control over line width, fibre morphology and fibre placement through the mechanical drawing out of fibres from the taylors cone as they are deposited on to high speed X-Y movable stage. The manipulation of process parameters can tune both the fibre width and morphology while fibre placement is enhanced through the drag force that is exerted when the fibre is drawn out at high speed on to the substrate. They were successful in producing stretchable piezoelectric nanogenerators and pressure sensors.

Consequently, [173] discussed three main modes of the mechano-electrospinning technique, namely mapped direct-writing (MDW) mode, leap direct-writing (LDW) mode and helix direct-writing (HDW) mode. Mapped direct writing is similar to near field electrospinning in that it uses the linear segment of the electrospun jet to deposit fibres in the micro and nanoscale. Leap direct writing is used to generate bead on string structures through the interplay of mechanical drawing, viscoelastic and electric field forces. This is made possible only at jet lengths that are greater than 0.5mm but less than 2mm with a substrate velocity lower than 150mm/s. Helix direct-writing exploits the whipping and buckling instabilities to direct write serpentine structures. They identified the relationship between the mechanical drawing force exerted by the jet impinging on a substrate moving at a velocity to be vital in manipulating the printed line width, positioning and alignment of deposited fibres.

Studies conducted by [174] led to findings which indicated that the composition of the solvent and the concentration also had a role to play when generating continuous fibres of Poly (amide-co-imide) PAI (torlon)/Poly (trimellitic anhydride chloride-co-4, 4'-methylene dianiline) (PTACM) through mechanoelectrospinning. The fibres tended to coil when the polymer blend concentration reached 26% dissolved in 6:4 solvent ratio of DMSO/THF. Fibre size was also found to decrease as the concentration decreased from 30% -26%. In further work [175] they proposed a one-step continuous process to uniformly coat the polymer fibre with silver nanoparticles.

## **2.19 Electrohydrodynamic jetting of melt extrusion**

Studies by [176] [177] and [178] described the use hot melt extrusion coupled with electrohydrodynamic jetting to direct write through melt electrospinning. Work by [176] showed that fibrous 3D scaffolds with fibre diameters that varied between (8-138 $\mu$ m) were possible using the polymer poly (2-ethyl-2-oxazoline). Principal operating parameters such as the extrusion heating temperature, feeding pressure, applied voltage and collector distance were methodically studied along with nozzles of varying diameters (23G, 337 $\mu$ m)(25G, 260 $\mu$ m)(27G, 210 $\mu$ m)(30G, 159 $\mu$ m). The investigation revealed that increasing the feeding pressure and heating temperature resulted in fibres with large diameters with the applied voltage playing an insignificant role. Thinner fibres were possible when the nozzle-substrate stand-off height was increased. They identified that (25G, 27G and 30G) were the ideal nozzles for the steady production of homogenously dispersed fine fibres (10-50 $\mu$ m) as the previously mentioned process parameters are systematically varied.

This investigation [177] used poly ( $\epsilon$ -caprolactone) to lay down successive layers of PCL fibres (20 $\mu\text{m}$ ) to produce tightly packed mesh woven (weaved at 60° and 90° orientations) scaffolds (pore size = 20 $\mu\text{m}$ ) for tissue engineering applications. Further on in [179], initial investigations into collector speed and shape revealed that hollow tubular scaffolds were possible by melt electrospinning fibres (20 $\mu\text{m}$ ) onto rotating tubular collectors. For this particular technique the fibre winding angle was pointed out to be the most vital for control over the mechanical properties of the scaffold and the pore number, size and shape. They also stressed that the electrospinning jetting speed needs to match the translational speed of the rotating collecting drum for the precise placement of fibres. On the other hand fibre diameter was directly linked to a combination of rotational drum speed of the collectors and the horizontal translating speed which produced a drawing out effect resulting in thinner fibres.

The effectiveness of the scaffold was confirmed when cell studies using three different cell types (Primary human osteoblasts (hOBs), mouse osteoblasts (mOBs) and human mesothelial cells) showed that the cells penetrated the fibrous scaffolds, attached and proliferated to yield a cell viability of > 90%. The homogenous fibrous network facilitated excellent spreading morphology as displayed by Primary human osteoblasts (hOBs) cells which were shown to extend in the gap between two fibres. Moreover, a vital link between the geometry of the pores which in turn is related to the fibre winding angle was established. The tissue lengths present in between interwoven fibres decreased as the fibres moved further apart from each other at wider winding angles. Investigators in [180] melt electrospun poly ( $\epsilon$ -caprolactone) scaffolds with fibre diameters of (7.5  $\pm$  1.6  $\mu\text{m}$ ) with an average interfibre spacing of 46  $\pm$  22  $\mu\text{m}$ . Subsequent cell study work with primary human dermal fibroblasts revealed that the

cells were able to penetrate deep into the scaffold. Moreover, vital dermal extracellular proteins were generated and uniformly dispersed throughout the cell laden scaffolds along with fibronectin and collagen type I.

This work [181] represents an investigation into the effect of amending collector shape and form (flat structured surface, raised structured dome substrate and smooth flat surfaces) on the accuracy and control of deposited fibres and subsequent scaffold pore size (400 $\mu$ m). The practical facets of melt electrospinning poly ( $\epsilon$ -caprolactone) which has a much lower melting point than poly (2-ethyl-2-oxazoline) were also taken into consideration. An important distinction between solution electrospinning and melt electrospinning was made as they described how structures were directly written by this process. In melt electrospinning the melt electrospun jet hits the surface and then proceeds to buckle under compressive forces which bring about random coiling at the point of impact. On the other hand, solution electrospinning jets lead to wider and more exaggerated coiled depositions due to whipping. They were successful in producing varied macroporous architectures with fibre diameters of (30-40 $\mu$ m) on patterned conductive substrates and this was attributed to focused electric fields that led to the highly selective deposition and alignment of fibres along the contours and curves of the conductive wire meshed substrates.

They struggled to heighten the structures due to a charge build up in the fibres as layers of PCL were printed on. The accumulation of charges deflected the incoming melt electrospun PCL fibres to the boundaries of the structures they were trying to produce. Changing the nozzle diameter also highlighted the need for equilibrium to be achieved between mass flow

of melted polymer and fibre pull out due to electrohydrodynamic effects. Inconsistencies in this balance was attributed to observed dynamic swaying of fibres and irregular jet pulsing.

This [178,182] research using the same material (polycaprolactone) exhibited how a range of periodic three dimensional structures could be produced consistently at much higher line widths of (< 10 $\mu$ m) when compared [176] [177]. Additionally, they confirmed and reiterated the need for a balance to be achieved between plotting speed and the rate at which fibres are extracted from the tip of the needle which was also highlighted by the findings of [176]. Similarly, nozzle dimensions were also shown to affect the printed line widths as they showed that reducing the nozzle diameter from 152.4 $\mu$ m to 51  $\mu$ m brought about a two-fold increase in printed line widths from 25 $\mu$ m to 13 $\mu$ m for the lowest plotting speeds. Increasing the plotting speed caused the line width to increase further from 25 $\mu$ m to 17 $\mu$ m (1.2 to 2.4mms<sup>-1</sup>, for the 152.4 $\mu$ m needle) and from 13 $\mu$ m to 7 $\mu$ m (0.8 to 2 mm s<sup>-1</sup>, for the 51 $\mu$ m needle). The research findings reported in [183] further validated this link between fibre stretching and substrate speed. Through simulations and experimental work they were able to identify three main states that occur during the impinging of an electrified the jet on a moving substrate, namely “catenary”, “heel” and “rotation”.

Interestingly [184] demonstrated another variant of this technique that involved the merging of drop on demand technology with melt extrusion to pattern microcantilever gravimetric sensors with 10 $\mu$ m sized droplets of molten polyethylene. A 0.25 Hz pulse voltage of 250-500V at a stand-off height of (20-40 $\mu$ m) was used to generate controlled droplet depositions

that could be varied in diameter between 2-27 $\mu\text{m}$  by manipulating the applied voltage. By accurately electrohydrodynamically placing the droplets on the silicon cantilever they were able to notice a change in the resonant frequency of the cantilever which could then be used to make mass measurements. They also investigated the effect of adding droplets at various distances from the freely suspended end of the cantilever and observed changes in resonant frequency that was inversely related to the distance. They eventually concluded that the sensitivity of the cantilever gravimeter to changes in mass increases when the droplet is accurately deposited at the freely suspended end of the cantilever.

## 2.20. Scaffold design

From an engineering and biological point of view, tissue engineering holds many challenges which span beyond the strict definition of cells and scaffolds. Perhaps the most critical issue of all is to understand and to define the native tissue which is meant to be replaced. In fact, the function of the tissue must be completely understood, biologically and biomechanically, in order to replace it optimally. The mechanical characterisation of biological tissue is, however, often complex due to testing conditions, the tissues' inherent anisotropy, and limited sample life-cycle. Furthermore, the mechanical signals regulating tissues must also be ascertained.

At a macroscopic level (mm range) the shape and composition of the scaffold will determine its cytotoxicity and the ability of the cells to penetrate its structure. At an intermediate level (100  $\mu\text{m}$ ), the pore size, orientation, interconnectivity and surface chemistry will determine

cell differentiation and proliferation behaviour as well as the supply of nutrients and the removal of waste products. At a microscopic level (1 $\mu$ m), the local surface texture and porosity will affect protein adsorption and cell adhesion. Ideally, the optimum pore size can vary from 5  $\mu$ m to 350  $\mu$ m depending on cell type while pore interconnectivity should be maintained within 200  $\mu$ m from the blood supply in order to provide for mass transfer of oxygen and nutrients. The surface of the scaffolds needs to be surface treated to create nanostructured irregularities less than 100nm to mimic the nanoarchitecture of natural tissues[185].Thus a thorough characterisation of each level of the scaffold and a proper design are crucial for understanding its behaviour as a tissue engineering construct.

The specific cell signalling that is triggered by the surrounding environment which in this case is a scaffold will ultimately determine if the scaffold will eventually turn into an integrated tissue. Initially the cell types need to attach externally to the scaffold surface and then proceed to migrate within it [186]. This is only possible if the scaffold has cell adhesion sites dispersed within in it throughout the scaffold in the appropriate density to promote cell migration. After the scaffold is populated by cells, proliferation and differentiation need to take place to produce the replacement tissue. Integrins are responsible for anchoring onto the extracellular matrix while simultaneously eliciting cues for cell differentiation or proliferation along with cytokines and growth factors. The dynamic nature of the extracellular matrix makes it a challenge to replicate. Mechanotransduction pathways initiated by mechanical stimuli allow the cells to remodel the tissue. The proteins on the extracellular matrix facilitate cell attachment via the integrins. The cells can then exert traction forces on the extracellular matrix to stretch the extracellular matrix proteins to reveal binding sites on the protein

structure [187-191]. Cellular mechanotransduction and cell signalling are vital issues that need to be fully understood and considered when designing artificial scaffolds in tissue engineering since it underpins cell differentiation, phenotype and proliferation [192, 193].

## **2.21 Drawbacks of current printing technologies**

The fabrication of scaffolds for better tissue regeneration has attracted a great deal of attention. In specific, three-dimensional (3D) scaffolds that mimic the *in vivo* cellular microenvironment is of fundamental importance to the success of tissue engineered constructs. Both scaffold chemistry and architecture can influence the fate and function of engrafted cells. Traditional methods of producing scaffolds in tissue engineering such as gas foaming/salt leaching, free drying, solvent casting/particulate leaching, emulsification and phase separation result in porous scaffolds with no control of over the internal architecture and interconnectivity with similar hindrances over pore sizes [194,195]. These techniques also require polymer to be processed using a solvent and could in turn leave residues that could prove to be toxic to the cells. In addition, they are also limited in the extent to which bioactive molecules can be loaded within the constructs for targeted release. This was overcome with the advent of a broad group of techniques called (RP) rapid prototyping technology that provided excellent control over internal spatial polymer architecture using a wide range of materials [196].

Fabrication techniques such as sheet lamination involve the use of heat and pressure to sequentially fuse layers of polymer followed by the use of a laser to cut out shapes. This

unfortunately leads to the structures that are too dense with little porosity and are thus incapable of building highly cellular tissues. Fused deposition modelling is limited to only materials with low melting points for them to be melted and extruded. Despite good planer (x-y) control, FDM suffers from poor control over pore height in the third dimension (z-axis) because it is highly dependent on the thickness of the polymer filament being extruded. Moreover, printing layers thicknesses with FDM are coarse with layer thickness that is between 250-700 $\mu$ m. The heat required to make the process work puts a restriction on incorporating bioactive molecules within scaffolds printed with this technique [197]. Additionally, the surfaces of extrude printed scaffolds have a low surface roughness and thus prevent cells from latching on. On the other hand light based fabrication technologies like SLA (stereolithography), 2PP (two photon polymerization) and SLS (selective laser sintering) have been used generate scaffolds and other structures from a range of materials that include biocompatible liquid polymer resin.

Despite line widths that range from 200nm for 2PP to several micrometers for SLA and SLS – these techniques suffer from a lack of flexibility in terms of the structural composition of the intended scaffolds. At any one time only one ceramic can either be sintered in SLS or in the case of 2PP and SLA, one polymer photopolymerized. Thus tailoring scaffolds with multiple polymeric constituents with imbedded bioactive molecules while simultaneously controlling the precise spatial distribution of cells during the fabrication process is still beyond them [198,199]. Despite SLS having the ability to print a wide variety of materials, it is restricted in its ability to control scaffold pore size due to the heterogeneous distribution of powder particle sizes (10- 100 $\mu$ m). Improvements on the laser based direct write technology

led to the development of matrix-assisted pulsed laser evaporation direct write (MAPLE DW) and Biolap™ which are based on the LIFT (laser induced forward transfer) principle. These technologies were designed specifically to deposit biological materials such as cells, DNA and polymer scaffolding material. Unfortunately they have low throughput and are only suitable for two dimensional studies of cell biology and struggle to produce 3D structures [200,201]. Inkjet printing offers high speed and low cost fabrication of tissue engineering constructs but falls short when it comes to printing solutions with high cell densities. The small orifices risk clogging and the high printing speeds cause cell damage [202]. Till today, there is no ideal material for manufacturing tissue engineering constructs at high resolution. The printed line widths or deposited droplet dimensions vary from 85-300 $\mu$ m.

## CHAPTER 3: EXPERIMENTAL DETAILS

### 3.1 Materials

#### 3.1.1 Regenerated silk fibroin

Silks are produced by members of the class Arachnida (over 30,000 species of spiders) and by several worms of the order Lepidoptera, which includes mites, butterflies and moths. Silk Fibroin is composed of fibrous proteins synthesized in the glands of these organisms and is generally composed of Beta-sheet structures due to the dominance of hydrophobic domains consisting of short side chain amino acids in the primary sequence. Silk fibroin polypeptide chains are composed of heavy and light segments of ~390 kDa and ~26 kDa. These segments are held together by disulphide bonds formed at the terminating carbon atoms of each subunit. Hydrophobic interactions characterize the associations of the heavy and light complexes formed.

Tensile strength in silk fibroin is achieved through hydrogen bonding that exists between the  $\beta$ -sheets. The sheets form through hydrophobic interactions that exist between the heavy and light segments. Elasticity and toughness are conferred through a combination of organized hydrophobic blocks and irregularly placed hydrophilic blocks [202]. The silk that is produced by these glands consist of fibroin strands that are embedded in a matrix of a globular protein called serecin. This is responsible for the sheen and texture commonly seen in silk. Fibroin is mostly responsible for the high strength of natural silk (silk I) because of its secondary structure, which is made of several crystalline antiparallel  $\beta$ -pleated sheets. The alanine and glycine rich polymers with amino acid sequences similar to those of collagen pack closely

because of their  $\beta$ -pleated sheet conformation thus greatly increasing the material's tensile strength [203].

### **3.1.2 Polycaprolactone**

Polycaprolactone (PCL) was chosen because it is a slowly degrading polymer (~2-3 years), elutes non-toxic by-products, and is biocompatible as evident through its wide array of FDA approved products (e.g., sutures and drug delivery) [204-207]. PCL degrades via hydrolysis of the ester linkages into water soluble hydroxycaproic acid monomers [204]. It is a semi-crystalline polymer that degrades more slowly than many other biodegradable synthetics [210]. This slow degradation rate allows adequate time for the cells to regenerate native tissue, ideally at the same rate as scaffold degradation. PCL also has a relatively low melting point of 60 °C allowing for easy manufacturing and scaffold fabrication [207, 208]. It is a semi-crystalline, bioerodable polymer that possesses the ideal mechanical properties that are necessary for it to be employed for use as a temporary extracellular matrix for cartilage regeneration. It dissolves in most organic solvents and is capable of undergoing hydrolysis within the body to form water soluble monomers. As a result the polymer has found its way into a number of biomedical devices for applications that include implantable contraceptive devices and staples for wound closure that degrade over time [209, 210].

### **3.1.3 Formic acid**

Formic acid ( $\text{HCO}_2\text{H}$ ), also called methanoic acid, the simplest of the carboxylic acids, used in processing textiles and leather. It is made by the action of sulfuric acid upon sodium

formate, which is produced from carbon monoxide and sodium hydroxide. Formic acid is also prepared in the form of its esters by treatment of carbon monoxide with an alcohol such as methanol (methyl alcohol) in the presence of a catalyst. Formic acid is not a typical carboxylic acid; it is distinguished by its acid strength, its failure to form an anhydride, and its reactivity as a reducing agent a property due to the  $-CHO$  group, which imparts some of the character of an aldehyde. The methyl and ethyl esters of formic acid are commercially produced. Concentrated sulfuric acid dehydrates formic acid to carbon monoxide. Pure formic acid is a colourless, fuming liquid with a pungent odour; it irritates the mucous membranes and blisters the skin. It freezes at 8.4 °C and boils at 100.7 °C [211].

### **3.1.4 Dimethyl carbonate**

It is a perfect methylating agent, carbonylating agent, methoxylating agent and methylolating agent with active chemical properties. Because of its excellent chemical and environmental property, DMC is used as a good solvent for coating, paints, ink and adhesive substituting other commonly used solvents (benzene, xylene, ethyl acetate, butyl acetate). It is an ideal substitute for toxic substances such as phosgene, dimethyl sulphate, and methyl chloroformate. Dimethyl carbonate possesses properties of being non-toxic while also being biodegradable thus making it a green chemical product. It freezes at 2 - 4 °C and has a boiling point of 90.3°C. Dimethyl carbonate is classed as a volatile flammable liquid, which does not have irritating or mutagenic effects if inhaled or in contact [212].

## **3.2 Solution preparation**

### **3.2.1 Silk Fibroin Solution preparation**

100g of de-gummed bombyx silk produced from silk worms of the Bombyx Mori moth was purchased from World of Wool, Huddersfield, UK. 15g of de-gummed silk was used to prepare 60ml of silk solution. Formic acid reagent  $\geq 96.0\%$  and lithium bromide  $\geq 99\%$  were obtained from Sigma-Aldrich (Dorset, UK) weighed amount (15g) of de-gummed silk fibroin was dissolved in 9.3M concentration of lithium bromide solution at 70 to 80° C. The silk solutions were then poured into 30mL slide-A-Lyzer Dialysis Cassettes (Thermo Fisher Scientific, USA) with a molecular weight cut off 3.5kDa and dialysed against deionised water for two days to remove the lithium bromide salts in the silk solution. The dialysed silk fibroin solution had a concentration of 8wt%. The solutions were then cast onto petri dishes and heat dried in an oven at 60°C until thin , transparent silk fibroin films were produced. The heat dried silk fibroin films were then cut up and weighed before being dissolved in formic acid to produce four different concentrations (10wt%, 15wt%, 20wt%, 22wt %) for printing.

### **3.2.2 Polycaprolactone Solution Preparation**

PCL (molecular weight 80 kDa) and dimethyl carbonate (DMC) were both purchased from Sigma-Aldrich. PCL pellets were dissolved in DMC to makeup solutions with eight different concentrations of polymer 7%, 10%, 12%, 15%, 18%, and 23% (by weight). This was done to identify the best range of concentrations for dispensing and ease of solvent evaporation that would result in a solid structure. PCL pellets and DMC were placed in a glass bottle

along with a magnetic stirrer and the solutions were magnetically stirred at ambient temperature of (25°C) for three hours, which was needed for complete dissolution.

### **3.3 Equipment**

#### **3.3.1 The Electrohydrodynamic printer**

A purpose built electrohydrodynamic printer [221] (Figure 11) was used. The x and y axis are driven by servo motors while the z axis is controlled by a stepper motor. When the axes are reset back to their home-positions both the print head and lower electrode are in line with each other (Figure 11c). A printing stage made of perspex was used to hold the substrate onto which the patterns are printed. 1  $\mu\text{m}$  linear encoders and endstop sensors on all three axes feedback information to the program COM-pu CAM to control the precise motion of the printing stage.

The 2D print pattern used was written up by specifying the x and y coordinates of the print route using Motion Planner software. The pattern produced in this study consists of a series of parallel linear lines separated by 250 $\mu\text{m}$  spacing. The program was uploaded to programmable motion-controller-PC unit. The print speed was set and maintained at 10mm/s for all the prints produced. A harvard syringe perfusor pump was used to deliver the silk solutions to the print heads via silicone tubing 300 $\mu\text{m}$  diameter. The needles were connected and regulated via a high voltage supply (Glassman Europe Ltd, Tadley, UK). The patterns were printed on VWR microscope glass slide at the ambient conditions specified earlier.

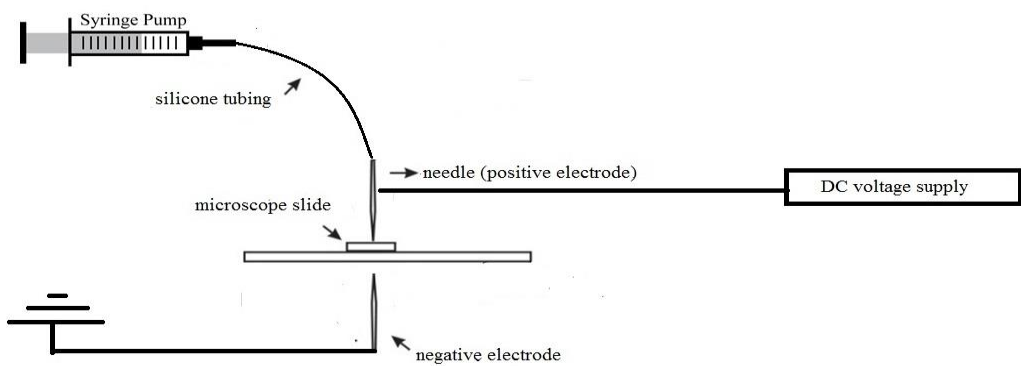


Figure 10 : Schematic diagram illustrating the printing setup used to test the print heads

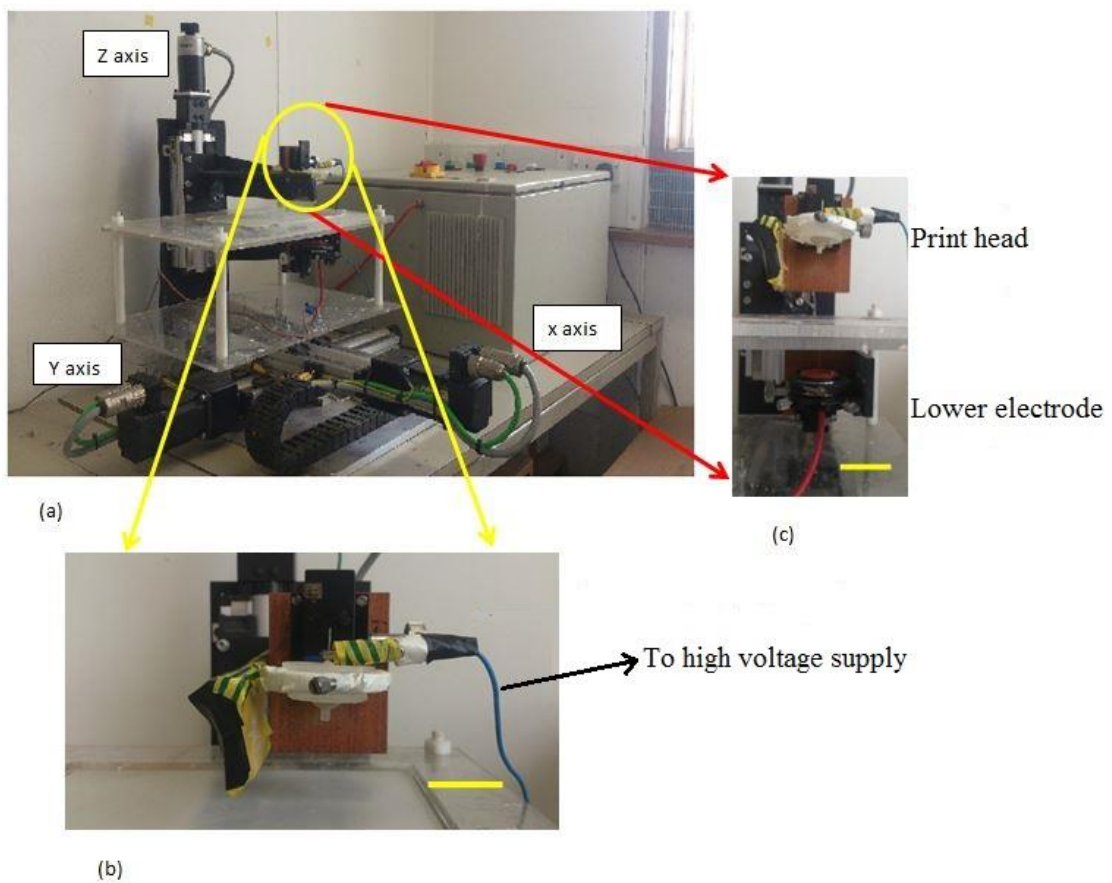


Figure 11: The electrohydrodynamic printer that was used to test the print heads: (a) the x, y and z axis printing stage which can move independently of the print head; (b) the print head assembly( scale bar 100mm) (c) the positions of the print head relative to the lower electrode (scale bar 100mm).

### 3.3.2 The print heads

The dimensions of the needles of the print heads are summarised in Table 2. More succinct details of the needles are described below.

#### 3.3.2.1 Reservoir

Consists of an 800 $\mu$ m shafted needle embedded within a plastic shell with a conical tapering end (Figure 12). The needle feeds the silk fibroin solution into the conical end of the plastic shell and also generates the electrical field when connected to the high voltage supply. The needle hovers over a small reservoir of silk fibroin solution that is maintained at a constant level by virtue of a regular flow rate.

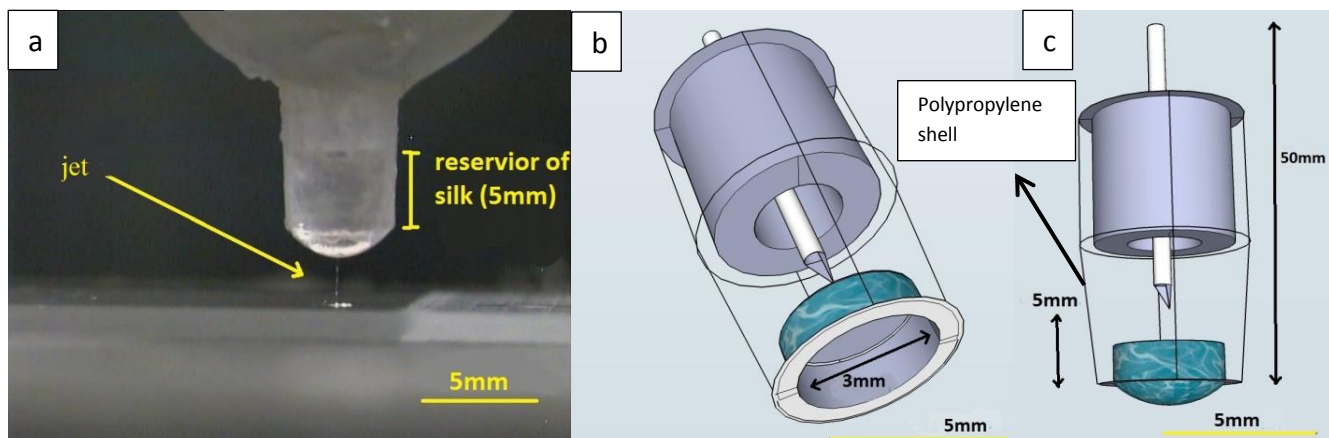


Figure 12: Reservoir print head: (a) in action, (b, c) internal view of design features

### 3.3.2.2 Pinhole reservoir

This print head (Figure 13) is built to the same specifications as the reservoir needle but the difference lies in the size of the orifice. In the Reservoir needle the orifice has a diameter of ~ 2mm while it is much smaller in the pinhole reservoir.

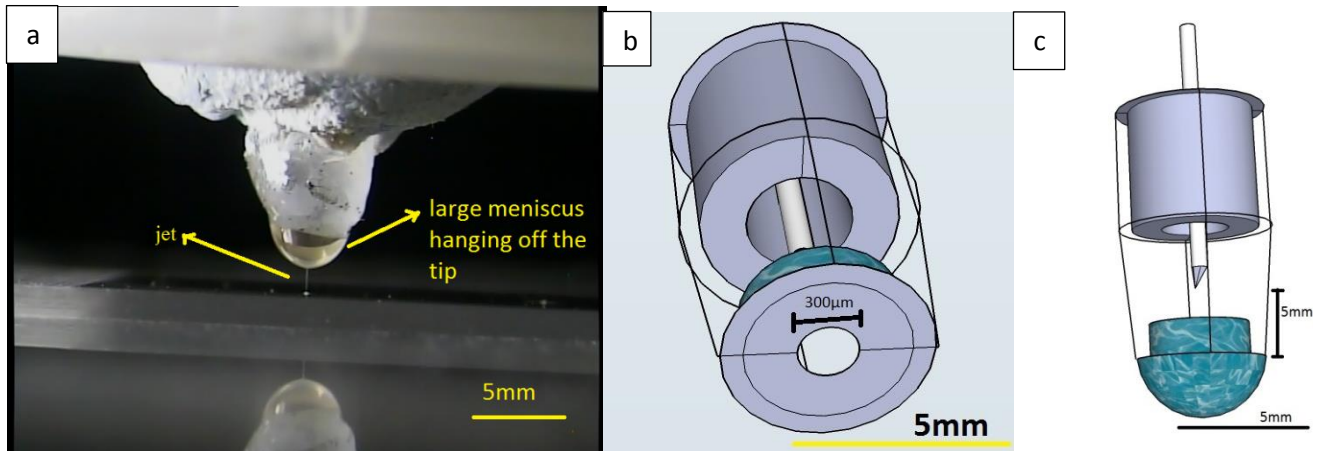


Figure 13: Pinhole reservoir print head: (a) in action (b, c) internal view of design features

### 3.3.2.3 Insulated shafted

This design (Figure 14) consists of a 800 $\mu\text{m}$  shafted needle partially insulated with silicone tubing. The sharpest point on the needle is positioned 780 $\mu\text{m}$  from the rim of the silicon tubing.

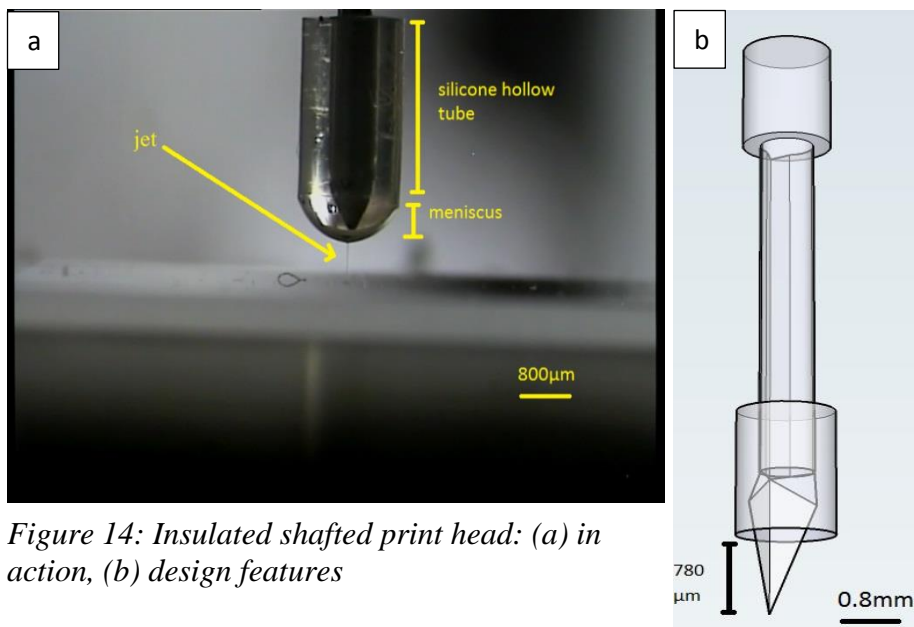


Figure 14: Insulated shafted print head: (a) in action, (b) design features

### 3.3.2.4 Shafted needle

In this design (Figure 15), the needle is positioned at 45° to the horizontal printing surface.

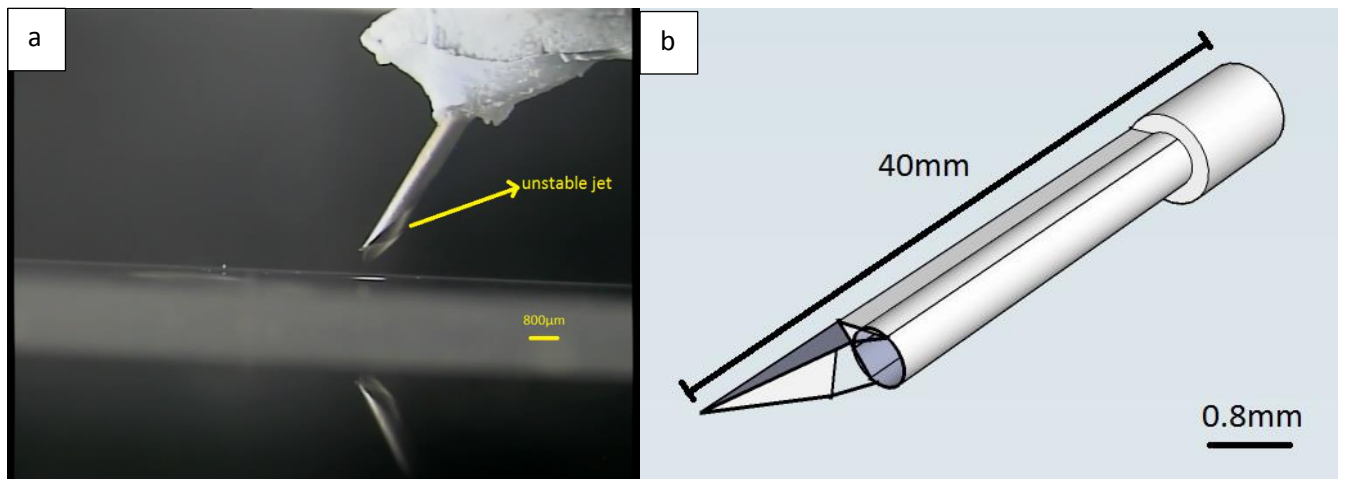


Figure 15: shafted print head: (a) in action, (b) design features

### 3.3.2.5 Calligraphy needle

In this design (Figure 16) a broad tip calligraphy nib with a slit down the middle is positioned at 45° to the horizontal and an 800μm shafted needle is used to feed the solution along the slit to the tip of the nib.

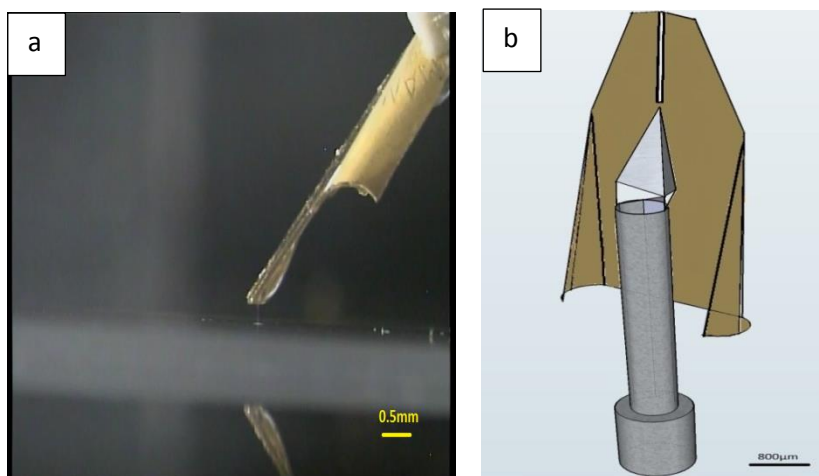


Figure 16: Calligraphy print head: (a) in action, (b) design features

*Table 2: Orifice dimensions of needles in each print head. In each case the needle supplying solution and generating the electric field was a shafted needle with an 800 $\mu$ m internal diameter.*

<b>Print head design</b>	<b>Orifice</b>
Reservoir	3mm
Pinhole	40 $\mu$ m
Insulated shafted	800 $\mu$ m
shafted	800 $\mu$ m
Calligraphy	800 $\mu$ m needle leading to an open ended broad tip calligraphy nib

### **3.4 Characterisation of solutions**

The solutions were characterized for their density, surface tension, viscosity, electrical conductivity and pH at a temperature of 21-25°C, ambient pressure (101.3 kPa) and a relative humidity of 50-55%.

#### **3.4.1 Electrical conductivity**

The electrical conductivity of the solutions was determined using a Jenway 3540 pH/conductivity meter (Bibby Scientific Limited, Staffordshire, UK). All the instruments were calibrated before use according to the manufacturer's instructions. The conductivity electrodes were always cleaned with acetone or ethanol to remove any excess polymer solutions or liquids remained into the probes. The probe was also rinsed with distilled water, after cleaning with ethanol or acetone, and dried before measurements. The electrode was kept immersed in the solutions/liquids for 10 min and the electrical conductivity values

shown on the meter were recorded. The mean values of three consecutive readings for conductivity were taken.

### **3.4.2 Surface Tension**

Using a Kruss Tensiometer K9, the surface tension of the solutions (standard Wilhelmy's plate method) was measured. Each solution was added to a 20ml tall glass container (beaker) and it was placed at the tensiometer platform. Then, the rectangular shape plate was hung from the tensiometer hook and the tensiometer was calibrated before use (set to zero). The edge of the plate was moved at the surface of the liquid in such a way that a meniscus could be formed between the liquid and the plate due to the surface tension force of the liquid. The plate was then steadily lifted and the surface tension value was taken when the plate was just about to detach from the liquid surface. The process was repeated five times for each liquid/solution in order to minimize errors and the average value and standard deviation of the surface tension was calculated. The plate was thoroughly cleaned after every measurement.

### **3.4.3 Density**

The density of the liquids/solutions used in the experiments was measured using a 25 ml standard density bottle (VWR International, Lutterworth, UK). An electronic balance (AND HF-1200G A&D Instruments Ltd., Japan) was used to measure the mass of the empty density bottle and the mass of the bottle filled with liquid/solution. The density value of each

liquid/solution was measured five times and the mean value and standard deviation were calculated. The density  $\rho$  ( $\text{kg m}^{-3}$ ) was obtained each time by the following Equation:

$$\rho = \frac{(W_2 - W_1)}{25}$$

Where  $W_1$  (g) and  $W_2$  (g) is the mass of the empty bottle and the mass of the bottle filled with liquid/solution, respectively.

### **3.4.4 Viscosity**

A Brookfield DV-III Ultra Rheometer suitable for small volumes, with an SC4-18 spindle, (Brookfield Viscometers Ltd, Essex, UK) was used to measure the viscosity of highly viscous

## **3.5 Characterisation of printed products**

### **3.5.1 Optical Microscopy**

The printed scaffolds were studied by optical microscopy (Micropublisher 3.3 RTV, 3.3 megapixel CCD Color-Bayer Mosaic, Real Time Viewing camera, MediaCybernetics, Marlow, UK). MediaCybernetics Image-Pro Insight software and Image J was used to carry out sample analysis. Images of the printed patterns were studied using a Nikon Eclipse ME600 optical microscope (Nikon Company, Tokyo, Japan). A set of 10 line width measurements were made for each pattern and the corresponding averages and standard deviations were calculated.

### **3.5.2 Differential scanning calorimetry**

Thermograms were recorded on a Perkin Elmer PYRIS Diamond Differential Scanning Calorimeter working in a nitrogen environment (20 $\mu$ l/min flow). Sealed aluminium pans containing approximately 5mg of the sample were used in each case. Thermograms heat/cool/heat were recorded in the range 20-70°C with a heating and cooling rate of 10°C/min. Two heating/cooling cycles were carried out to firstly determine prior thermal history of the PCL samples and secondly to determine behaviour once a uniform heating/cooling profile was administered.

The heat of fusion was used to compute the percentage crystallinity,  $XC = \Delta H_m / \Delta H_m^\circ$  , where  $\Delta H_m$  was the measured enthalpy of melting and  $\Delta H_m^\circ$  was the enthalpy of melting of 100% crystalline polymer. For PCL  $\Delta H_m^\circ = 142$  J/g.

### **3.5.3 Fourier transform infrared raman spectroscopy**

The FTIR spectroscopy was used to confirm the presence of different functional groups of Dimethyl carbonate in the scaffolds that were produced. FTIR-ATR spectra were determined using a Perkin Elmer system 2000 FT-IR spectrometer equipped with a diamond ATR accessory. Ten scans over the region 3000cm<sup>-1</sup> – 400cm<sup>-1</sup> were made at a resolution of 4cm<sup>-1</sup>

### 3.5.4 AFM peak force quantitative nanomechanical mapping

The mechanical properties of the scaffolds were studied at the nanoscale using PeakForce QNM AFM. The technique allows the user to gauge the force and distance at nanometer scale resolutions in numerous environmental conditions. The surface topography of hydrogels, cells and other biomaterials typically used in tissue engineering can be mapped out effectively. Through nanoscale probing, the technique provides information on the Derjaguin-Muller-Toporov (DMT) modulus, deformation, adhesion and dissipation. The DMT model was applied in this study to quantitatively map the Young's modulus information. AFM PeakForce QNM was carried out with a Bruker MultiMode 8 AFM microscope that was fitted with a PPP-NCH cantilever (Nanosensors). For quantitative analysis, a sampling area (4x4 $\mu$ m) consisting of a matrix of pixels measuring 256x256 was chosen at an appropriate point on the flattest part of the sample. The calibration of the cantilever was carried out using the relative method by comparison to a known reference sample. Further analysis of the raw data was conducted by using the NanoScope analysis (V1.40) software package.

The data were analysed by a modification of the Hertz theory which makes assumption that the sample is an isotropic and linear elastic solid occupying an infinitely extending half space and that the indenter is not deformable. Loading force is defined as:

$$F = \frac{4\sqrt{R}}{3} \frac{E}{1 - \nu^2} \delta^{\frac{3}{2}}$$

Where  $\delta$  = indentation depth,  $v$  = Poisson's ratio,  $R$  = tip radius and  $E$  = elastic ratio

The DMT model adds a correction for adhesive forces to the Hertz model and this gives:

$$F - F_{adh} = \frac{4}{3} E^* \sqrt{R(d - d_0)^3}$$

$F - F_{adh}$  is the force on the cantilever relative to adhesion force,  $d-d_0$  = deformation of the sample and  $E^*$  is the reduced modulus. If the Poisson's ratio is known:

$$E^* = \left[ \frac{1 - v_s^2}{E_s} + \frac{1 - v_{tip}^2}{E_{tip}} \right]^{-1}$$

$v_s$  = Poisson's ratio of the sample,  $v_{tip}$  is Poisson's ratio of the probe,  $E_s$  is the Young's modulus of the sample,  $E_{tip}$  is the Young's modulus of the probe.

## CHAPTER 4

### DESIGN AND CONSTRUCTION OF THE ELECTROHYDRODYNAMIC CARTESIAN ROBOT

#### 4.1 Overview

In recent times 3D additive manufacturing has appeared on the global stage as a major disruptive technology. The technology embodies itself in many competing ways, namely SLS (selective laser sintering) [213], FDM (fused deposition modelling) [213, 214], 3DP (three-dimensional printing) [213-215], LOM (laminated object manufacturing) and finally, stereolithography apparatus (SLA) [214]. Despite these processes having the ability to produce 3D structures, they lack consistency and accurate reproducibility. Techniques like LOM and SLA require additional preparation steps before the product is finished. These additional steps increase the complexity and the cost of fabrication. The ease of use and cost had always been major drawbacks that have in the past isolated 3D printing technology only to a niche market. However, reduction in cost of hardware and innovative programming has led to accessible open source projects like RepRap which has marked a peak in the steady maturity of this technology over the last three decades [216].

At present RepRap which is an FDM technology has been portrayed only as a novelty device with extensive and versatile printing capabilities at very coarse layer thicknesses. Unfortunately, in-situ material manipulation for printing is only limited to thermoplastics that can be heated just beyond their melting temperature before being extruded onto a heated bed. Metals and heat sensitive organic compounds are yet to be printed via FDM (fused deposition modelling) [217]. Moreover printing onto surfaces is restricted to the heated bed that is

supplied with the printer. Nevertheless, attempts have been made to use the technology to build specialised 3D printers that can be used to extrude cell solutions and hydrogels accurately to manufacture scaffolds for organ regeneration with varying degrees of success. The technology allows for spatially heterogeneous multi-material structures to be produced resulting in cell laden scaffolds for applications in replacement knee menisci and invertebral discs [218-220].

Issues with the previous printer that were taken into consideration:

The printer described in chapter 3 struggled with a number of issues that paved the way for work on the cartesian robot. Some of the main issues are described below

### 1) Hardware resolution

The printer was restricted to a maximum hardware resolution of  $24\mu\text{m}$ .

### 2) Vibrations

The printer was unable to make sharp turns without violent tremors distorting the printed lines (Figure 17).

### 3) Open system

The printer was exposed to the open environment and thus made the electrohydrodynamic jetting susceptible to changes in humidity, temperature and minor disturbances in the ambient surrounding.

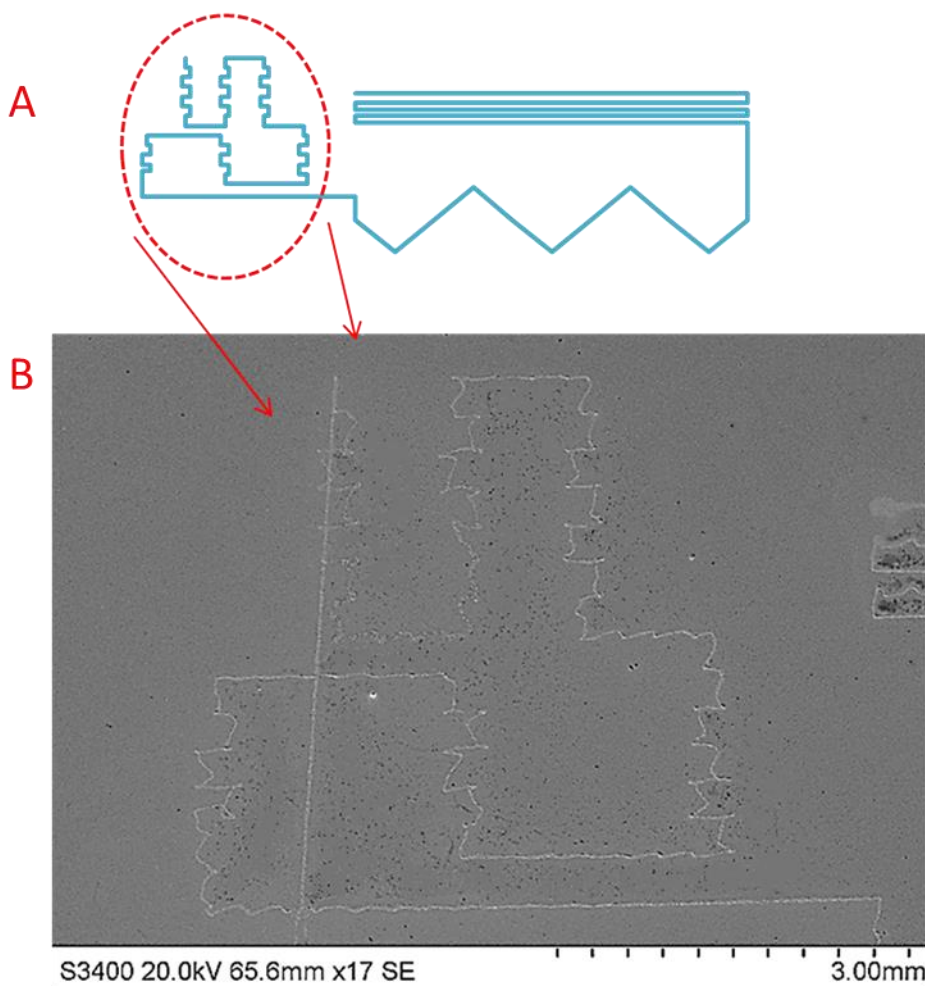


*Figure 17: Comparison of A) intended printing path and B) actual printed path taken due to the tremors at sharp corners*

#### 4) Metal Frame

Most of the printer was manufactured out of aluminium, more specifically the print head holder. This meant that every metal component in the vicinity of the print head would act as a potential ground when a voltage was applied to the print head. These electrical disturbances affected the stability of the cone-jet when printing and also posed a health and safety risk to the user.

## 5) Outdated Software

The Compu-Cam software that was used to operate the printer was tedious and cumbersome to use since the G-code had to be manually entered into the program and debugged before printing. This restricted the complexity of structures that we could potentially print.

## 6) No live feed

Since there is no camera to feed information back to the user, visual judgements can only be made with the naked eye which is prone to error and exposes the user to risk when operating with highly corrosive solvents.

## **4.2 The Setup**

The EHD 3D printer that was designed and constructed in our laboratory is a purpose-built cartesian robot, using the popular open-source Arduino microcontroller as its central feature together with stepper drivers, motors, and sensors to control its movements (Figure 18-20). To perform a print, a CAD (computer aided design) file that contains the model design is first converted into an STL (standard tessellation language) file. The STL files contain three-dimensional polygons that are sliced up into distinct layers using a slicing software so that the printer can easily digest its information. The program then divides the object into digital cross-sections so that the printer is able to build structures layer-by-layer. The cross-sections essentially act as guides for the printer, so that the object is the exact size and shape by specifying tool paths to dictate precise movements. This is then followed by conversion into machine understandable G-code that can be used to control the stepper motors which in turn determine accurate translations in the x, y or z direction.

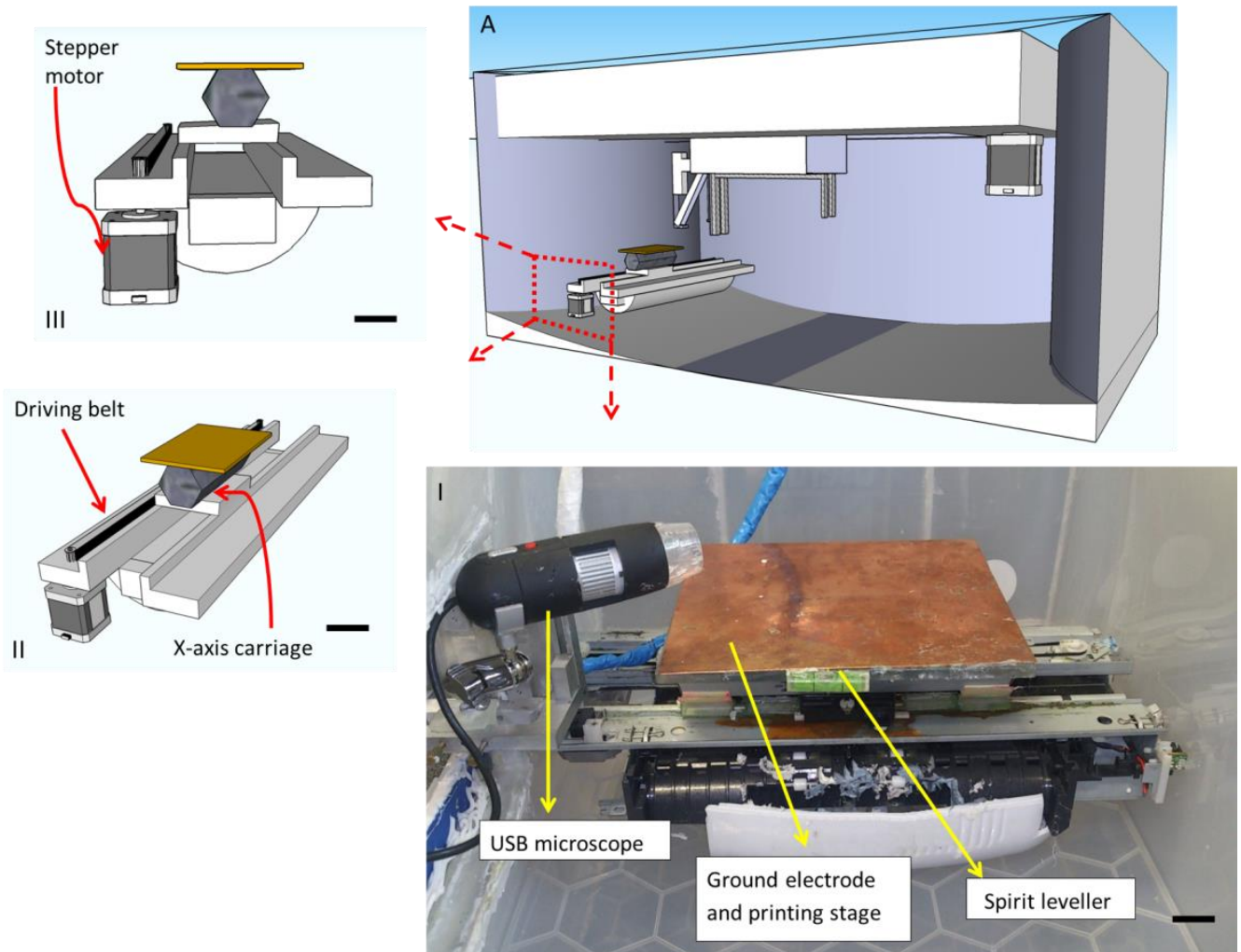
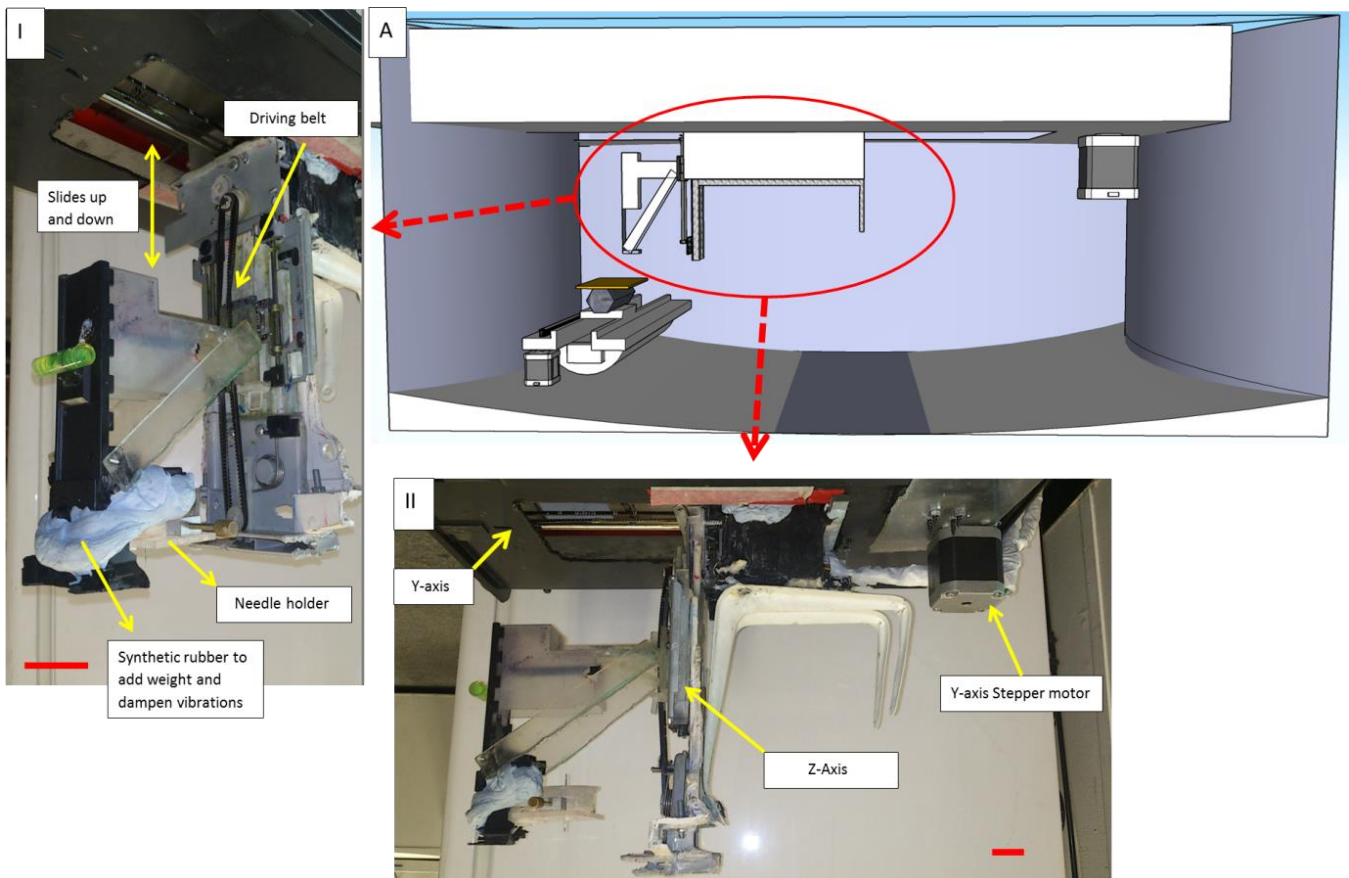
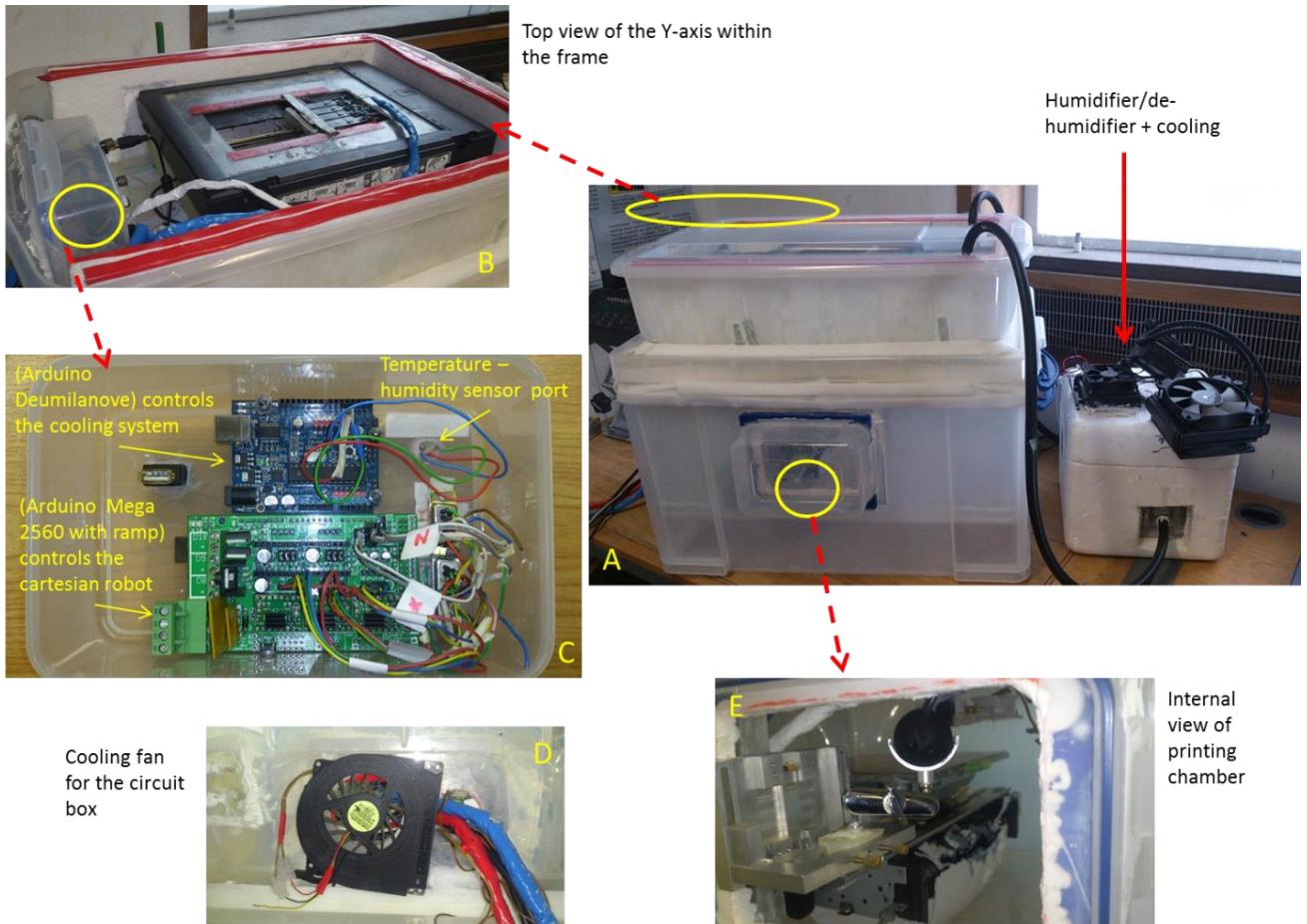


Figure 18: The x-axis. A) internal view of the printer A(I)The X-axis and the components with respect to each other A(II) isometric view of the x-axis showing the drive belt and x-axis carriage A(III) side-on view of the x-axis showing how the stepper motor fits into the x-axis. (Scale bar =100mm)



*Figure 19: Cross-sectional view of the printer revealing the Y and Z axis assembly within the printer. A(1) key components of Z- axis, gears, driving belt and needle holder A(II) side on view showing the positions of Y and Z axis in relation to each other. (Scale = 20mm)*



*Figure 20: The Cartesian robot. a) full setup b) y-axis cradle c) main circuit box d) cooling fan for the main circuit box e) Internal view, x and y axis positions can be seen in relation to each other*

A script based software determines the tool path from the STL file and sends the information to the Arduino 2560 mega microcontroller which in turn interfaces with the RepRap arduino mega pololu shield to drive the stepper motors which were preferred over servo motors due to the low operating accelerations and static loads that each axis was expected to endure during the course of each print. The stepper motors fit into an open loop control system where no real time feedback is provided with respect to the home positions of each axis. This apparent drawback is offset by a new feature called microstepping that facilitates each step taken by

the motor to be subdivided further into smaller micro steps thus enabling high precision and accuracy during motion. This microstepping feature which is provided by the A4988 pololu stepper drivers also serves to allow a stepping motor to stop and hold a position between the full or half-step positions. This feature also eliminates the jerky character of low speed stepping motor operation thus reducing vibrations and diminishing problems related to resonance.

When operating at low speeds there is always a risk of the stepper motor missing steps due to a fall in current followed by a sudden subsequent rise of current in the copper windings of the motor. An enhancement designed into the A4988 pololu stepper driver specifically addresses this issue by mixed decay operation which prevents rapid fluctuations in current to ensure smooth motion regardless of changes in speed during a print.

### **4.3 Machine frame and axes**

A sturdy polypropylene structure was used to bear the static and dynamic loads, thermal strains and mechanical vibrations. It is essential that the polypropylene structure does not deform or vibrate beyond the permissible limits under the action of forces encountered in printing. All components of the machine must remain in correct relative positions to maintain the geometric accuracy while printing, regardless of the magnitude and direction of these forces. Two polypropylene boxes were used to build the frame of the electrohydrodynamic cartesian robot. A closed chamber was preferred to ensure maximum isolation from the external environment.

The walls of the inner polypropylene box bend inwards to reduce the area of contact with the external box (Figure 21). This is done to minimise flow of heat and vibrational energy into and out of the printing environment. The configuration also forces the inner box into a state of compression thus making the frame sturdy with the external box forming the tough flexible exo-skeleton. Within this frame, three belt driven axes are placed orthogonally to each other with the Z axis hanging off the X-axis (Figure 19 A (II)). All three axes were fitted with mechanical endstops to feedback information to the computer on the limits of each axis.

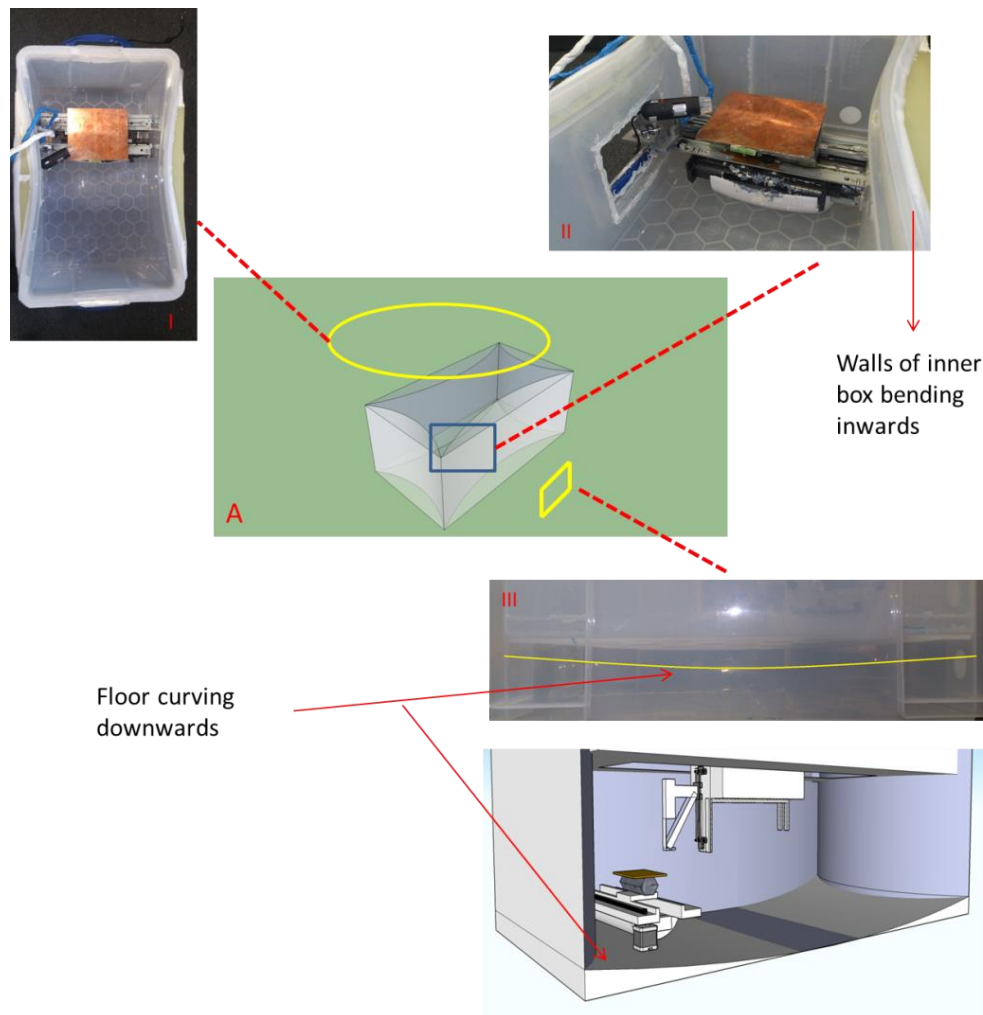


Figure 21: Polypropylene frame. 1) Top view showing contours of the internal box II) inward bending of wall III) floor bending downwards

During printing the Z-axis makes 100 $\mu\text{m}$  translations after every layer is deposited while the x-axis and y-axis are capable of delivering up to a minimum of 10 $\mu\text{m}$  translations at a time. This represents an overall increase in the printing hardware resolution when compared to work that was performed on a conventional CNC machine [221] where the hardware resolution was 24 $\mu\text{m}$ .

The printer also features a flat ground electrode made from copper (Figure 18 A (I)). This enables the electric field lines generated by the positively biased needle to meet the ground electrode perpendicularly. This is done to improve homogeneity of the electric field lines close to the surface which should serve to minimise whipping and axisymmetric instabilities in the jet during printing. A generic USB microscope is installed to provide live video feed during any print. The USB microscope is capable of recording in high definition at 30 frames per second and is important in allowing the user to make visual judgements on the stability of the jet thus permitting minor adjustments to be made to the flow rate or applied voltage.

## **The fluid deposition**

A Harvard syringe perfusor pump was used to deliver the PCL solutions to the print head through silicone tubing measuring 300 $\mu\text{m}$  in diameter. The needles were connected and regulated via a high voltage supply (Glassman Europe Ltd, Tadley, UK). The structures were printed into petri dishes filled with distilled water. To avoid charge build up, the petri dishes were grounded using an external ground electrode

#### **4.4 Cooling/humidity control system**

Since temperature and humidity play a vital role in achieving a stable cone-jet, it is necessary for the operating environment to remain at a specified temperature and humidity depending on the type of polymer that is used in the print. An automated cooling system was built to maintain a constant temperature and humidity for the duration of the print which usually lasts for about 190 minutes.

The mechanics of automated cooling control requires a simple feedback loop to be in place to ensure efficient regulation. In this feedback loop, a DHT11 temperature-humidity sensor is placed close to the printing area. The sensor reads the current temperature and humidity of the chamber and feeds the information back into a program written in C language which is installed and running on the microcontroller. The readings are then matched to a predefined setting which is specified by the user and subsequent humidity levels and cooling are regulated via the engagement of the peltier cooling element, humidifier/de-humidifier as and when required. This is made possible through a series of connections between the respective devices and the power supply through a relay module that is in turn controlled by the microcontroller (Figure 22). The relay module acts as switch, switching on and switching off any of the devices wired up to it based on instruction from the microcontroller.

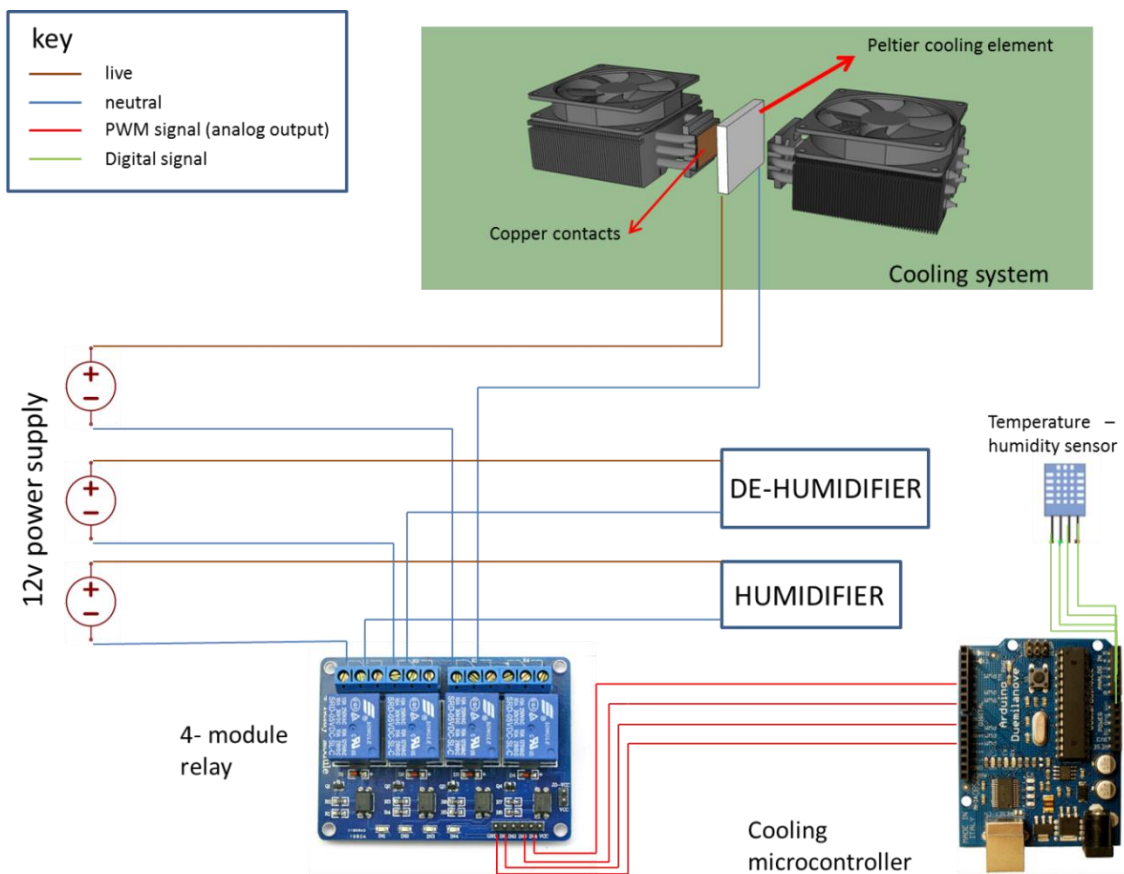


Figure 22: Circuit diagram illustrating the connections between the microcontroller, humidifier, de-humidifier and the cooling mechanism.

The cooling system consists of a peltier cooling element sandwiched in between two water liquid coolers (Figure 23 (I)). The peltier element uses the peltier effect to generate a heat flux at the juncture between the two sides of the element which is made of two different types of materials. This peltier effect results in a temperature differential of about 60°C between the two surfaces of the element (Figure 23 (I)). As a direct result of this the peltier element can act as a solid state thermoelectric heat pump that is capable of moving heat energy out of the printing chamber. The cool side of the peltier element is placed in contact with the copper contacts of the water cooler across which water (the coolant) is pumped before being channelled back to the radiator where the air from the printing chamber is cooled by making

it to pass across chilled aluminum fins before being directed back into the main chamber (Figure 23 (I)).

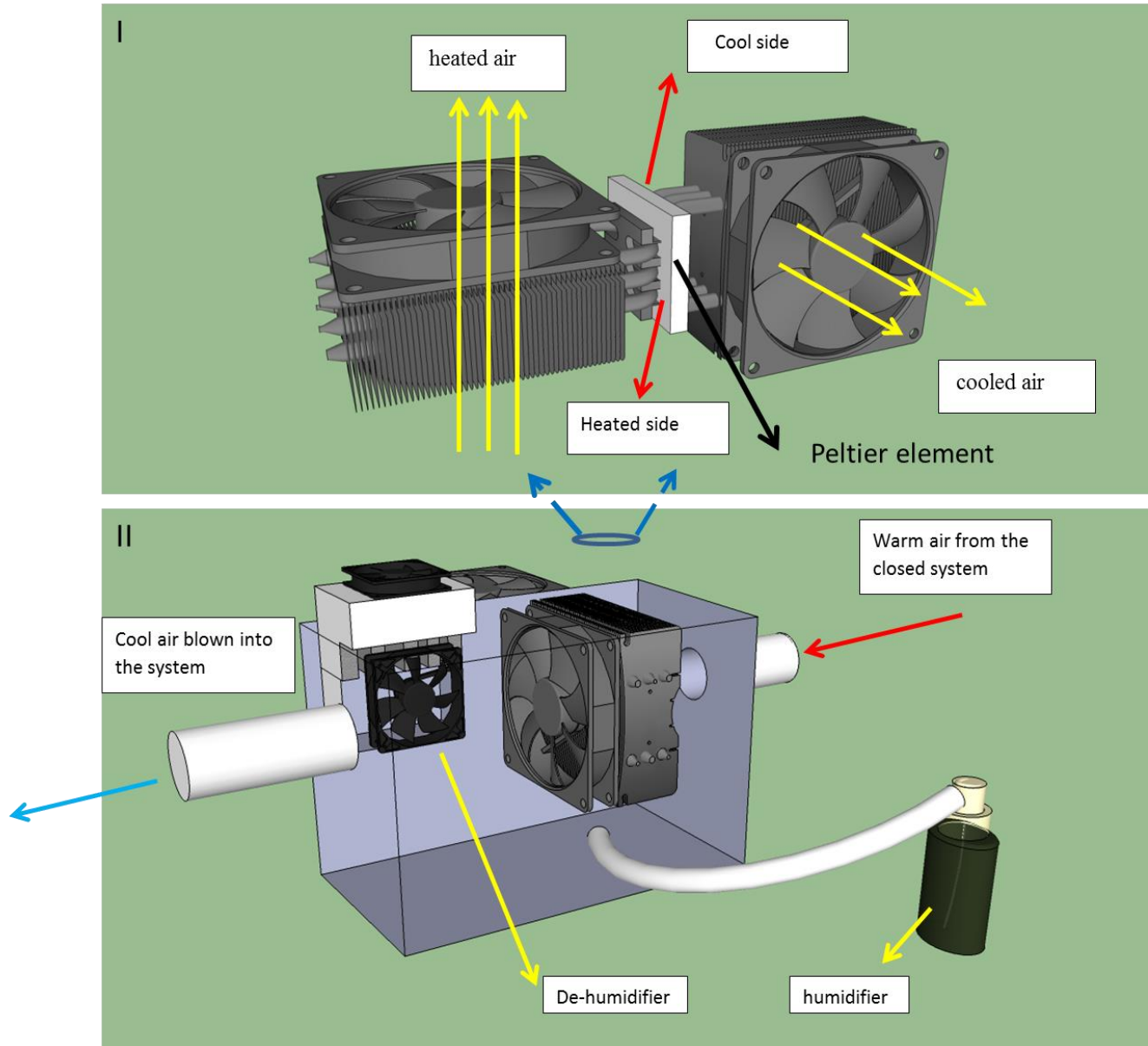


Figure 23: The cooling/humidity control system. I) how the cooling mechanism works II) cross-sectional view illustrates the different components of the cooling/humidity control system.

## CHAPTER 5. RESULTS AND DISCUSSION

### 5.1 Evaluation of the Print Heads

#### 5.1.1 Reservoir, insulated shafted and pinhole print heads

The best printed lines generated by each print head are compared in Figure 24. Figures 25 (a)-(e) provide a detail assessment of the printed line width generated by each needle with respect to the applied voltage. A gradual increase in the line width was observed as the voltage applied was increased from 10 to 20 kV for all silk concentrations and flow rates. As the voltage increases there is an increase in the applied electrostatic stresses that results in more material being pulled out. At low voltages (10kV, 12kV) small amounts of solution is pinched-off from the large meniscus that is suspended from the tips of all the print head designs. Each print head design responded well to change in low flow rates and was able to print its highest resolved lines at  $1.5 \mu\text{L}/\text{min}$  with the exception of the calligraphy needle. No obvious pattern was noted as the concentration of the solutions was varied from 10wt% to 22wt% but it produced different results for each print head design.

Short electrode separation distances of 5mm were used and the effect of four different concentrations on each needle and the resulting line widths were studied. As a result of varying the concentrations in each solution the electrical conductivity and viscosity was also different for each solution (Table 3). The higher viscosity solutions produce the most stable jets but tend to thicken the jets produced. Solutions with a higher viscosity have a higher conductivity but the effect is diminished due to reduced charge mobility.

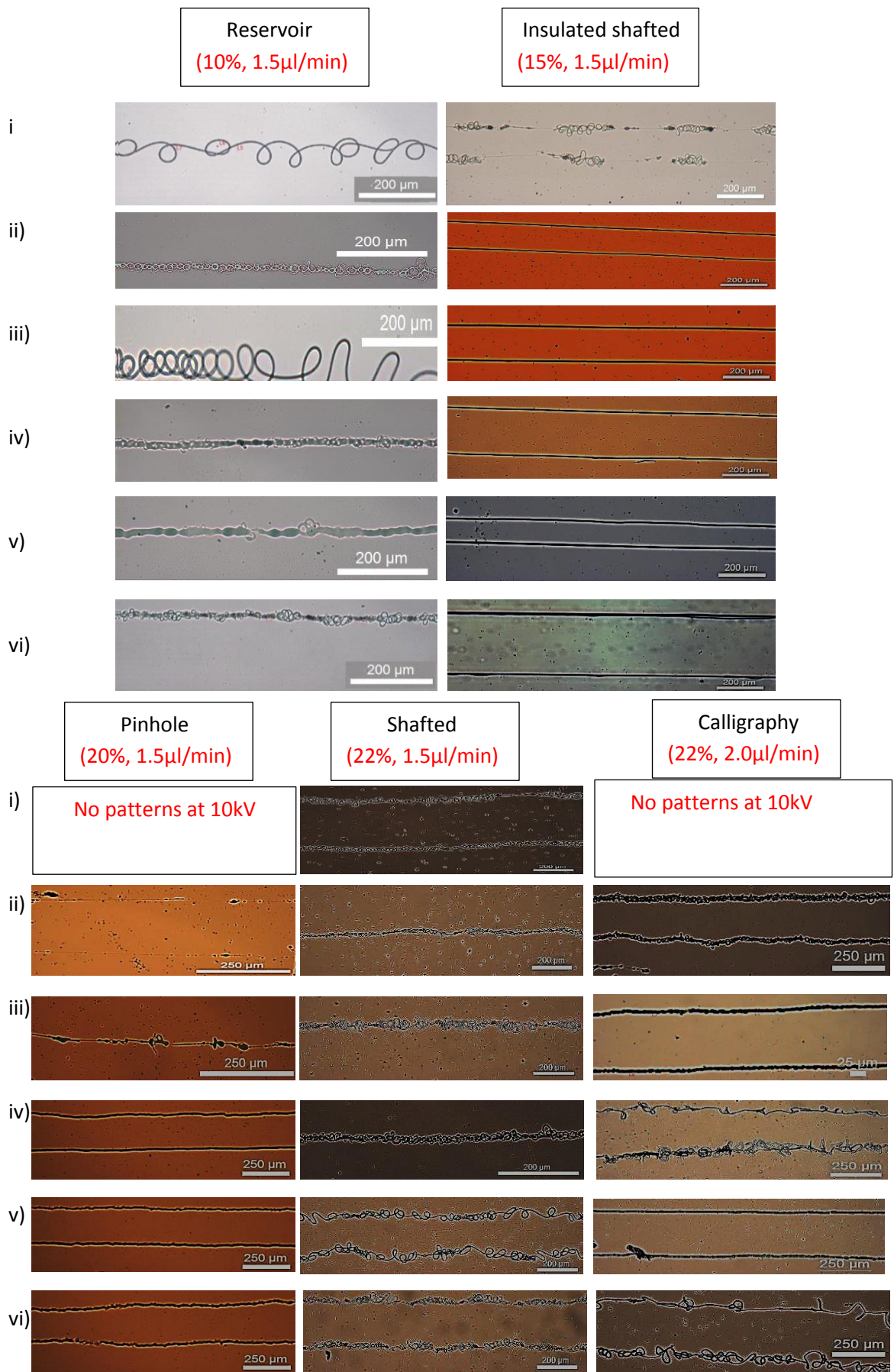
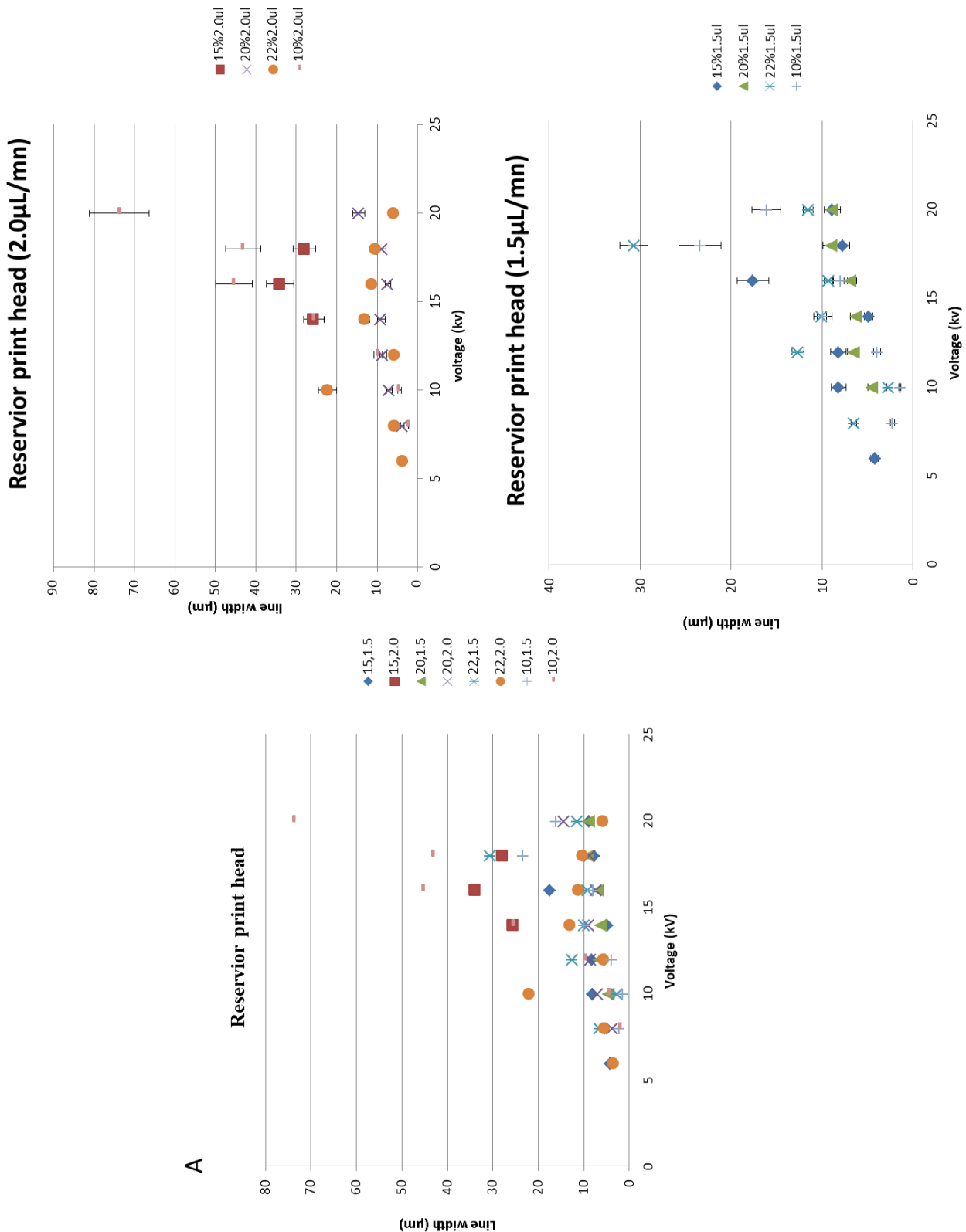


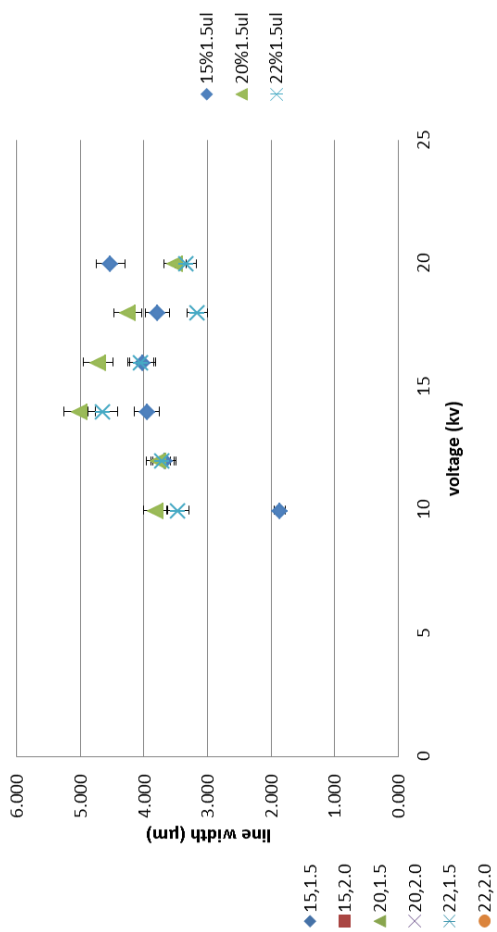
Figure 24: A comparison of best print patterns produced by each print head as the applied voltage is increased from i) 10kV to vi) 20kV in increments of 2kV.



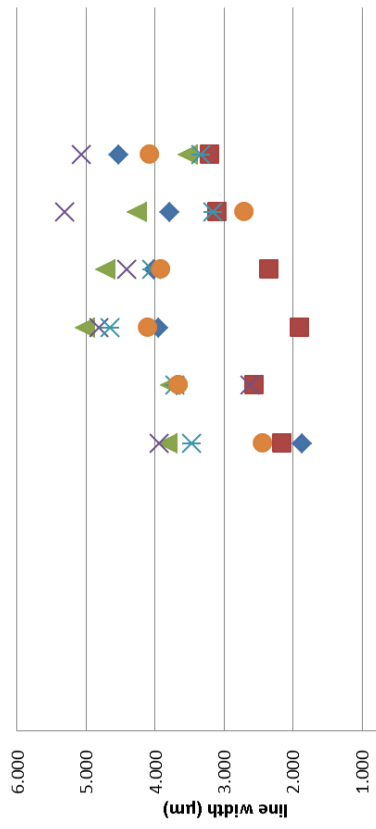
When determining the average line width for excessively coiled and wavy printed lines, care was taken to make sure only linear sections of the printed lines were selected. A series of ten random measurements were taken along the length of the printed line.

B

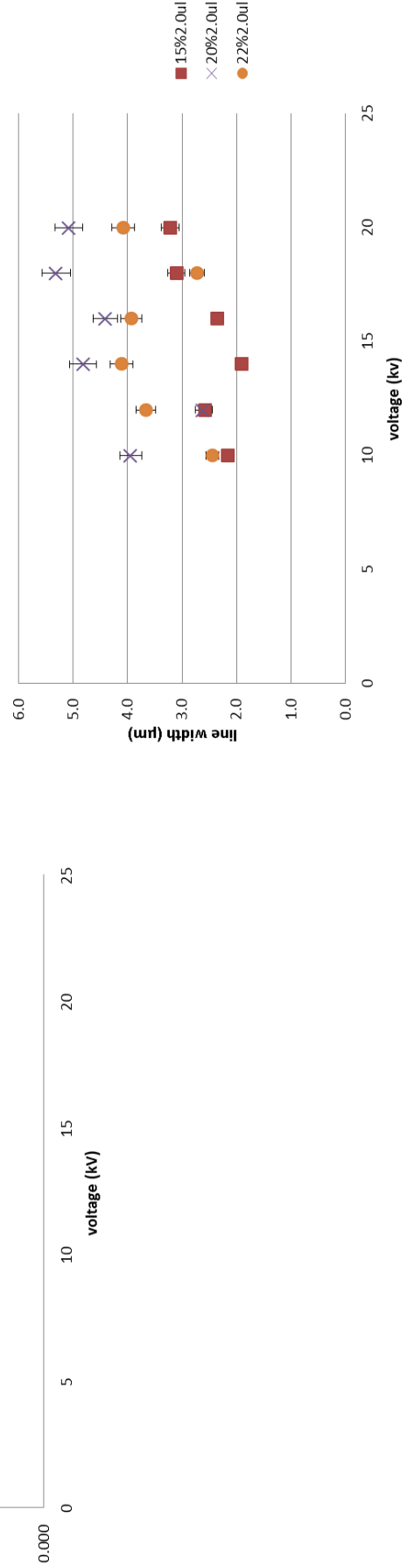
### Insulated shafted print head (1.5 $\mu$ L/mn)



### Insulated shafted print head

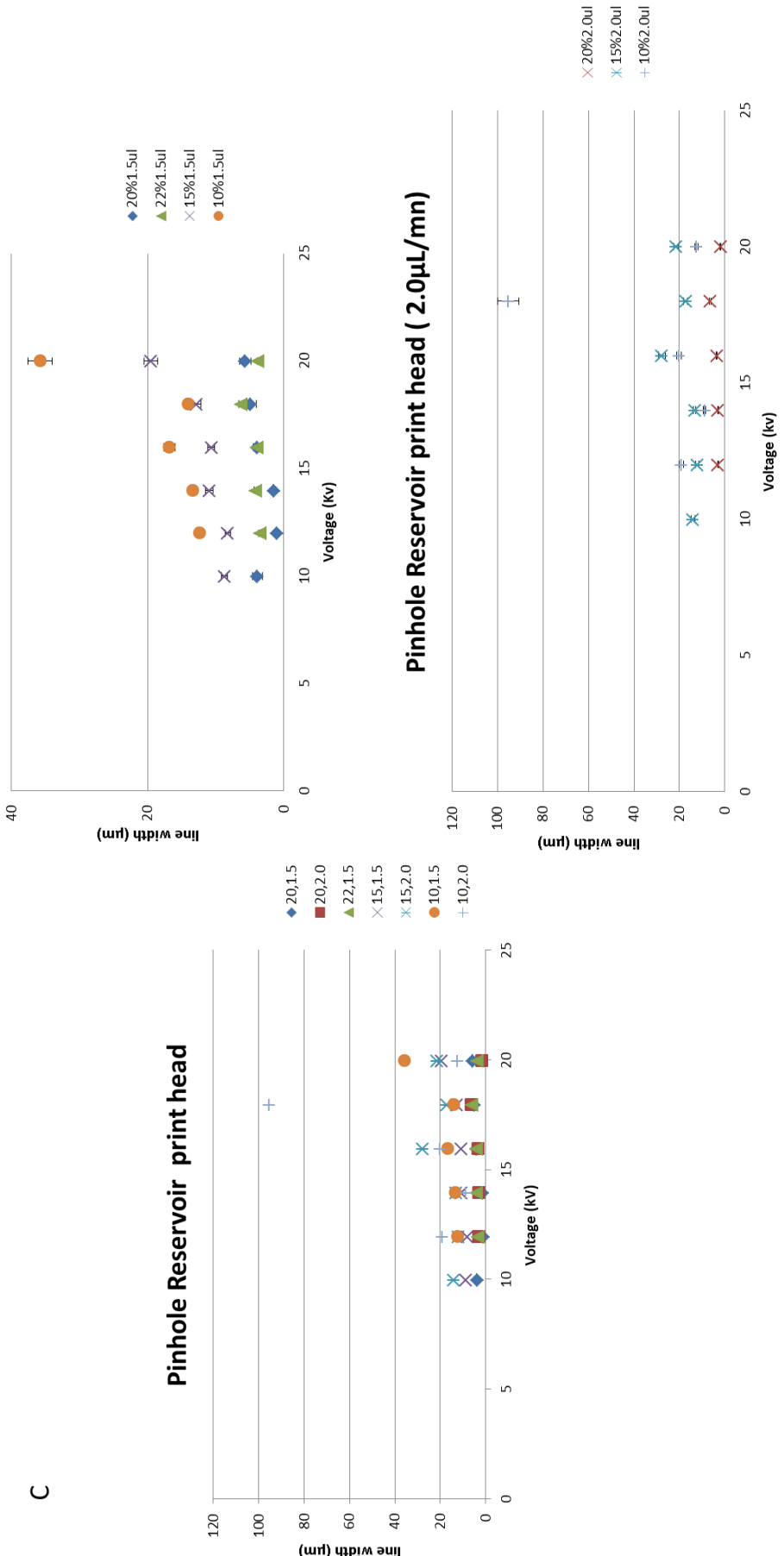


### Insulated shafted print head (2.0 $\mu$ L/mn)



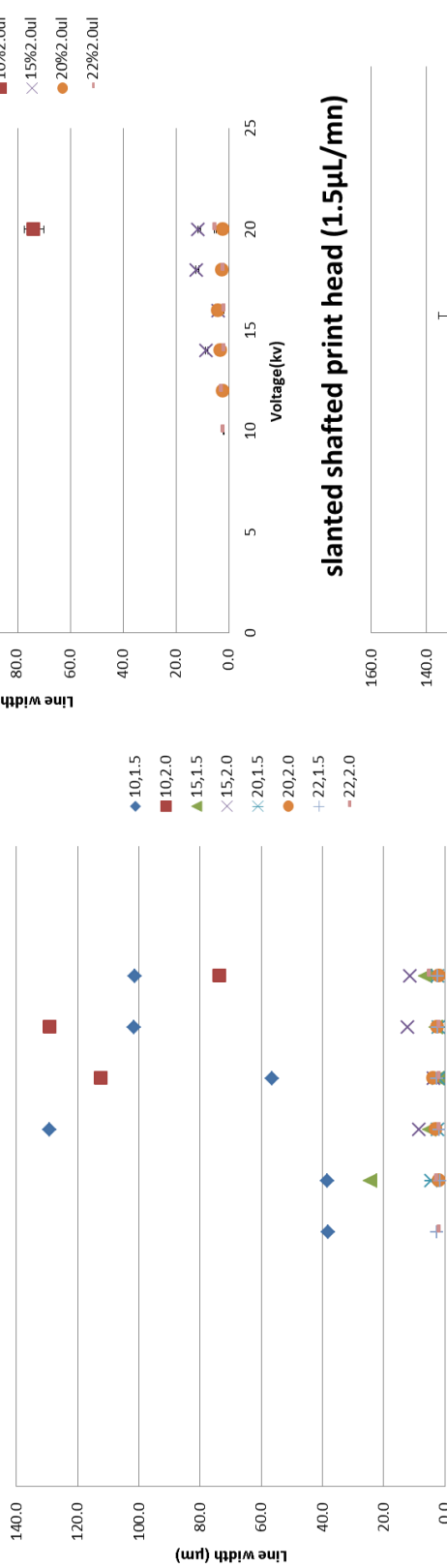
C

### Pinhole Reservoir print head ( 1.5 $\mu$ L/mn)

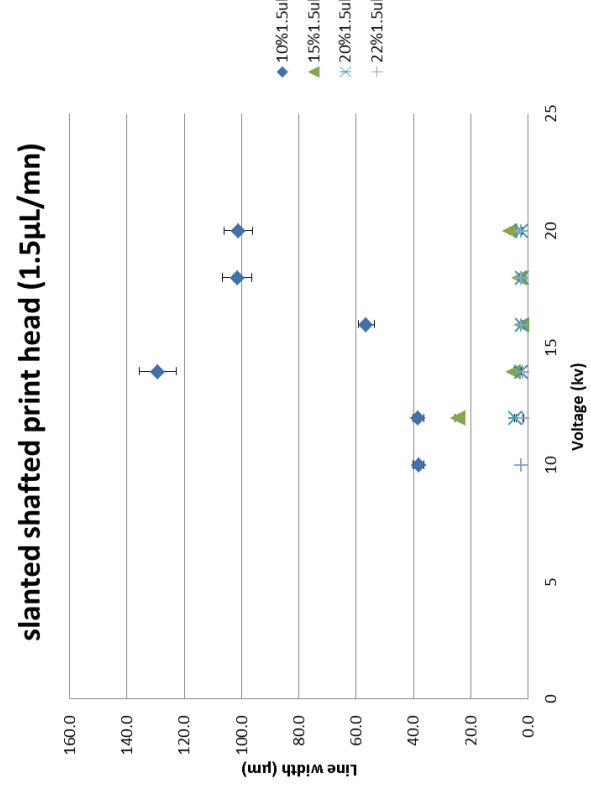


D

### slanted shafted print head



### slanted shafted print head (2.0 $\mu\text{L}/\text{mn}$ )



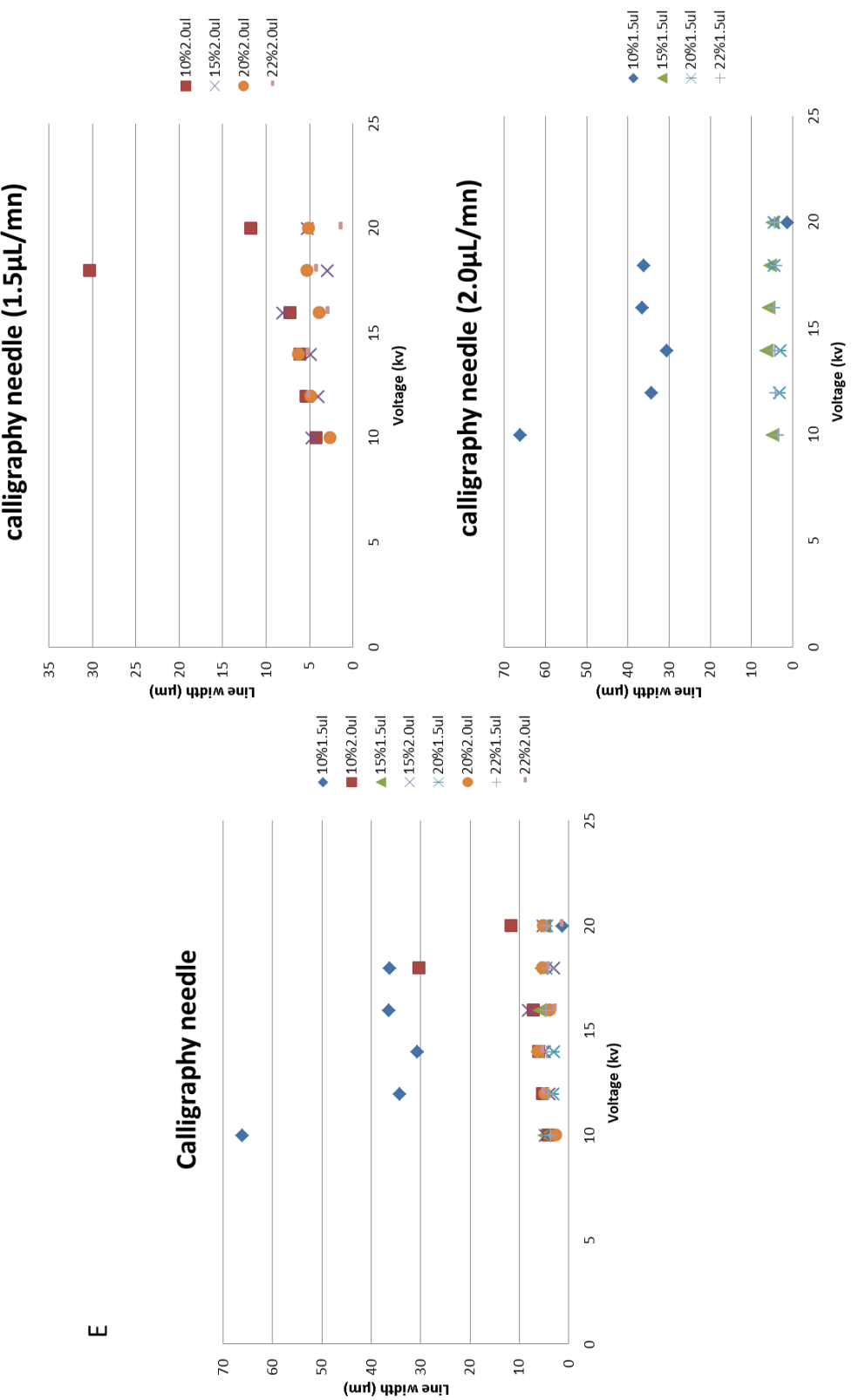


Figure 25: Printed line width variation with applied voltage and silk concentration for both flow rates ( $1.5\mu\text{L}/\text{min}$  and  $2.0\mu\text{L}/\text{min}$ ). a) Reservoir print head b) Insulated shafted print head c) Pinhole reservoir print head d) Slanted shafted print head e) Calligraphy print head. The key in each graph indicates: Silk concentration in wt%, Flow Rate in  $\mu\text{L}/\text{min}$ .

### 5.1.2 Silk fibroin solution properties

Table 3: Physical properties of silk fibroin solutions used in the experiments. All % refer to weight

Solution	Density(kgm <sup>-3</sup> )	Viscosity (mPa s)	Electrical conductivity (mS m <sup>-1</sup> )	Surface tension (mNm <sup>-1</sup> )
Formic acid	1220	1.44 ±0.2	30 ±2	35 ±0.3
SF 10%	1310	10 ±0.2	598 ±5	40 ±0.6
SF 15%	1330	18.6 ±0.2	745 ±3	42 ±0.2
SF 20%	1320	29.5 ±0.1	859 ±6	44 ±0.8
SF 22%	1340	39.2 ±0.2	916 ±2	45 ±0.7

The low working distance helps reduce the chances of varicose and whipping instabilities from arising in the jet as well as in maintaining the rheological properties of the solution by limiting solvent evaporation (222). The concentrated electrical field that is created over a short working distance of 5mm brings about the enhanced ionization of the gas around the tip of the needle and the ionization produces electrons that partially neutralize the charges on the surface of the jet, hence restricting the growth of whipping disturbances (32) . As a result, any irregularities observed on the optical micrographs of the printed patterns can be attributed to instabilities brought about by buckling. Controlling mechanical buckling instabilities triggered by competing axial compression and lateral bending of the electrified jet proved to be very difficult. These instabilities arise as a result of compressive and bending forces being exerted onto a straight electrified jet as it makes contact with the firm glass substrate thus forcing the jet to bend and curve during deposition (223).

Each print head was structurally designed to investigate different aspects for potential in control, printed line width and jet stability. The differences in designs forced mechanical buckling under a variety of conditions and as a result for the same set of parametric

conditions different buckling patterns were produced when each of the five print head designs were used.

The excessive coiling and looping that is observed in patterns printed using the reservoir print head (Figure 12) can be attributed to buckling instabilities (223). This effect is most pronounced at low voltages of (10kV) and the frequency with which the looping occurs increases as the voltage is gradually increased to 20kV. For this particular print head design, the use of low flow rates and low concentrations produced very thin jets that bent and looped when they impinged on to the substrate. The opposite was true for higher concentrations and flow rates where the more viscous, heavier deposits were able to absorb some of the impact energy and required a much higher applied bending stress to cause mechanical buckling. The optical micrographs (Figure 24) also revealed that as the frequency of buckling intensified the coiled deposits would coalesce to form thicker lines at higher applied voltages. The narrowest line width for this design was at 10kV with a 10wt% silk concentration with the flow rate set at 1.5  $\mu$ L/min (Figure 25a).

The insulated shafted print head produced a mixture of results with patterns containing excessive coiling, looping and zig-zag folding due to buckling instabilities in addition to patterns with good linear coherence. Unlike the reservoir design, the insulated shafted needle design forced high radial electrostatic stresses directly into the meniscus that enveloped the tip of the needle. As a result it can be expected that the electric field strength is at maximum near the tip of the electrohydrodynamic cone generating the jets thus bringing about a higher jetting velocity. Hence, the buckling instabilities were apparent at high concentrations and high flow rates. The high viscosities encountered in the jetting of the more concentrated silk

solutions (20wt%, 22wt %) would have resulted in very high compressive forces being applied on the jet as it impinged on the substrate during the printing process. Conversely, low concentrations and low flow rates produced the best results in terms of printed line width and pattern coherence with the narrowest line width of  $1.87\mu\text{m}$  being achieved at a 15% silk concentration with the flow rate set at  $1.5\mu\text{L}/\text{min}$ . The intensity of mechanical buckling as seen in (Figure 26) increased with increasing concentration. Increasing the concentration from 15wt% to 22wt% may have played a part in the mechanical buckling but other factors like conductivity, temperature and relative humidity would have influenced the final deposition.

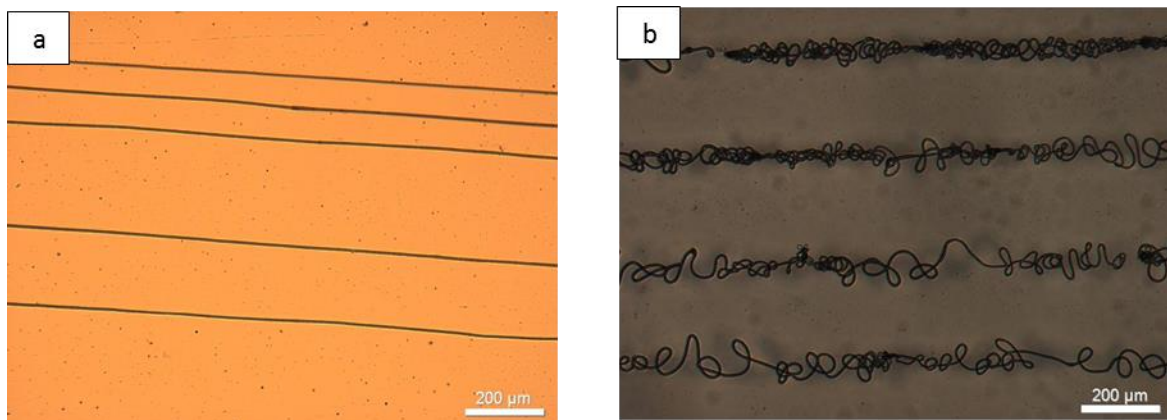


*Figure 26: Transition in the intensity of mechanical buckling as concentration of the silk solution was increased resulting in (a) straight printed lines becoming (b) non-linear. Print head used was insulated shafted, the flow rate was  $1.5\mu\text{l}/\text{min}$  and the applied voltage was set to  $12\text{kV}$ . The silk concentration (wt %) was 15 in (a) and 22 in (b)*

The pinhole reservoir print head was by far the best design in terms of jet stability and line width because it was able to deposit patterns in a controlled fashion for all applied voltages, flow rates and concentrations test with no visible whipping or buckling instabilities (Figures 24 and 25c). The narrowest line width printed with this design was  $1.05\mu\text{m}$  which was

obtained at 12kV using a solution concentration of 20wt% with the flow rate set at 1.5 $\mu$ L/min (Figure 13c). The only difference between the pinhole reservoir and the reservoir design is the size of orifice (compare (Figure 12(b) with Figure 13(b)). The smaller orifice (300 $\mu$ m) on the pinhole reservoir offered more control over the supply of solution to the meniscus in addition to narrowing the radial component of the electrostatic field lines. This coupled with the fact that the electrostatic pressure was applied from a distance ensured steady jet deployment.

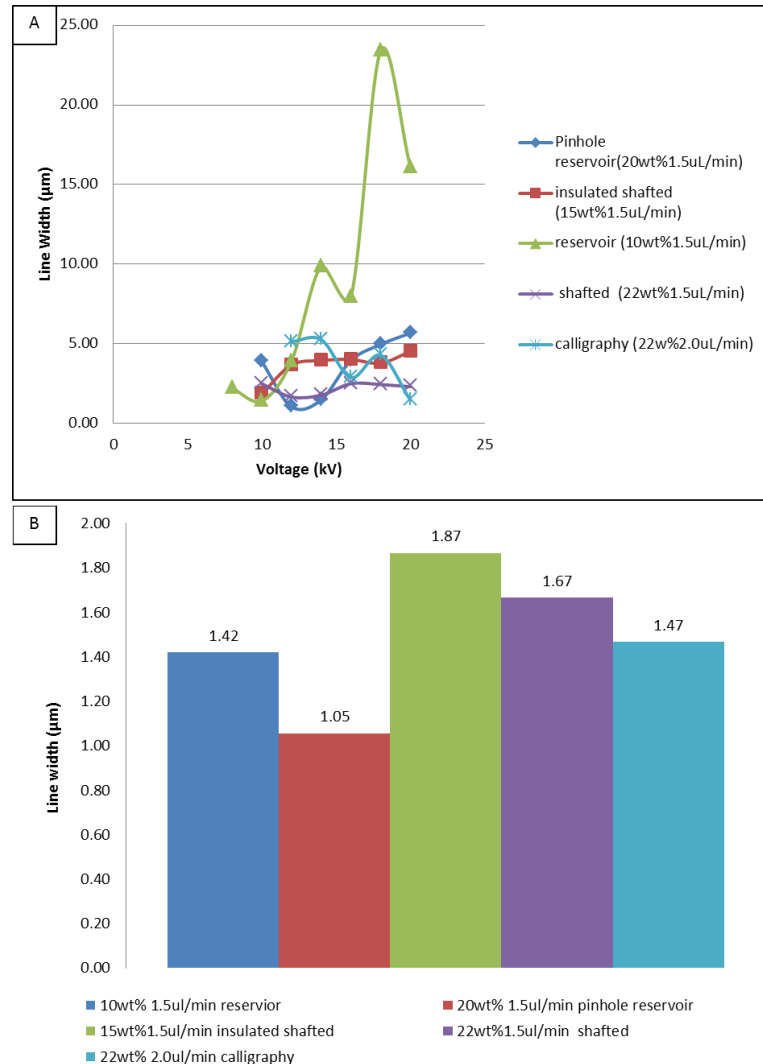


Figure 27: Print head designs tested in the work, (a) comparison of optimised silk concentration, flow rate, applied voltage and line width (b) comparison of highest line width

conical jets rarely changed or fluctuated as the voltage was varied from 10 to 20kV. Unstable

modes such as the pulsatile and intermittent cone-jet mode were non-existent. The presence of a reservoir ensures a constant and steady supply of solution to the meniscus thus preventing the meniscus from oscillating. Jet oscillations are usually brought about by competition between supply from the syringe and withdrawal of material caused by the applied electric field (224, 225).

### **5.1.3 Shafted and calligraphy print heads**

These were designed to enhance the lateral components of the applied electric field as opposed to the radial components. They each achieved this structurally in slightly different ways with the calligraphy design having a narrow slit down its middle and the slanted shafted print head having an 800 $\mu$ m orifice that tapers to a sharp needle point (compare Figure 15(b) with 16(b)).

Both designs behaved in a similar manner; with printed pattern line width (2-4 $\mu$ m) achieved for all applied voltages and flow rates at 22wt%, 20wt% and 15wt% silk concentration solutions. The largest line widths were recorded in both designs for a 10wt% concentration. This silk concentration has lower viscosity and surface tension properties (Table 3) thus creating and maintaining a stable jet was difficult without the appropriate stabilizing viscoelastic stresses. Enhancing the electric field strength in the lateral plane had the effect of throwing the jet off course during the printing process. This can be seen in (Figure 26) which indicated a significant degree of scatter, discontinuous and irregular printing. The ideal performances of the print heads are compared in (Figure 27)

In conclusion, the pinhole design proved to perform the best. The flow rate plays a vital role in maintaining steady jetting and is in turn dependant on the rheological and electrical properties of the printing fluid. The presence of a reservoir in the pinhole and reservoir print head designs allowed for a fluid flow process that was sufficiently slow to enable any intermediate state to be considered as an equilibrium state. This permits short electrical charge relaxation times and hence the criterion for classical electrohydrodynamic jetting stability  $Te/Th < 1$  is satisfied. The thickness of this meniscal charge is referred to as the charge relaxation length and is replenished by charge conduction which is determined by the dielectric constant and conductivity of the printing ink. The hypodermic needles used in these designs were each encased in a plastic shell made of polypropylene. Polypropylene has a low dielectric constant of 1.5 which was enough to weaken the electric field inside the shell to an extent that ensured jetting was not possible within the plastic shell. As a result, jetting only took place outside the plastic shell as the printing ink oozed out of the orifice.

This design is ideal for printing low conductivity solutions but would not work with highly conductive inks. This is because the jetting would take place even if the electric field was weakened since only a slight meniscal charge would be necessary to deform the meniscus into a Taylor's cone and thus enable jetting. Nevertheless, the design can be modified to allow this by making the shell out of a material with a higher dielectric constant so that effective reduction in electric field strength will be possible without inducing corona discharge between the needle and the shell. This is because the shell will start to behave like a faradays cage as it becomes more conductive.

The insulated shafted design introduced high radial electrostatic stresses directly into the meniscus which brought about jetting at high velocity. This design would be ideal for low conductivity printing inks but would not be suitable for highly conductive inks. The silicone sheath covering the tip of the needle helped funnel the printing ink to the tip. The intensified electric field would have also reduced the electrical relaxation time for specific concentrations which explains the good results obtained using the 15wt% silk solution. In a similar manner, the slanted shafted design introduced high radial electrostatic stresses directly into the meniscus but at a 45 degree angle. The angle enhanced the lateral electric field strength and as a result caused the electric field lines to spread out. This prevented stable printing.

The calligraphy design closely resembles two similarly charged needles placed next to each other. The design also featured plenty of sharp edges and points and would have meant that the charge density along these sharp features would have been very high bringing about intense electric fields. Once again, this proved detrimental to effective stable printing

The charge relaxation length and the applied voltage are key factors in cone-jet stability. Based on findings reported in literature [25] it is possible to predict the diameter of the cone jet by using the charge relaxation length since both values should approach unity when in the cone jet mode. The material properties can thus be manipulated to adjust the charge relaxation length which in turn affects the jet diameter and hence the eventual printing line width thereby offering the user a route to predicting printed line width from the material properties.

## 5.2 Evaluation of the Cartesian Robot (human ear like construct)

### 5.2.1 Solution properties of Polycaprolactone

Table 4: Physical properties of polycaprolactone solutions used in the experiments. All % refer to weight

Solution	Density(kgm <sup>-3</sup> )	Viscosity (mPa s)	Surface tension (mNm <sup>-1</sup> )
Dimethyl Carbonate	1.08	1.44 ±0.2	30.5 ±0.3
PCL 7%	1.10	26 ±0.2	31.2 ±0.6
PCL 10%	1.13	34.3 ±0.2	32.5 ±0.2
PCL 12%	1.16	73.7 ±0.1	33.3 ±0.8
PCL 14%	1.18	133.5 ±0.2	35.3 ±0.7
PCL 15%	1.20	192.8 ±0.4	40.3 ±0.5

The design and construction of new hardware warrants an investigation to demonstrate its capabilities and areas of improvement. Thus the system validation for this machine involves the attempt at fabricating a human ear (Figure 28). Thin continuous micrometer sized jets are pulled out of a meniscus suspended from a print head with a 800µm nozzle in the presence of an high electric field. This fine jet represents a small ratio of jet diameter to nozzle diameter and is used to fabricate the 3D construct in this study. The printing takes place within petri dish filled with distilled water that offers a lucid cushion like surface to print on. As layer after layer of PCL is deposited, an equal volume of water in the petri dish is displaced thus allowing the construct to grow with minimum resistance. The petri dish was grounded to ensure that the positive charges being delivered to the petri dish by the electrohydrodynamic jet during the printing process were neutralised.

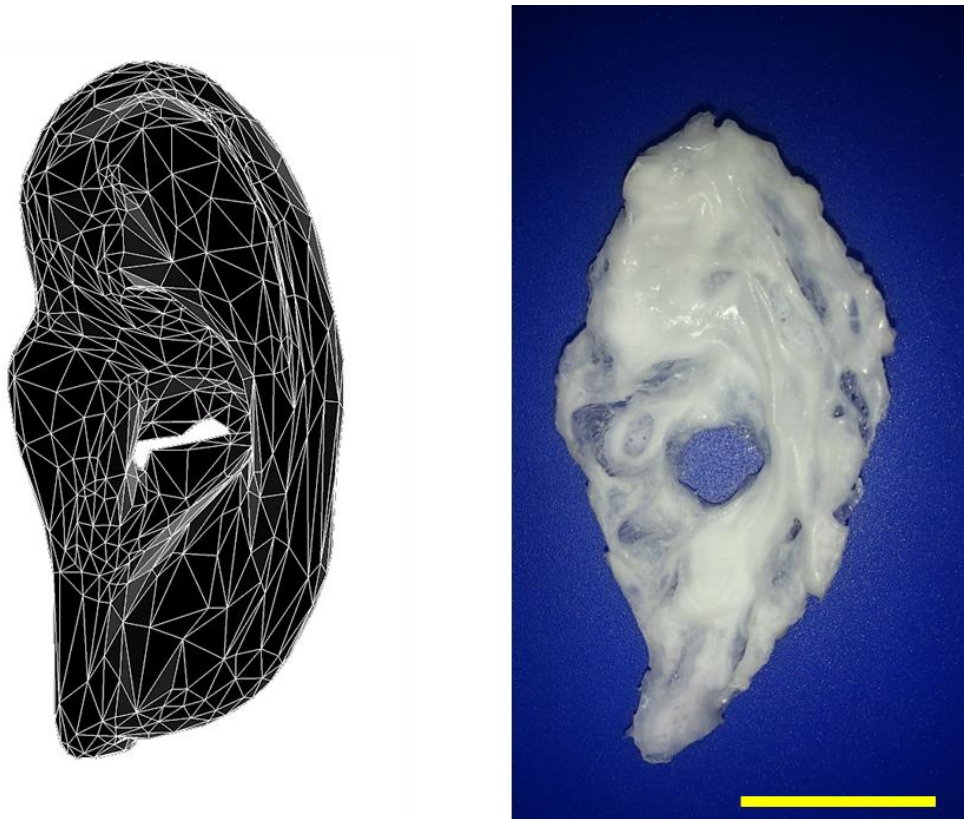


*Figure 28: The three-dimensional STL construct compared to the actual printed construct (scale bar = 15mm).*

For the five PCL solutions that were investigated, we can see from (Figure 29 a-e) the gradual evolution of the intended construct from a structure that possess no resemblance to a human ear (Figure 29a) to a 3D human ear like construct (Figure 29e) . The use of a grounded water bath ensured the rapid precipitation of the PCL which is mainly due to PCL's high hydrophobicity for water. This precipitation became more prominent with the increase in PCL content in the printing solution. Printing solutions with lower concentrations (7%, 10%) tended to spread along the surface of the water bath as they were deposited which is illustrated in (Figure 29 (1-3)) where the dark, condensed portions indicate where the material has been deposited in significant amounts. The increased solvent to solute ratio made it harder for the precipitated PCL to remain in place because as the solvent DMC dissolved in water it would carry the PCL away with it. Thus shape integrity and uniformity was difficult

to control when using low concentrations of PCL. At high concentrations (15%,14%), the first few layers deposited were more than enough to anchor down the construct and offer a firm printing surface onto which subsequent layers of PCL could be deposited. The higher viscosity also contributed towards distinct features like the inner folds of the ear to become more pronounced (Figure 29e and 29(5)).

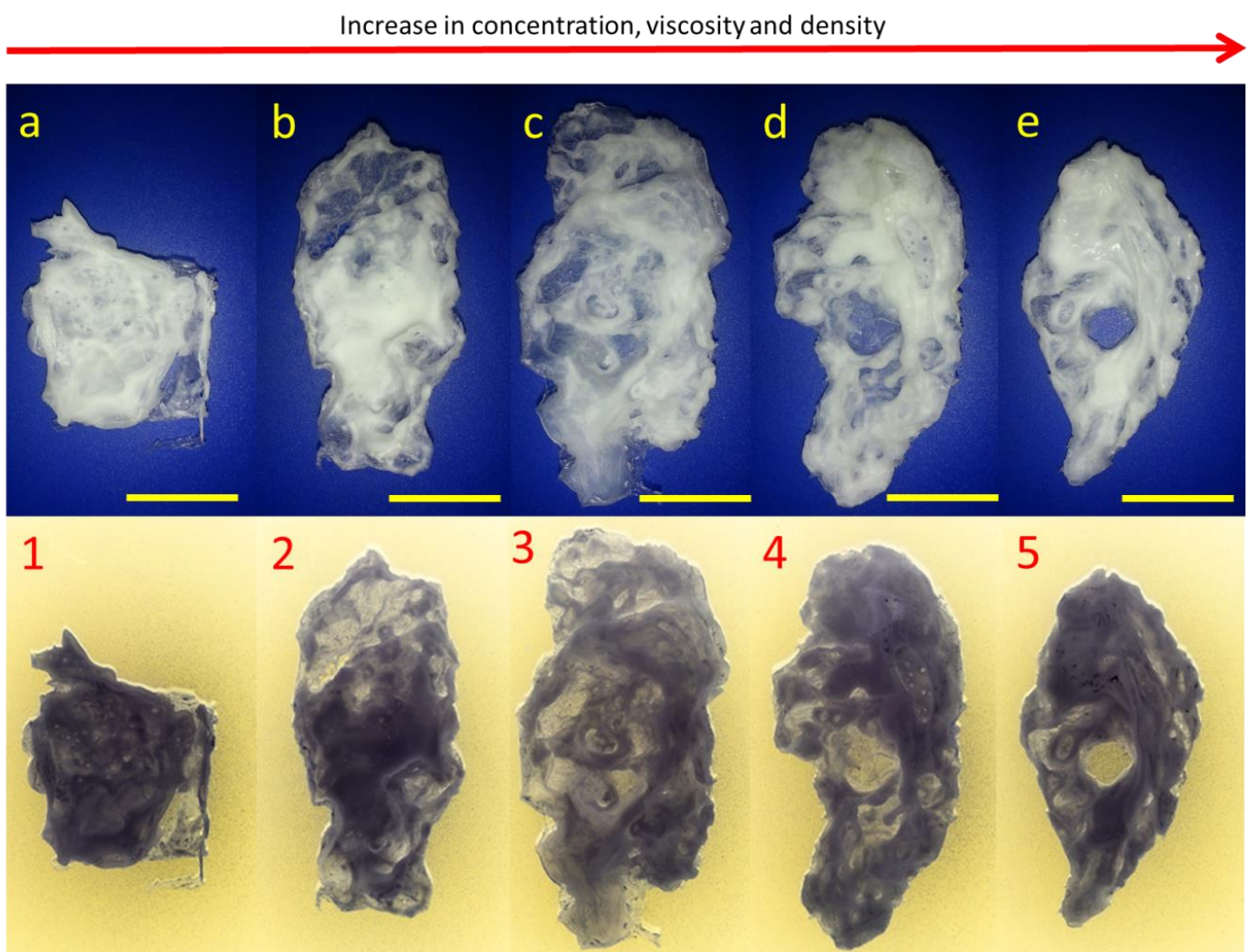


Figure 29: The gradual evolution of the construct with respect to concentration, viscosity and density (scale bar 20mm).

Construct shrinking was an issue with all prints. Almost all the constructs contracted in height and width by about 20% as the solvent evaporated, see fig (30(a, b)). The use of low PCL concentrations brought about the shrinking in both the height and width.

Concentrations exceeding 15% proved to be too viscous to work with since they often solidified within the silicone tubing and clogged up the print head during the print.

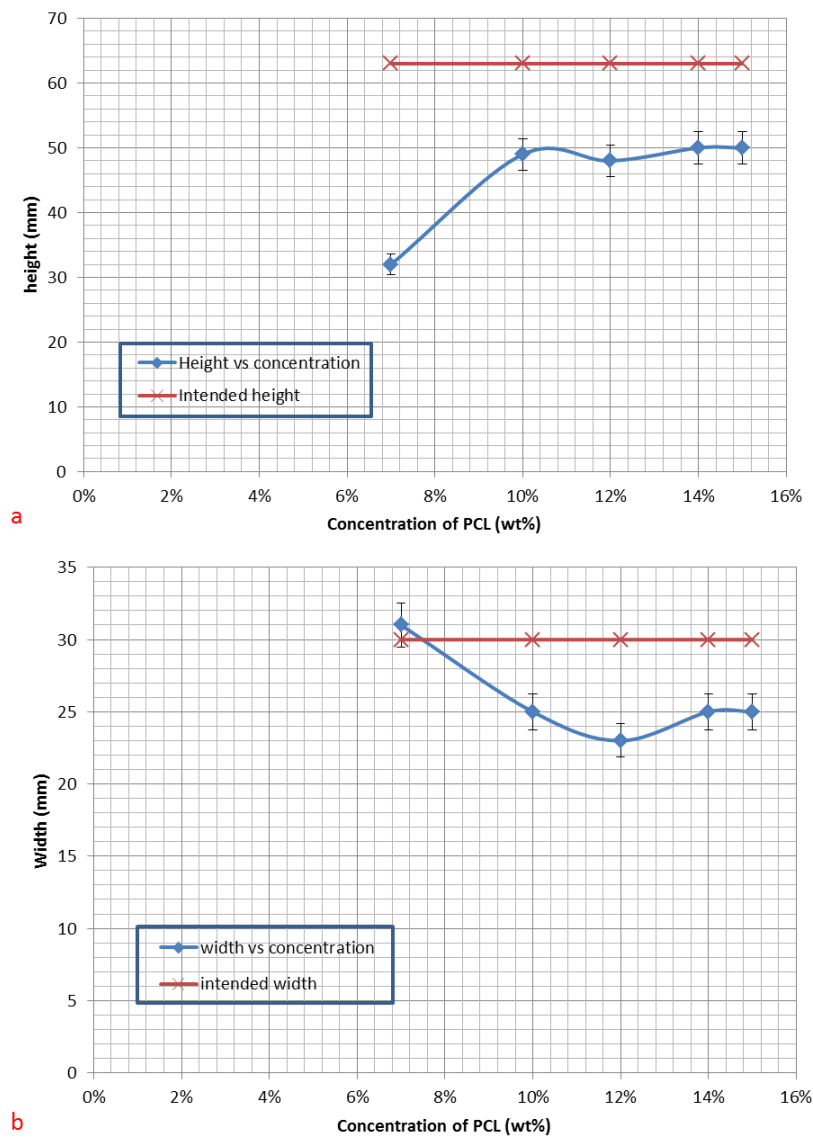


Figure 30: A comparison of the shrinking observed in the constructs. a) height b) width

(Figure 31) illustrates the ideal operating regimes within which a stable 3D construct can be printed while maintaining a continuous jet in the cone-jet mode for the duration of the print (190 minutes). The higher viscosity solutions (15%, 14%, and 12%) required a higher electrostatic force to overcome the surface tension at the meniscus for jetting to take place. The increased PCL content would have restricted the mobility of charged ions and molecules and therefore to overcome this, higher voltages (4 and 6kV) and higher flow rates (40 and 60 $\mu$ l/mn) were required for 14% and 15% solutions. The high flow rates and low standoff heights of (30mm) served to force the continuous jet along a linear path to the surface of the water bath, thus preventing the chances of varicose and whipping instabilities from arising in the jet.

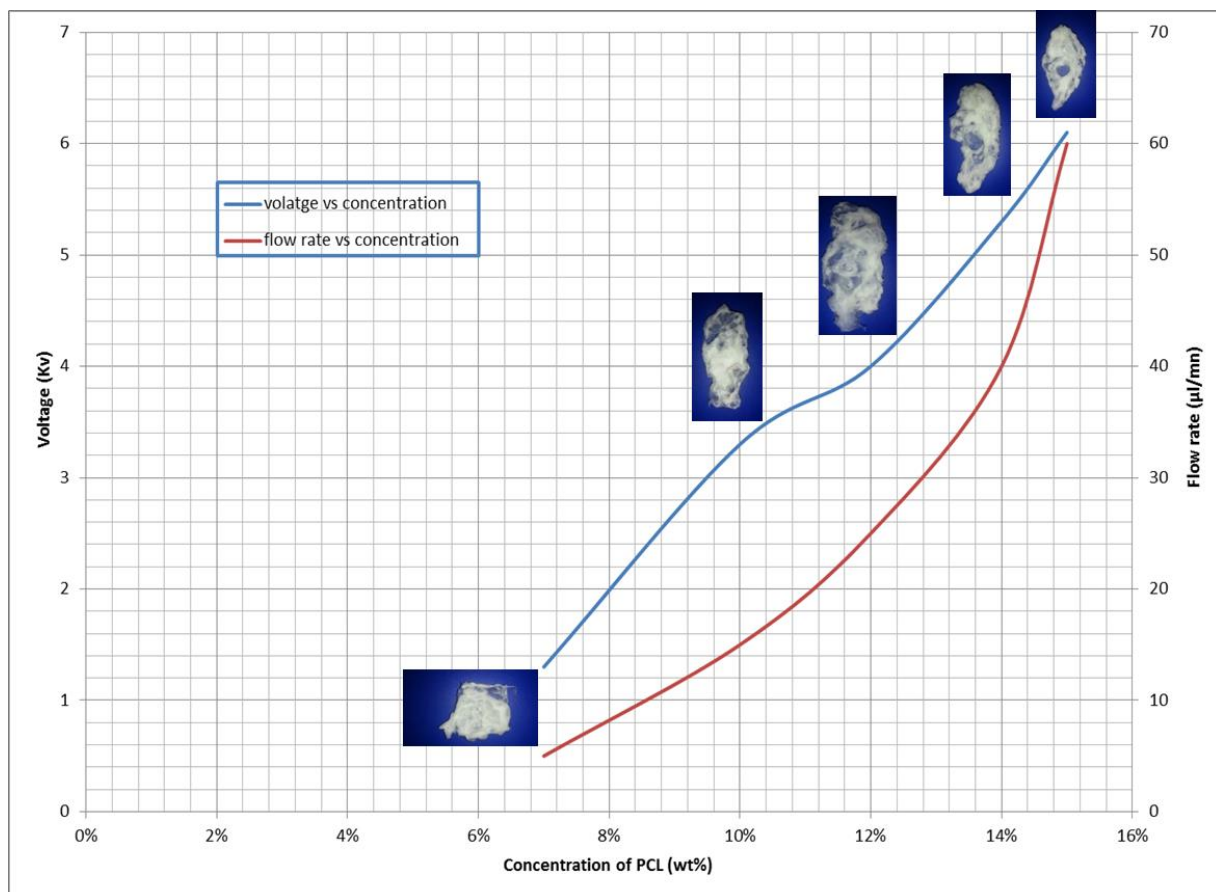


Figure 31: The printing operating envelope

Close up examinations of the printed constructs revealed that successive layer by layer deposition was accurate as can be seen in (Figure 32i). Similarly when printing with the high viscosity solutions (15% and 14%), minute air bubbles were found trapped at certain points in the constructs (Figure 32III). This only occurred when the print was focused on an area or region that was intended to be thicker or required more material for extra support.

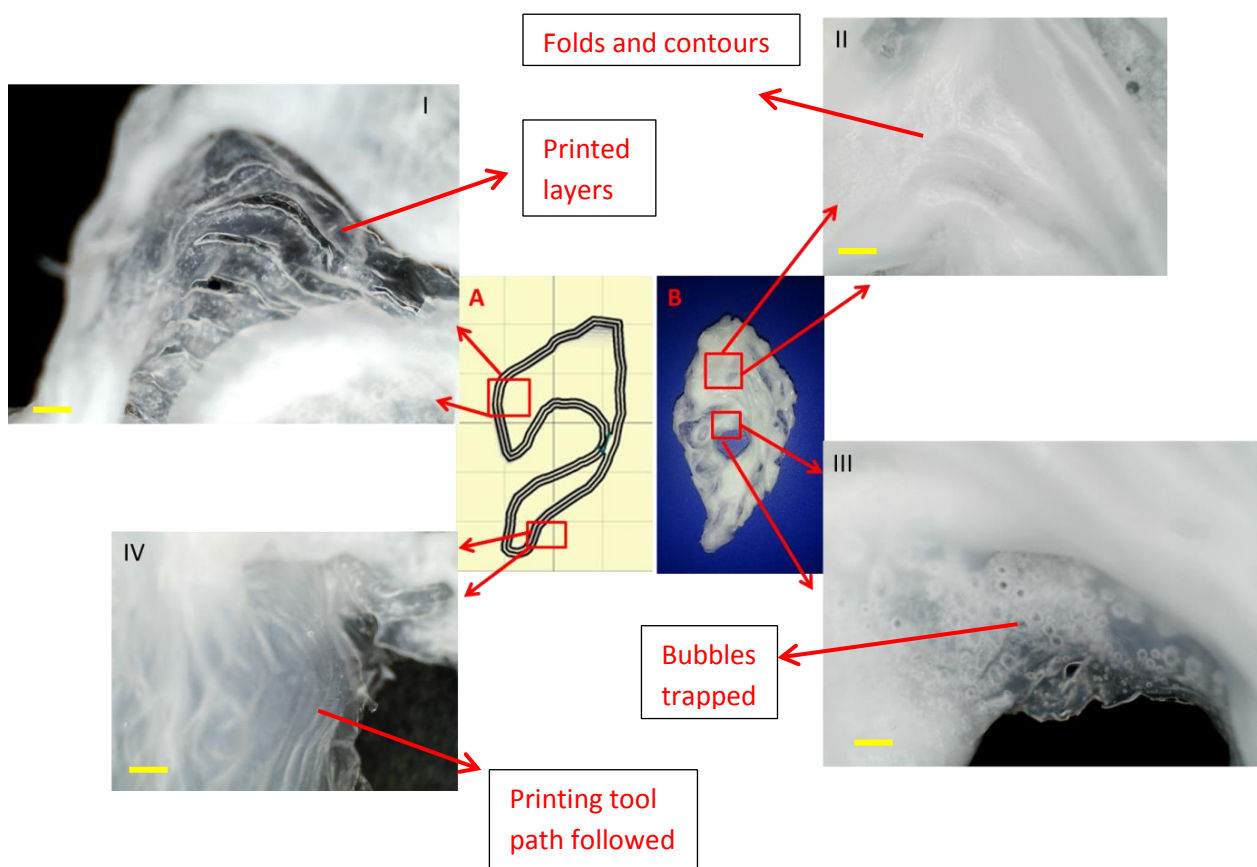


Figure 32: Light microscope plane view of key features of the construct. a) Live screen capture of the tool path taken during the print b) actual construct (scale bar=1mm)

### 5.3 Evaluation of the Cartesian Robot (Nasal septal scaffolds)

#### 5.3.1 Solution properties of Polycaprolactone

Table 5: Physical properties of PCL solutions used in the experiments. All % refer to weight

Solution	Density (kgm <sup>-3</sup> )	Viscosity (mPa s)	Surface tension (mNm <sup>-1</sup> )
Dimethyl Carbonate (%wt)	1.08	1.44 ±0.2	30.5 ±0.3
PCL 15%	1.20	192.8 ±8	40.3 ±0.5
PCL 18%	1.45	225 ±6.25	42.5 ±0.2
PCL 23%	1.90	875 ±161	65.3 ±0.8

The CAD of the nasal septal scaffold (Fig. 33a) was uploaded to the printer sliced into 18 layers and converted into G-code which specified the exact tool path (Fig. 33b) to a 3D finished product (Fig. 33c). The septal scaffolds were prepared at three different concentrations (15wt%, 18wt% and 23wt %).

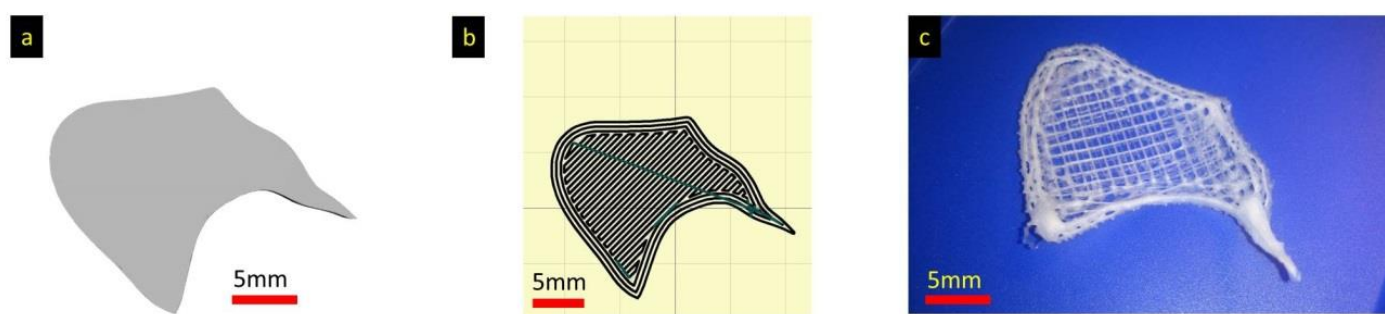


Figure 33. The printing route from STL File to the final printed construct a) The three-dimensional STL construct b) Printing tool path for one layer c) The actual printed construct

Systematic AFM PeakForce QMN of the scaffolds revealed that the DMT modulus increased from 213-647MPa with the increase in polymer concentration from 15% to 23%. This finding was further supported by differential scanning calorimetry which indicated that the degree of crystallinity increased from 15% to 44% as the concentration increased from 15% to 23% (Figure. 34). This can be attributed to the electrostatic field which induces molecular orientation of the PCL chains due to the tensile pulling and stretching forces that are exerted during the printing process, thus improving the degree of crystallization, which in turn explains the gradual rise in measured DMT modulus values.

Moreover, the increase in molecular chain alignment assists in inducing further crystallization since the aligned molecular chains serve as nucleation sites for further crystallization to initiate along the rows of aligned PCL chains thus enabling extensive crystallization to take place at higher concentrations (23%) [226]. The higher concentration also prevents chain mobility thus restricting beading from forming along the printed filaments. The DMT modulus of the scaffolds can also be manipulated by either increasing or decreasing the number of printed layers. The accumulative effect of stacking layers of polymer successively would have also contributed to the high modulus values. In this case, the number of layers 18, is kept constant throughout the investigation. Thus the technique offers means to alter mechanical properties of the printed scaffolds to suite the in-vitro biological requirements.

The DSC thermograms also revealed that on cooling, maximum crystallization occurred at temperatures between 28-30°C which was close to the ambient temperature (25°C) in which the samples were left to rest once printed. Residual solvent may have permitted further chain

folding and hence increased crystallization, post-printing. Lower concentrations (15% and 18%) tended to show two peaks placed close to each other suggesting crystallites of differing sizes embedded within the PCL filaments (Figure. 35). The lowest concentration (15%) had two peaks in the first heat/cool cycle at 56°C and 59°C that became more distinct in the second heat/cool cycle to give two sharp peaks at 48°C and 55°C. The observed effect became less severe as the concentration was increased to 18% where one broad melting peak can be seen.

The highest concentration (23%) also showed only one melting peak at 60°C. This trend highlights key events that took place during the printing process with respect to the crystallization profile at different concentrations. Printing at lower concentrations tends to lead to non-uniform crystallization that is further exacerbated by low flow rates of (20 $\mu$ l/min) and rapid solvent evaporation brought about by finite jetting. The polymer chains at these

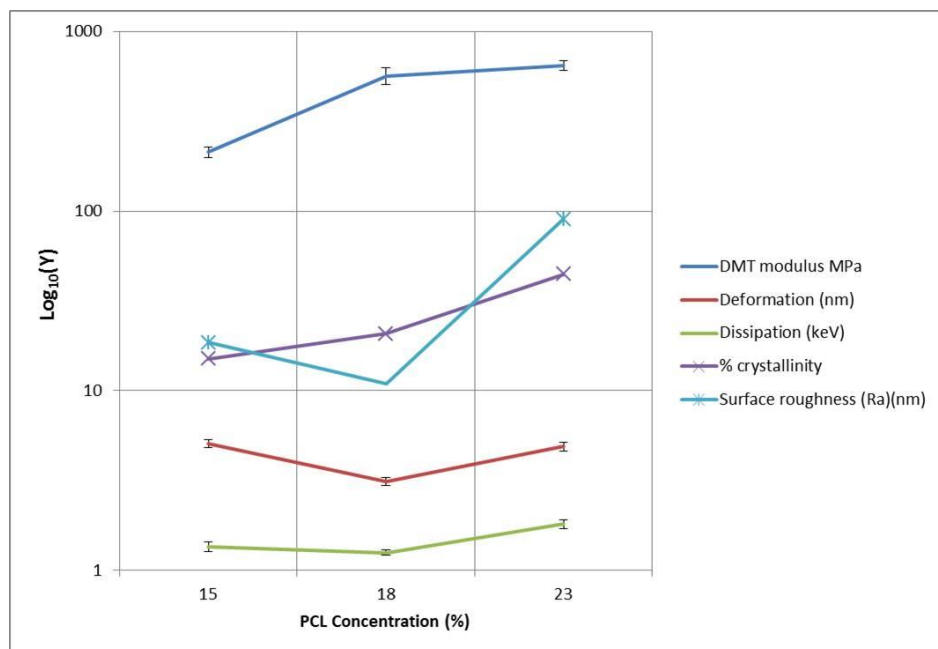


Figure 34: A comparison of DMT modulus, deformation, dissipation, surface roughness and crystallinity (represented as Y and defined in the legend) as a function of concentration.

printed concentrations (15% and 18%) do not have enough time to fold and re-organize themselves into a thermodynamically energetically favourable crystallized state. Upon increasing the polymer content, a knock-on domino effect was detected as increasingly aligned molecular chains assisted in inducing crystallization in addition to making the process uniform thus resulting in a gradual rise in melting temperature from 56°C and 59°C at 15% to 60°C at 23%.

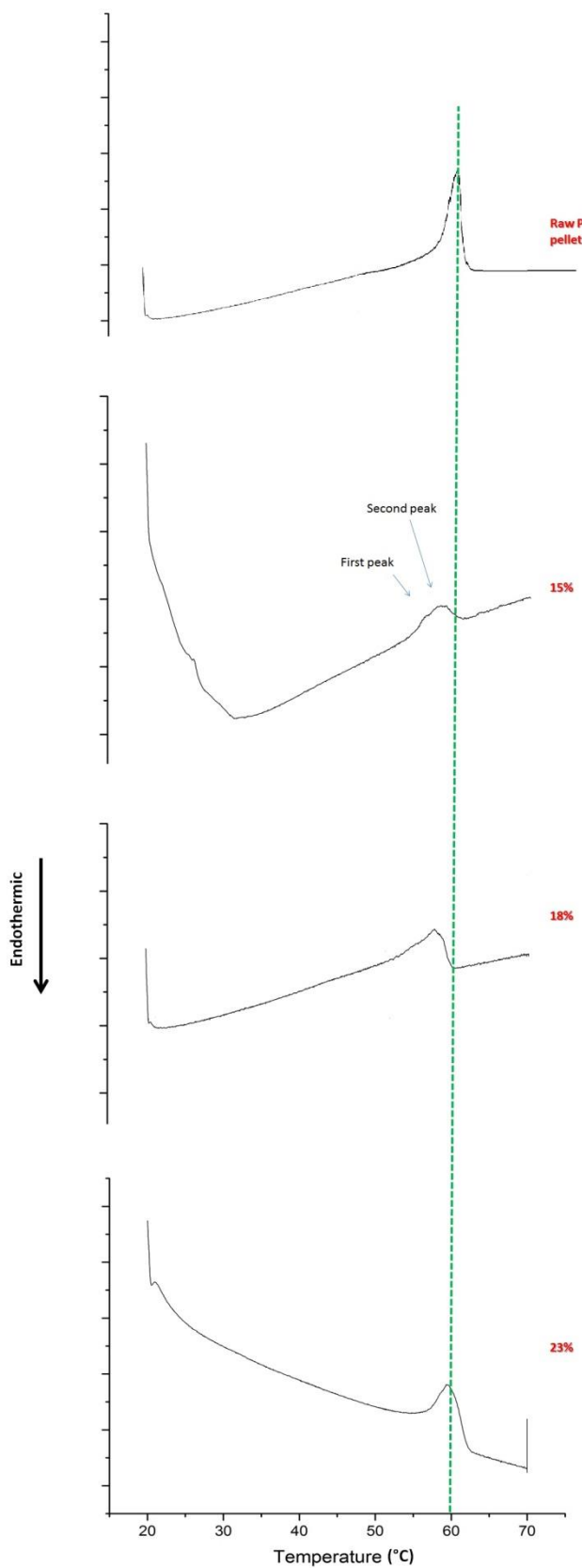


Figure 35. Differential scanning calorimetry traces illustrating the thermal history of scaffolds prepared

Further analysis of the AFM PeakForce QNM data showed that the DMT modulus and deformation curves appear to be inversely correlated while the deformation and dissipation curves are complementary (Figures 36-38). The results were obtained as an average of 256 data points on the test sample. Increases in deformation from elastic and plastic contributions led to increases in energy dissipation while increases in DMT modulus, leading to minimal cantilever induced deformation for all concentrations tested (Figure. 34). Since polymers exhibit viscoelastic behaviour which is a time dependant material property, the deformation induced during the AFM sampling would have been plastic deformation which is permanent.

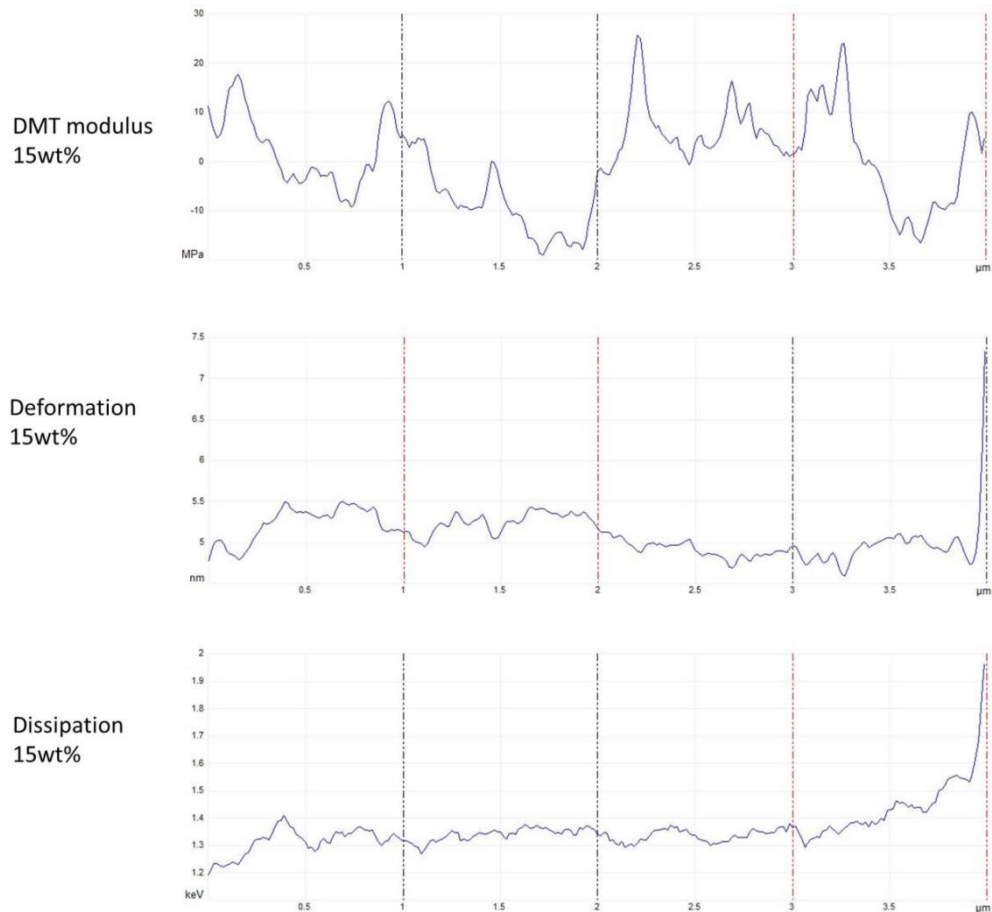


Figure 36: The variation in DMT modulus, deformation and dissipation for 15wt% with respect to the position along sample area.

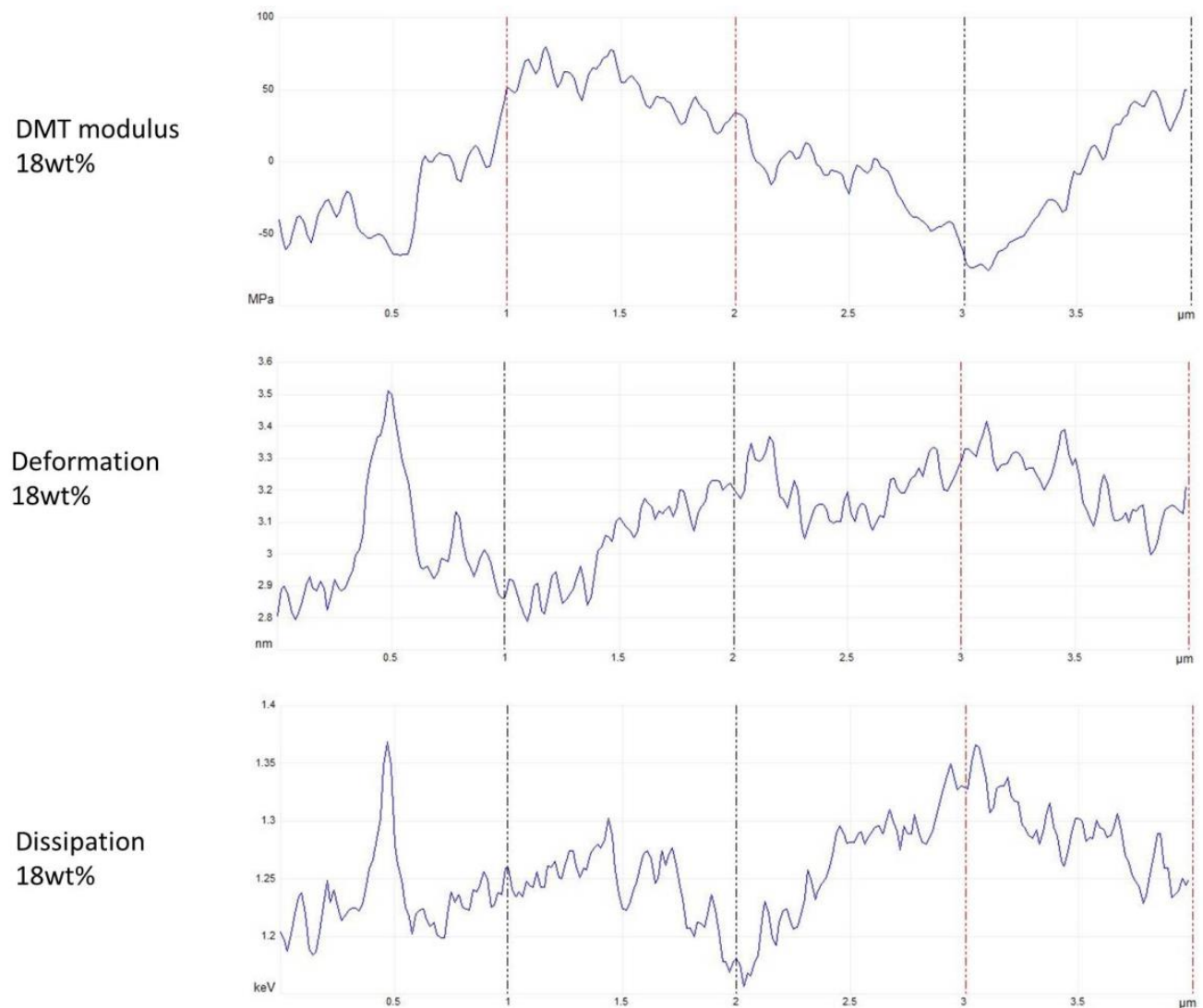
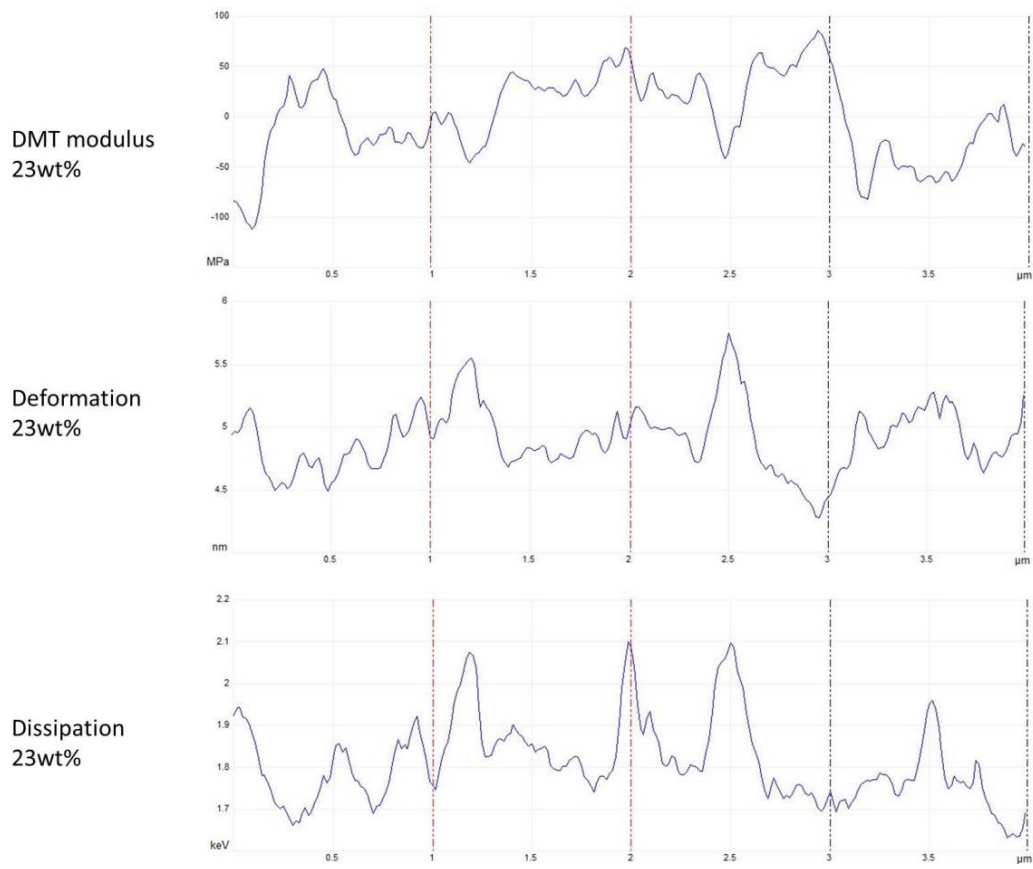


Figure 37: The variation in DMT modulus, deformation and dissipation for 18wt% with respect to the position along sample area.



*Figure 38: The variation in DMT modulus, deformation and dissipation for 23wt% with respect to the position along sample area.*

The measured printed PCL filament diameter (line width) was also found to increase with increasing concentrations from  $20 \pm 5.3 \mu\text{m}$  for 15% to  $105 \pm 34.36 \mu\text{m}$  at 23% (Figure. 39). It must be noted that the highest measured printed line width of  $20 \pm 5.3 \mu\text{m}$  at 15wt% in this work is similar to reported printed line width of scaffolds made using electrohydrodynamic printing of 70wt% PCL dissolved in acetic acid [227]. There was no noticeable trend in the change of surface roughness of the printed scaffolds with the highest Ra value recorded at 90 nm for 23% and the lowest at 11nm for 18% (Figure. 34 and 40). The surface roughness is vital for good cell adhesion but since PCL is hydrophobic, thus specific surface

functionalization or hydrophilic coatings using biopolymers like collagen will be needed to make electrohydrodynamically printed PCL scaffolds effective[228,229].

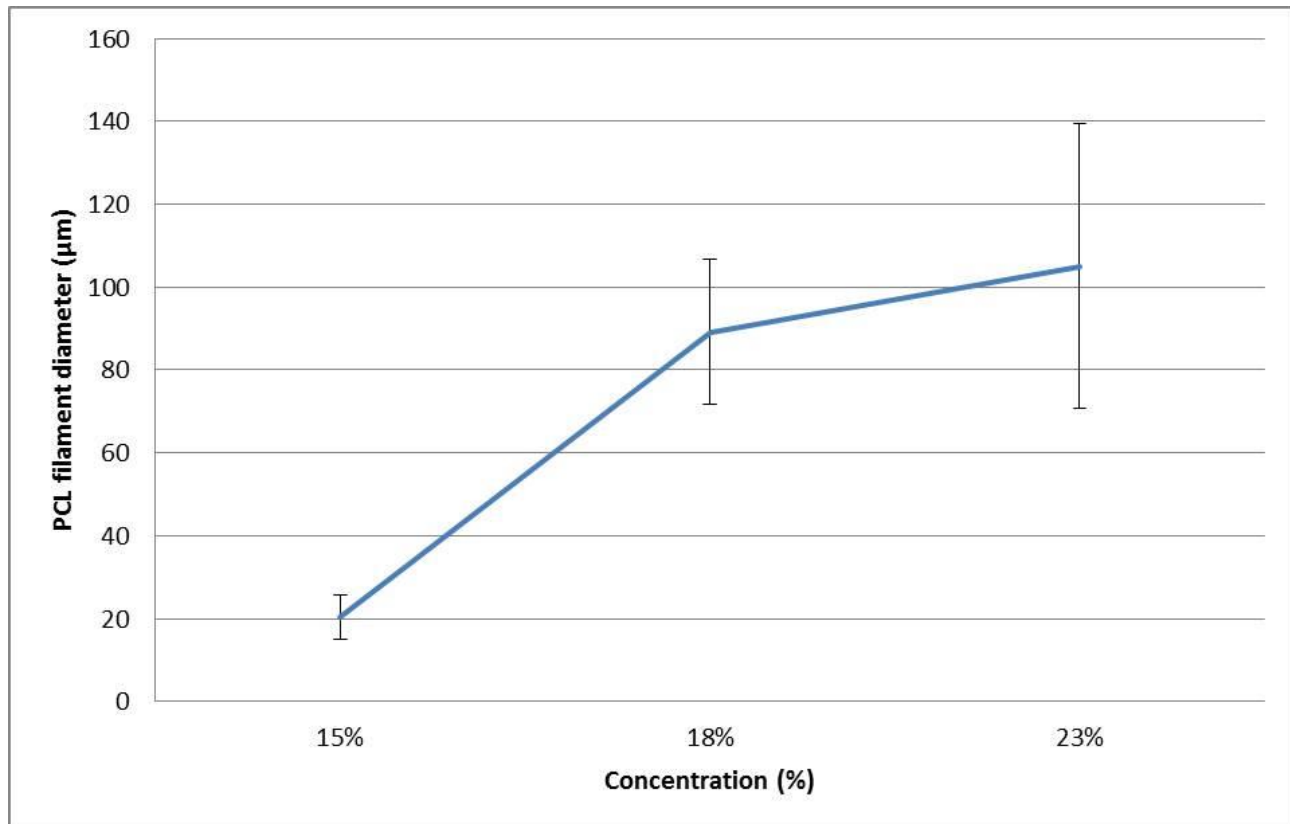
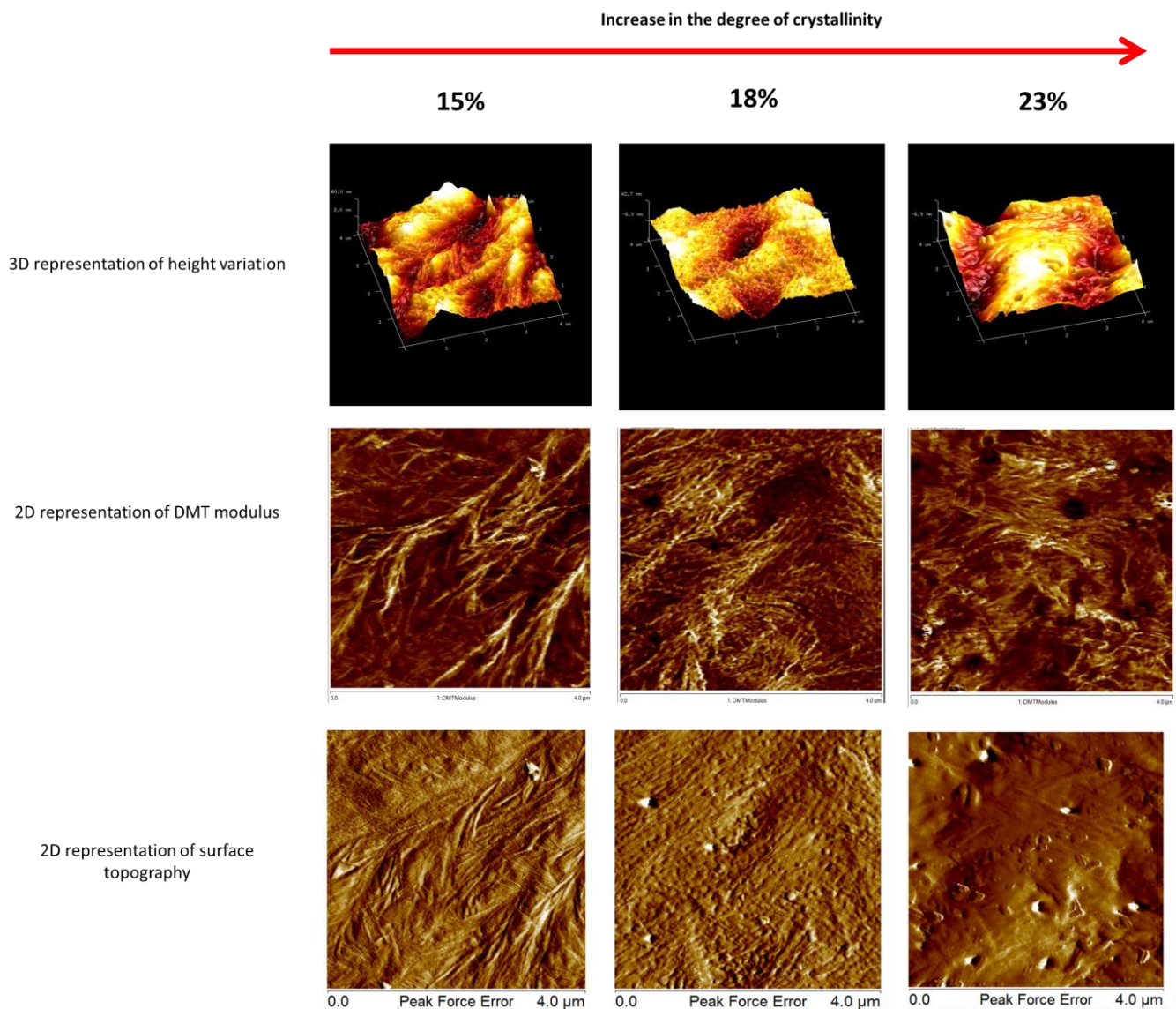


Figure 39: A comparison of how PCL filament width (line width) varies with PCL concentration

Figure 41 shows the effect of varying the polymer concentration, flow rates and applied voltages. It was observed that at low concentrations, primary dispensed PCL filaments were susceptible to whipping instabilities thus resulting in coiled deposits. This coiling became less severe after two or three printed layers (Figure. 41 D) as subsequent PCL filaments were deposited in a parallel aligned manner. As a result it was possible to create PCL constructs embedded with both ordered and disordered configurations using a 15% solution. As the concentration was further increased to 18%, once again the primary dispensed filaments whipped and coiled into a woven mesh like platform upon which thicker filaments (89

$\pm 17\mu\text{m}$ ), which were less likely to bend and coil, were deposited in an ordered rectilinear fashion (Figure. 41 E). The highest concentration yielded a purely ordered rectilinear patterned scaffold with the thickest PCL filaments measuring at  $105 \pm 34.36\mu\text{m}$ . Prior studies [230,231] have shown that cells prefer a random, disordered scaffold architecture for ideal cell adhesion, proliferation and differentiation. This effect was attributed to similarities between extracellular matrix supports and disordered frame-works.



*Figure 40: Typical two and three dimensional depictions of the height variation, DMT modulus and surface topography of the scaffolds prepared*

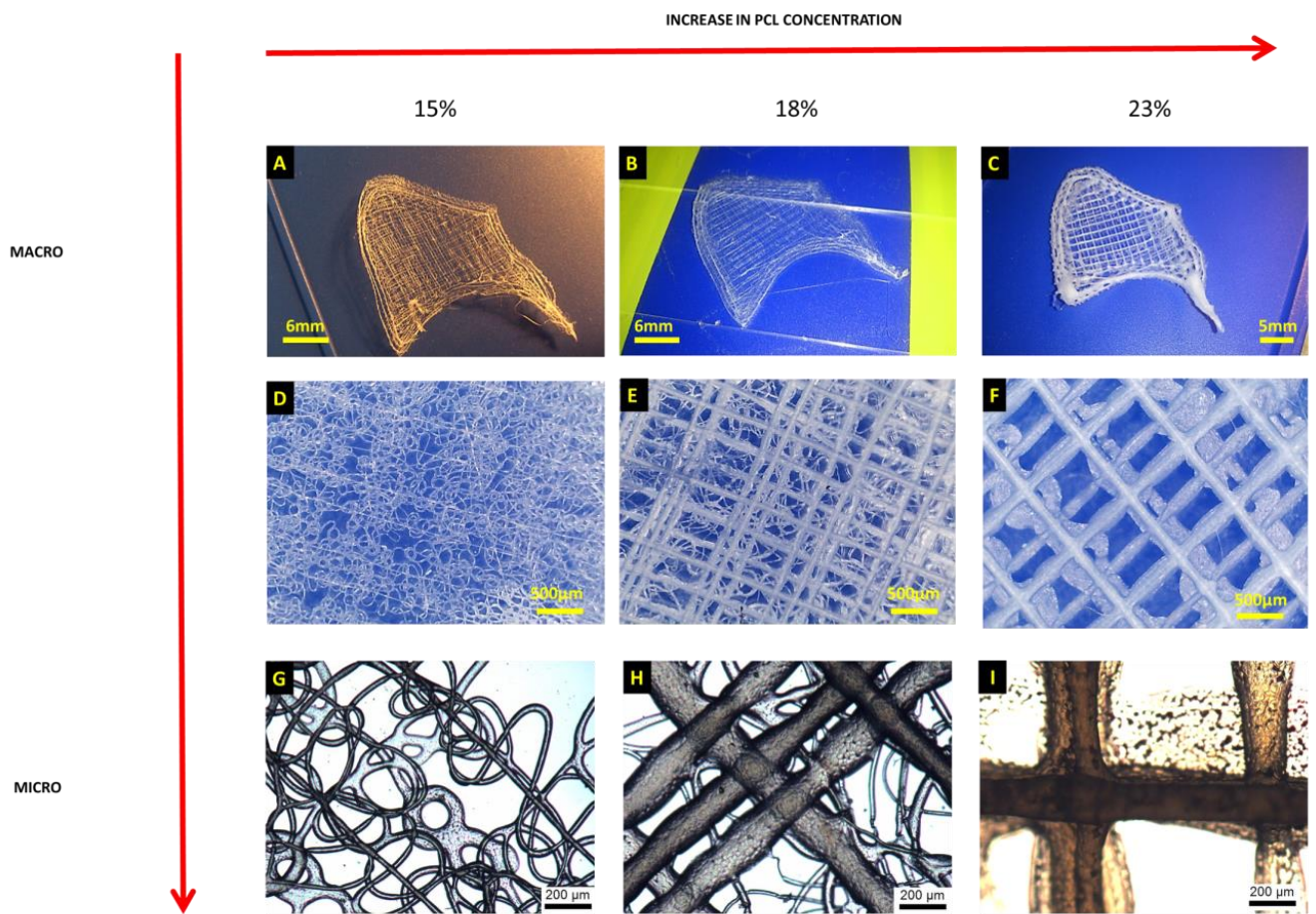


Figure 41: The nasal septal scaffolds printed shown at different length scales

An FTIR analysis was conducted to identify the composition of the scaffolds. The results show a characteristic C=O peak at  $1723\text{ cm}^{-1}$ ,  $\text{CH}_2$  asymmetric stretching at  $2945\text{ cm}^{-1}$  and symmetric stretching at  $2865\text{cm}^{-1}$ , C-O-C stretching at  $1241\text{ cm}^{-1}$  and C-O stretching at  $1170\text{ cm}^{-1}$ , all belonging to PCL (Figure. 42). Nevertheless, dimethyl carbonate (DMC) also shares similar functional groups with polycaprolactone and thus we cannot conclusively state that DMC has been completely removed.

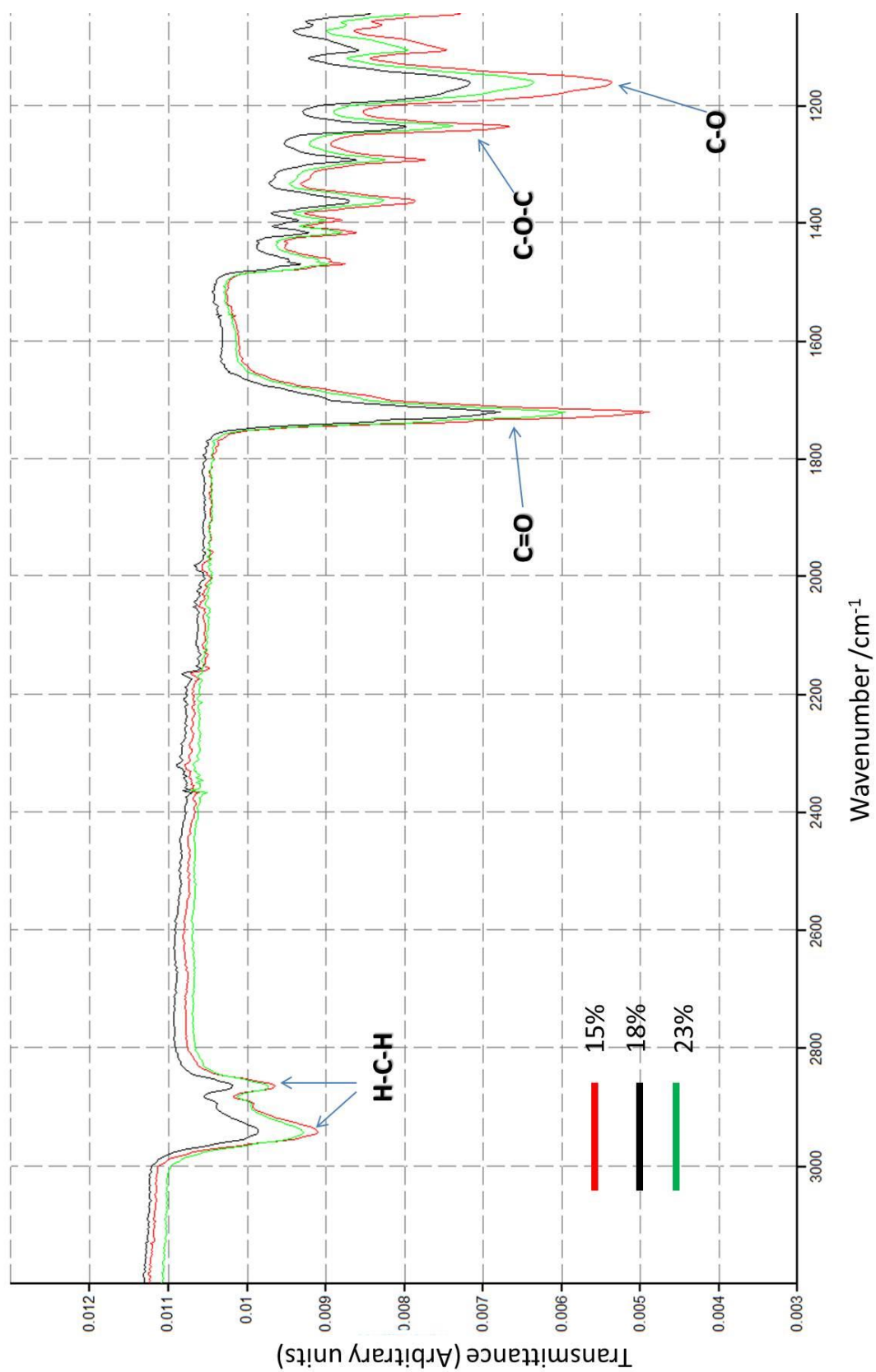


Figure 42: FTIR spectra highlighting key peaks detected

## CHAPTER 6 CONCLUSIONS AND FUTURE WORK

### 6.1 Conclusions

The research work undertaken attempted to produce an Arduino based 3D electrohydrodynamic printer with micrometer scale printing capability. Initial attempts at producing printed lines with a line width in the submicron and nanoscale ( $<1\mu\text{m}$ ) produced varied and inconsistent results and were thus not reported. This led to the investigation of print head design in an attempt to shape and improve the electric field line distribution between the nozzle and the substrate.

Five different print head designs with  $800\mu\text{m}$  diameter needles were used to print silk patterns that had an average line width which varied between  $1\text{-}10\mu\text{m}$ . The results show that modifying the print head design of the needle has a significant effect on line width of the silk patterns produced. Thus, by using needle orifices that were much larger than those used in previous work we were successful in printing lines with widths that were of the order of  $1\mu\text{m}$ . Therefore, this study indicates potential and highlights an alternative route to achieving fine line widths in printing without the need to reduce the needle diameter. The investigation of insulated shafted, reservoir and pinhole reservoir designs highlighted some key features that need to be incorporated in future print head development. The use of sharp tip needles to introduce highly intensified electrostatic stresses directly into the meniscus will produce stable prints only under specific conditions. This drawback can be overcome by pulling the needle back to a distance of about 5mm from the meniscus and applying a concentrated radial electric field.

The use of a reservoir ensures that a steady and stable supply of printing ink to the needle print head. This is critical to the stability and congruency of the shape and volume of the cone jet at the tip. This can be further regulated by virtue of a small orifice at the base of the reservoir. More importantly, the reservoir reduces the electrical relaxation time for stable taylor cone formation. The concept of using sharp conductive tips to introduce highly intensified electrostatic stresses was used in a similar manner by researchers in [66] to reduce the hysteresis time in generating a Taylors cone. Attempts to reduce satellite spray that is caused by electrohydrodynamic jetting have led researchers to use ring shaped gated electrodes to focus electric field lines around the nozzle [64] and plates with holes between the nozzle and substrate to direct the electric field lines. Interestingly, the pinhole design is capable of achieving the same effect through the use of a polypropylene shell made out of a material with a low dielectric constant to weaken the effect of electric field lines that do not follow a trajectory that is perpendicular to the substrate. This leads to reliable prints in the continuous mode.

Applying an electric field with a tilted configuration proved to be detrimental to stable printing since it was difficult to control the jetting trajectory while attempting to print straight lines. Having the print head positioned at a  $45^\circ$  to the substrate would have prevented the formation of closely spaced linear electric field lines. As a result the delicate force balance that must exist (cone-jet mode) between surface tension and electrically induced electrostatic stresses would have been hard to maintain thereby leading to haphazard and discontinuous lines. The variations and fluctuations in printed line width could also be linked to the quality of the silk solutions produced on the day the experiments were carried out. It was difficult to produce silk solutions with identical rheological properties despite measurements of surface

tension, electrical conductivity and dialysed solution concentration for quality control and standardization purposes. It is clear from the results that specialised print heads would have to be fabricated to suite specific purposes as described in work reported by [55]. They used the drop on demand process to fabricate patient specific drug units by pumping drugs through an insulating inner nozzle which was encased within an outer conductive electrode thus effectively preventing electrochemical reactions from taking place at the fluid-electrode interface. Further work described in [56] showed how placement accuracy of active drug molecules could be improved by placing an inverted microscope (IX51, Olympus, Japan) under a transparent glass printing.

We attempted to develop a portable desktop electrohydrodynamic printer with the capability of controlled deposition at a range of flow rates, applied voltage and printing solution viscosities using replication rapid prototyping technology. The union of RepRap technology with Electrohydrodynamic phenomena has proven to offer greater design freedom and geometrical versatility for EHD printed constructs when compared to attempts reported in literature. The open source programs that accompany this technology are easily available and make it possible for users to make attempts at printing complex and elaborate constructs with minimal effort. For example, the G-code that dictates the toolpath can be easily manipulated using easy to use open source software such as G-Code Ripper. This allows less experienced users to tailor their STL files to meet their needs without the requirement for specialist knowledge. At the same time, simple 3D modelling software's like Google sketchup can be used to draw up the constructs that are to be printed.

We were also able to show how this open source prototyping technology was used to receive inputs of humidity and temperature within the confines of the printing chamber and then subsequently act upon them to bring about a change. Previous attempts at reducing the cost of such printers reported in [48] could only bring the cost down to <\$50,000 with nearly similar functionality. The printer designed here would cost well under £1000. Nevertheless, work reported in [55] illustrates how nozzle design would have to be tailored for specific purposes.

The Arduino boards were also programmed and used in conjunction with small cooling fans to cool down the electronics during the course of a print. The problems associated with the previous printer described in chapter four pertaining to the overall frame and hardware resolution were alleviated as we were able to increase the hardware resolution to  $10\mu\text{m}$  from  $24\mu\text{m}$ . The vibrations and tremors encountered with the previous printer [135] can be avoided by orthogonal positioning of the respective axes (x,y,z). This printer also featured a flat ground electrode which we found to have no effect on either the stability of jetting or printed line width when using the Pinhole reservoir, reservoir and insulated shafted print head designs. The findings are contrary to previously reported findings [65].

The printer was constructed out of a non-conductive material (polypropylene) which reduced the electric field interference from external sources but did not eliminate the field within the printing chamber. Additionally, it also served to confine the printing area to a controlled ambient environment. This setup also served to protect the user from static discharge from metallic surfaces while also offering protection from the harmful fumes of the solvents used. Furthermore, the environment can be manipulated to allow for the introduction of a partial ionisable gas to stabilize the jetting. The polypropylene construction would not be able to

neutralize the ionized gas. This design feature was incorporated based on findings reported in [32] where significant gains were made in controlling capillary jets of glycerol and polyethylene oxide (PEO) through the partial neutralization of surface charges on the jets brought about by the ionization of the gas in the immediate vicinity of the cone-jet. They also reported that the ions produced had a contribution to the final measured current values at the counter electrode [32-34]. The study where an attempt at a human ear replica was made has highlighted the need for the optimization of the material formulations for accurate and instantaneous deposition of material during the printing process. It was a struggle to print 3D structures to a height greater than 5mm. This was as a result of subsequent charge build up in the printed layers that generated their own static electric field which interfered with the electric field between the print head and grounded substrate. This happened despite print depositing inside a grounded the petri dish filled with water. This led to work with simple 3D structures.

The electrohydrodynamic printer would benefit from a real time feed-back loop to compensate for the effect of intrinsic material property limitations on maintaining a consistent jetting for lengthy printing durations. This would also help bridge the gap between actual printed constructs and the idealised three dimensional objects that are drawn up. An attempt at exploring the possibility of using the technology to manufacture polymeric scaffolds was made. We successfully showed that it was possible to fabricate scaffolds which can be customised to generate complicated intricate architectures with varied mechanical properties. Simultaneously, the degree of structural order can also be altered by means of simply varying the polymer concentration while keeping all other operating parameters constant. We were also able to achieve similar PCL filament line widths to those reported in

literature but at much lower concentrations of 15%. The study illustrates how the EHD printing process can be used to induce crystallization in PCL thereby enhancing the mechanical properties of the constructs created using this material. This option is non-existent in conventional printing techniques such laser lithography and extrusion based printing techniques.

## 6.2 Future work

- A study using finite elemental analysis of jet behaviour in response to changes in solution and system parameters will be required to better understand and control the features of each of the print heads
- Further parametric studies are required to better understand and compensate for gaps in the merge between electrohydrodynamic phenomena and RepRap extrusion technology. Additionally, better electronics need to be designed or faraday cage shielding needs to be implemented so that the electronics will be able to withstand the negative effects of corona discharge which disables all electrical circuitry and destroys the stepper drivers.
- The software programming code needs to be adjusted to include the effects of varying the process parameters (flow rates, voltages , standoff height, stage speed) and

solution parameters ( viscosity, electrical conductivity, concentration ,density) . This is so that the printer can detect and respond in a more timely fashion.

- A better climate control system needs to be designed and implemented to complement the portable nature of future electrohydrodynamic printers. The cooling effects of the current system is limited by the poor insulation and sealing of the printing chamber. Furthermore, its cooling was too gentle for it to have any major effect on the printing process.
- Further parametric investigations are necessary to study the effect of varying flow rate and applied voltage on the structures produced and cell studies are warranted to determine the usefulness of nasal septal constructs as effective biological supports. In particular cell work with chondrocytes or stem cells on scaffolds needs to be attempted
- Drug encapsulation within scaffolds produced through electrohydrodynamic co-axial and tri-axial printing. These processes can be used as promising techniques to fabricate multilayer structures that contain different drugs and bioactive agents in each layer, which can be released in a controlled manner where and when is necessary. A variety of structures from two dimensional drug loaded patches to three dimensional drug and cell loaded scaffolds can be prepared

- Electrohydrodynamically dispensing both polymer and drug for the development of 3D printed dosage forms in personalised medicine. The dosage forms can be studied for their drug release profiles and characterized using XRPD, IR, DSC, AFM, SEM, Hardness, Friability, Dissolution, Stability
- **Line width** and placement accuracy can be improved if replicating rapid prototyping technology can be combined with EHD drop on demand. Alternatively an attempt can be made at developing a new direct write technique that combines the strengths of laser lithography such as spot resolution and accuracy with that of electrohydrodynamic phenomena which offers flexibility and a highly quantised delivery mode for the deposition of biodegradable photopolymer.
- The printing hardware stability and resolution can be improved through the use of lead screws and stepper motors with smaller stepping angles. The printing setup will contain three lead screw driven axes ( X, Y, Z) powered by  $0.9^\circ$  Hybrid stepper motor ( Nema 23). It is anticipated that with the given lead screw pitch of (1mm) and the stepper motor stepping angle of ( $0.9^\circ$ ), the printer will have a maximum printing resolution of  $2.5\mu\text{m}$  which will be a step up from the hard ware resolution reported in previous work.
- Servo motors can be used instead of stepper motors to lend better positional accuracy. Stepper motors lack positional feedback from the machine and is therefore unable to

maintain positional control. Servo motors on the other hand have positional encoders that constantly feed information back to the motion controller system so that the power can be adjusted to ensure that the motor remains on course.

- In an effort to optimize material formulation for more consistent jetting performance, gel permeation chromatography can be carried out to determine the range of polymer chain lengths present in the dialysed silk fibroin that is produced.
- Mechanical and differential scanning calorimetry testing of electrohydrodynamically printed silk fibroin constructs/struts should be carried out to investigate if the electrohydrodynamic process has an effect on degree of crystallinity.
- X-ray diffraction studies need to be carried out on the printed polycaprolactone constructs to evaluate crystal size and orientation in the printed polycaprolactone struts.

## **REFERENCES:**

[1] R. S. Mills (1999) Recent Progress in Ink Jet Technologies II (Society for Imaging Science and Technology, Washington), 286–290

[2] Nakao H, Murakami T, Hirahara S, Nagato H, & Nomura Y, (1999) International Conference on Digital Printing Technologies (Society for Imaging Science and Technology, Washington, IS&Ts NIP15 : 319–322

[3] Choi D.H, and Lee F. C (1993), Proc. of IS&T's Ninth International Congress on Advances in Non-Impact Printing Technologies. October 4–8, Yokohama, Japan (Society for Imaging Science and Technology, Washington)

[4] Mironov V, Visconti R.P, Kasyanov V, Forgacs G, Drake C.J. and Markwald R.R (2009) “Organ printing: tissue spheroids as building blocks” *Biomaterials*. 30: 2164–74.

[5] Roth E. A, Xu T, Das M, Greory C, Hickman J.J. and Boland T(2004) “Inkjet printing for high-throughput cell patterning” *Biomaterials*, 25: 3707–15.

[6] Boland T, Xu T, Damon B and Cui X (2006) “Application of inkjet printing to tissue engineering” *Journal of Biotechnology*, 1: 910–7

[7] Mironov V, Boland T, Trusk T, Forgacs G. and Markwal R.R (2003) “Organ printing: computer-aided jet-based 3D tissue engineering”, *Trends in Biotechnology* 21: 157–61

[8] Le HP (1998) “Progress and Trends in Ink-Jet Printing Technology”. *Journal of Imaging Science and Technology* 42:49–62.

[9] K.H. Choi, K. Rahman, N.M. Muhammad, A. Khan, K.R. Kwon, Y.H. Doh, H.C. Kim, in: Bo Cui (Ed.), *Recent Advances in Nanofabrication Techniques and Applications*, 2011, pp. 548–568.

[10] A.M. Ganan Calvo, *Phys. Rev. Lett.* 79 (1997) 217–220.

[11] Calvo A. M.G (1997) “Cone-Jet Analytical Extension of Taylor's Electrostatic Solution and the Asymptotic Universal Scaling Laws in Electrospraying”, *Phys. Rev. Lett.* 79 : 217–220

[12] Zeleny J (1917) “Instability of electrified liquid surfaces”, Physical review letters. 10: 1-6

[13] Taylor G. I (1969) “Electrically Driven Jets”, Proceedings of the Royal Society A. 313: 453-475

[14] Hayati I, Bailey A.I. and Tadros T.F.J (1987) “Investigations into the mechanisms of electrohydrodynamic spraying of liquids: I. Effect of electric field and the environment on pendant drops and factors affecting the formation of stable jets and atomization”, Colloid Interface Science. 117: 205–221

[15] Zeleny J. (1914), The electrical discharge from liquids points and a hydrostatic method of measuring the electric intensities at their surfaces. Phys. Rev. E 3, 69-91.

[16] Taylor G. (1964), Disintegration of water drops in an electric field. Proc. R. Soc. A Math. Phys. Eng. Sci 280, 383-397.

[17] Jones A.R. and Thong K.C. (1971), The production of charged monodisperse fuel droplets by electrical dispersion. J. Phys. D: Appl. Phys. 4, 1159-1166.

[18] Mutoh M., Kaieda S. and Kamimura K. (1979), Convergence and disintegration of liquid jets induced by an electrostatic field. *J. Appl. Phy.* 50, 3174-3179.

[19] Nagorynti V.S. and Bezrukov V.I. (1980), Droplet emission in an electrostatic field. *Magn Gidrodin USSR* 16, 111.

[20] Smith D.P.H. (1986), The electrohydrodynamic atomization of liquids. *IEEE Trans. Industry. Appl.* IA-22, 527-535.

[21] Cloupeau M. and Prunet-Foch B. (1990), Electrostatic spraying of liquids: Main functioning modes, *J. Electrostatics* 25, 165-184.

[22] Jaworek A. and Krupa A. (1999a), Classification of the modes of EHD spraying. *J. Aerosol. Sci.* 30, 873-893.

[23] H. Choi, J. Park, O. Park, P. Ferreira, J. Georgiadis, J. Rogers, *Applied Physics Letters* 92 (2008).

[24] De la Mora JF, Loscertales IG (1994) The current emitted by highly conducting Taylor cones. *J Fluid Mech* 260: 155-184.

[25] Lee A, Jin H, Dang H, Choi K, Ahn K. 2013. Optimization of Experimental Parameters To Determine the Jetting Regimes in Electrohydrodynamic Printing. *Langmuir* 29:13630-9

[26] Lee M, Kang D, Kim N, Kim H, James S, Yoon S. 2012. A study of ejection modes for pulsed-DC electrohydrodynamic inkjet printing. *Journal of Aerosol Science* 46:1-6

[27] Jaworek A. and Krupa A. (1999a), Classification of the modes of EHD spraying. *J. Aerosol. Sci.* 30, 873-893.

[28] Hartman R.P.A., Borra J.P., Brunner D.J., Marijnissen J.C.M. and Scarlett B. (1999a), The evolution of electrohydrodynamic sprays produced in the cone-jet mode, a physical model. *J. Electrostatics*. 47, 143-170.

[29] Rulison A.J. and Flagan R.C. (1994), Electrospray atomization of electrolytic solution, *J. Colloid. Interface. Sci.* 167, 135-145.

[30] Cloupeau M. and Prunet-Foch B. (1989), Eletrostatic spraying of liquids in cone-jet mode, *J. Electrostatics* 22,135-139.

[31] Ganan-Calvo A.M., Ripoll A.B. and Rubino C.P. (1996), The equilibrium shapes of liquid menisci emitting liquid and charges in steady cone-jet mode. *J. Aerosol. Sci.* 27, S187-S188.

[32] Korkut S, Saville D.A, Aksay I.A (2008) “Enhanced Stability of Electrohydrodynamic Jets through Gas Ionization”, *Physics Review Letters*. 100: 1-4

[33] Saville D. A (1971) “Stability of electrically charged viscous cylinders” *Physics of Fluids* 14: 1095-1100

[34] Korkut S, Saville D.A, Aksay I.A (2008) “Colloidal Cluster Arrays by Electrohydrodynamic Printing” *Langmuir* 24: 12196-12201

[35] Hartman R.P.A., Brunner D.J., Camelot D.M.A., Marijnissen J.C.M. and Scarlett B. (2000), Jet break-up in electrohydrodynamic atomization in the cone-jet mode, *J. Aerosol. Sci.* 30, 823-849.

[36] Lopez-Harrera JM, Barrero A, Lopez A, Loscertales IG, Marquez M (2003) Coaxial jets generated from electrified Taylor cones, Scaling laws. *J Aerosol Sci* 34: 535-552.

[37] Tang K. and Gomez A. (1995), Generation of monodisperse water droplets from electrosprays in a corona assisted cone-jet mode. *J. Colloid. Interface. Sci.* 175, 326-332.

[38] Weber C. (1931), On the breakdown of a fluid jet. *Journal of Mechanics and Applied Mathematics* 11, 136-159.

[39] Jayasinghe S.N. and Edirisinghe M.J. (2002), Effect of viscosity on the size of relics produced by electrostatic atomization. *J. Aerosol. Sci.* 33, 1379-1388.

[40] Grace J.M. and Marijnissen J.C.M. (1994), A review of liquid atomization by electrical means. *J. Aerosol. Sci.* 25, 1005-1019.

[41] Higuera, F. J. (2003) Flow rate and electric current emitted by a Taylor cone. *Journal of Fluid Mechanics*, 484, 303-327.

[42] Kwon K, Lee D. 2013. Investigation of pulse voltage shape effects on electrohydrodynamic jets using a vision measurement technique. *Journal of Micromechanics and Microengineering* 23

[43] Li J. (2006) On the meniscus deformation when the pulsed voltage is applied. *Journal of Electrostatics* 64:44-52

[44] Li J. (2007) On the stability of electrohydrodynamic spraying in the cone-jet mode. *Journal of Electrostatics* 65:251-5

[45] Son S, An K, Kim Y.J, Choi J, Lee S (2010) Study of the phenomenon of meniscus deformation and ejection by pulse voltage and frequency in drop on demand EHD printing. *NSTI-NANOTECH ISBN 978-1-4398-3402-2 VOL.2*

[46] Kang D, Lee M, Kim H, James S, Yoon S. 2011. Electrohydrodynamic pulsed-inkjet characteristics of various inks containing aluminum particles. *Journal of Aerosol Science* 42:621-30

[47] Kim J, Oh H, Kim S. 2008. Electrohydrodynamic drop-on-demand patterning in pulsed cone-jet mode at various frequencies. *Journal of Aerosol Science* 39:819-25

[48] Barton K, Mishra S, Shorter K, Alleyne A, Ferreira P, Rogers J. 2010. A desktop electrohydrodynamic jet printing system. *Mechatronics* 20:611-6

[49] Sutanto E, Shigeta K, Kim Y, Graf P, Hoelzle D, et al. 2012. A multimaterial electrohydrodynamic jet (E-jet) printing system. *Journal of Micromechanics and Microengineering* 22

[50] Wang H, Li M, Chen X, Zheng J, Chen X, Zhu Z. 2015. Study of deposition characteristics of multi-nozzle near-field electrospinning in electric field crossover interference conditions. *Aip Advances* 5

[51] Wang H, Li M, Huang S, Zheng J, Chen X, et al. 2015. Deposition characteristics of the double nozzles near-field electrospinning. *Applied Physics a-Materials Science & Processing* 118:621-8

[52] Wei C, Qin H, Ramirez-Iglesias N, Chiu C, Lee Y, Dong J. 2014. High-resolution ac-pulse modulated electrohydrodynamic jet printing on highly insulating substrates. *Journal of Micromechanics and Microengineering* 24

[53] Hashimdeen SH, Miodownik M, Edirisinghe MJ. 2014. The Design and Construction of an Electrohydrodynamic Cartesian Robot for the Preparation of Tissue Engineering Constructs. *PLoS ONE* 9:e112166

[54] Park J, Lee J, Paik U, Lu Y, Rogers J. 2008. Nanoscale Patterns of Oligonucleotides Formed by Electrohydrodynamic Jet Printing with Applications in Biosensing and Nanomaterials Assembly. *Nano Letters* 8:4210-6

[55] Elele E, Shen Y, Susarla R, Khusid B, Keyvan G, Michniak-Kohn B. 2012. Electrodeless Electrohydrodynamic Drop-on-Demand Encapsulation of Drugs into Porous Polymer Films for Fabrication of Personalized Dosage Units. *Journal of Pharmaceutical Sciences* 101:2523-33

[56] Hwang T, Kim J, Yang D, Park Y, Ryu W. 2013. Targeted electrohydrodynamic printing for micro-reservoir drug delivery systems. *Journal of Micromechanics and Microengineering* 23

[57] Rahman K, Khan A, Nam N, Choi K, Kim D. 2011. Study of Drop-on-Demand Printing Through Multi-Step Pulse Voltage. *International Journal of Precision Engineering and Manufacturing* 12:663-9

[58] Galliker P, Schneider J, Eghlidi H, Kress S, Sandoghdar V, Poulikakos D. 2012. Direct printing of nanostructures by electrostatic autofocussing of ink nanodroplets. *Nature Communications* 3

[59] Onses M, Song C, Williamson L, Sutanto E, Ferreira P, et al. 2013. Hierarchical patterns of three-dimensional block-copolymer films formed by electrohydrodynamic jet printing and self-assembly. *Nature Nanotechnology* 8:667-75

[60] Shigeta K, He Y, Sutanto E, Kang S, Le A, et al. 2012. Functional Protein Microarrays by Electrohydrodynamic Jet Printing. *Analytical Chemistry* 84:10012-8

[61] Jang Y, Kim J, Byun D. 2013. Invisible metal-grid transparent electrode prepared by electrohydrodynamic (EHD) jet printing. *Journal of Physics D-Applied Physics* 46

[62] Jeong Y, Lee H, Lee B, Park S, Yudistira H, et al. 2014. Directly Drawn Poly(3-hexylthiophene) Field-Effect Transistors by Electrohydrodynamic Jet Printing: Improving Performance with Surface Modification. *Acs Applied Materials & Interfaces* 6:10736-43

[63] Kim Y, Kim S, Hwang J. 2013. Drop-on-demand hybrid printing using a piezoelectric MEMS printhead at various waveforms, high voltages and jetting frequencies. *Journal of Micromechanics and Microengineering* 23

[64] Lee S, An K, Son S, Choi J. 2013. Satellite/spray suppression in electrohydrodynamic printing with a gated head. *Applied Physics Letters* 103

[65] Lee D, Yu J, Shin Y, Park D, Yu T, Hwang J. 2008. Formation of ceramic nanoparticle patterns using electrohydrodynamic jet printing with pin-to-pin electrodes. *Japanese Journal of Applied Physics* 47:1723-5

[66] Xu L, Sun D. 2013. Electrohydrodynamic printing under applied pole-type nozzle configuration. *Applied Physics Letters* 102

[67] Chen C, Saville D, Aksay I. 2006. Electrohydrodynamic "drop-and-place" particle deployment. *Applied Physics Letters* 88

[68] Lee J, Jeong Y, Cho D. 2014. Fabrication of Nanofibrous Mats with Uniform Thickness and Fiber Density. *Macromolecular Materials and Engineering* 299:1052-61

[69] Bisht G, Nesterenko S, Kulinsky L, Madou M. 2012. A Computer-Controlled Near-Field Electrospinning Setup and Its Graphic User Interface for Precision Patterning of Functional Nanofibers on 2D and 3D Substrates. *Journal of Laboratory Automation* 17:302-8

[70] Lee J, Kim S, Kim Y, Park J, Kim Y, Hwang J. 2008. Design and evaluation of a silicon based multi-nozzle for addressable jetting using a controlled flow rate in electrohydrodynamic jet printing. *Applied Physics Letters* 93

[71] Pan Y, Huang Y, Guo L, Ding Y, Yin Z. 2015. Addressable multi-nozzle electrohydrodynamic jet printing with high consistency by multi-level voltage method. *Aip Advances* 5

[72] Lee J, Kim Y, Kang B, Kim S, Park J, Hwang J. 2009. ELECTROHYDRODYNAMIC JET PRINTING CAPABLE OF REMOVING SUBSTRATE EFFECTS AND MODULATING PRINTING CHARACTERISTICS. *Ieee 22nd International Conference on Micro Electro Mechanical Systems (Mems 2009)*:487-90

[73] Hashimdeen S, Miodownik M, Edirisinghe M. 2013. Print head design and control for electrohydrodynamic printing of silk fibroin. *Materials Science & Engineering C-Materials For Biological Applications* 33:3309-18

[74] Park J, Hardy M, Kang S, Barton K, Adair K, et al. 2007. High-resolution electrohydrodynamic jet printing. *Nature Materials* 6:782-9

[75] Schirmer NC, Kullmann C, Schmid MS, Burg BR, Schwamb T, Poulikakos D. 2010. On Ejecting Colloids Against Capillarity from Sub-micrometer Openings: On-Demand Dielectrophoretic Nanoprinting. *Advanced Materials* 22:4701-5

[76] Li X, Huang J, Edirisinghe M, Bonfield W. 2011. An electrically driven jetting technique for diverse high-resolution surface structures of nanometre hydroxyapatite crystals. *Colloids and Surfaces B: Biointerfaces* 82:562-70

[77] L. Wang, Y. Qiu, Y. Pei, Y. Su, Z. Zhan, W. Lv, D. Sun Proc. IMechE Part N: J. Nanoeng. Nanosyst., 225 (2012), pp. 85–88

[78] Park S, Lee D, Kim S, Shin Y, Yu T, et al. 2009. Design of Electrohydrodynamic Lens for Stabilizing of Eletrohydrodynamic Jet Printing. *Electrostatics* 2007 142

[79] Lee J-G, Cho H-J, Huh N, Ko C, Lee W-C, et al. 2006. Electrohydrodynamic (EHD) dispensing of nanoliter DNA droplets for microarrays. *Biosensors and Bioelectronics* 21:2240-7

[80] Zheng J, Liu H, Wang X, Zhao Y, Huang W, et al. 2014. Electrohydrodynamic Direct-Write Orderly Micro/Nanofibrous Structure on Flexible Insulating Substrate. *Journal of Nanomaterials*

[81] Zheng G, Liu H, Xu R, Wang X, Liu J, et al. 2014. Alternating Current Electrohydrodynamic Printing of Microdroplets. *Journal of Nanomaterials*

[82] Ferraro P, Coppola S, Grilli S, Paturzo M, Vespi V. 2010. Dispensing nano-pico droplets and liquid patterning by pyroelectrodynamic shooting. *Nat Nano* 5:429-35

[83] Park J-U, Lee S, Unarunotai S, Sun Y, Dunham S, et al. 2010. Nanoscale, Electrified Liquid Jets for High-Resolution Printing of Charge. *Nano Letters* 10:584-91

[84] Rogers J, Paik U. 2010. NANOFABRICATION Nanoscale printing simplified. *Nature Nanotechnology* 5:385-6

[85] Coppola S, Grimaldi I, Loffredo F, Villani F, Nenna G, et al. 2014. Printing on demand of polymer micro lenses array. *Micro-Optics* 2014 9130

[86] Coppola S, Vespi V, Grimaldi I, Loffredo F, Villani F, et al. 2012. Fabrication of optical microlenses by a new inkjet printing technique based on pyro-electrohydrodynamic (PEHD) effect. *Micro-Optics* 2012 8428

[87] Grimaldi I, Coppola S, Loffredo F, Villani F, Minarini C, et al. 2012. Printing of polymer microlenses by a pyroelectrohydrodynamic dispensing approach. *Optics Letters* 37:2460-2

[88] Grimaldi I, Coppola S, Loffredo F, Villani F, Nenna G, et al. 2013. Graded-size microlens array by the pyro-electrohydrodynamic continuous printing method. *Applied Optics* 52:7699-705

[89] Coppola S, Vespi V, Grilli S, Ferraro P. 2011. Self-assembling of multi-jets by pyro-electrohydrodynamic effect for high throughput liquid nanodrops transfer. *Lab on a Chip* 11:3294-8

[90] Coppola S, Vespi V, Nasti G, Gennari O, Grilli S, et al. 2014. Tethered Pyro-Electrohydrodynamic Spinning for Patterning Well-Ordered Structures at Micro- and Nanoscale. *Chemistry of Materials* 26:3357-60

[91] Byun S, Park H, Lee K, Lim B, Lee H, Seo D. 2012. Application of Electrohydrodynamic Printing for Liquid Crystal Alignment. *Electrochemical and Solid State Letters* 15:J28-J30

[92] Ahmad Z, Rasekh M, Edirisinghe M. 2010. Electrohydrodynamic Direct Writing of Biomedical Polymers and Composites. *Macromolecular Materials and Engineering* 295:315-9

[93] Bayram C, Ahmad Z, Denkbas E, Stride E, Edirisinghe M. 2013. Electrohydrodynamic Printing of Silk Fibroin. *Macromolecular Research* 21:339-42

[94] Kim J, Lee D, Hwang J, Jung H. 2009. Direct pattern formation of bacterial cells using micro-droplets generated by electrohydrodynamic forces. *Microfluidics and Nanofluidics* 7:829-39

[95] Kim H, Lee D, Park J, Kim J, Hwang J, Jung H. 2007. Optimization of electrohydrodynamic writing technique to print collagen. *Experimental Techniques* 31:15-9

[96] Poellmann M, Barton K, Mishra S, Johnson A. 2011. Patterned Hydrogel Substrates for Cell Culture with Electrohydrodynamic Jet Printing. *Macromolecular Bioscience* 11:1164-8

[97] Poon H, Saville D, Aksay I. 2008. Linear colloidal crystal arrays by electrohydrodynamic printing. *Applied Physics Letters* 93

[98] Onses M, Ramirez-Hernandez A, Hur S, Sutanto E, Williamson L, et al. 2014. Block Copolymer Assembly on Nanoscale Patterns of Polymer Brushes Formed by Electrohydrodynamic Jet Printing. *Acs Nano* 8:6606-13

[99] Cai Y, Li J, Poh C, Tan H, Thian E, et al. 2013. Collagen grafted 3D polycaprolactone scaffolds for enhanced cartilage regeneration. *Journal of Materials Chemistry B* 1:5971-6

[100] Li JL, Cai YL, Guo YL, Fuh JYH, Sun J, et al. 2014. Fabrication of three-dimensional porous scaffolds with controlled filament orientation and large pore size via an improved E-jetting technique. *Journal of Biomedical Materials Research Part B: Applied Biomaterials* 102:651-8

[101] Ahn S, Lee H, Kim G. 2011. Polycaprolactone Scaffolds Fabricated with an Advanced Electrohydrodynamic Direct-Printing Method for Bone Tissue Regeneration. *Biomacromolecules* 12:4256-63

[102] Kim M, Kim G. 2014. Electrohydrodynamic Jet Process for Pore-Structure-Controlled 3D Fibrous Architecture As a Tissue Regenerative Material: Fabrication and Cellular Activities. *Langmuir* 30:8551-7

[103] Kim M, Kim GH. 2015. Electrohydrodynamic direct printing of PCL/collagen fibrous scaffolds with a core/shell structure for tissue engineering applications. *Chemical Engineering Journal* 279:317-26

[104] Kim G, Ahn S, Lee H, Lee S, Cho Y, Chun W. 2011. A new hybrid scaffold using rapid prototyping and electrohydrodynamic direct writing for bone tissue regeneration. *Journal of Materials Chemistry* 21:19138-43

[105] Yang G-H, Kim M, Kim G. 2015. A hybrid PCL/collagen scaffold consisting of solid freeform-fabricated struts and EHD-direct-jet-processed fibrous threads for tissue regeneration. *Journal of Colloid and Interface Science* 450:159-67

[106] Rasekh M, Ahmad Z, Day R, Wickham A, Edirisinghe M. 2011. Direct Writing of Polycaprolactone Polymer for Potential Biomedical Engineering Applications. *Advanced Engineering Materials* 13:B296-B305

[107] Rasekh M, Ahmad Z, Frangos C, Bozec L, Edirisinghe M, Day R. 2013. Spatial and temporal evaluation of cell attachment to printed polycaprolactone microfibres. *Acta Biomaterialia* 9:5052-62

[108] Gupta A, Seifalian A, Ahmad Z, Edirisinghe M, Winslet M. 2007. Novel electrohydrodynamic printing of nanocomposite biopolymer scaffolds. *Journal of Bioactive and Compatible Polymers* 22:265-80

[109] Wang K, Paine M, Stark J. 2009. Fully voltage-controlled electrohydrodynamic jet printing of conductive silver tracks with a sub-100 $\mu$ m linewidth. *Journal of Applied Physics*

[110] Youn D, Kim S, Yang Y, Lim S, Kim S, et al. 2009. Electrohydrodynamic micropatterning of silver ink using near-field electrohydrodynamic jet printing with tilted-outlet nozzle. *Applied Physics a-Materials Science & Processing* 96:933-8

[111] Lee D, Lim D, Kim Y, Hwang J. 2009. Electrical Characterization of a Microstrip Line Patterned by Electrohydrodynamic Jet Printing of Silver Nanoparticles. *Journal of Imaging Science and Technology* 53

[112] Rahman K, Khan A, Muhammad N, Jo J, Choi K. 2012. Fine-resolution patterning of copper nanoparticles through electrohydrodynamic jet printing. *Journal of Micromechanics and Microengineering* 22

[113] Kim D, Rahman K, Khan A, Choi K. 2012. Direct Fabrication of Copper Nanoparticle Patterns through Electrohydrodynamic Printing in Cone-Jet Mode. *Materials and Manufacturing Processes* 27:1295-9

[114] Lee D, Lee J, Shin Y, Park S, Yu T, et al. 2009. Structuring of Conductive Silver Line by Electrohydrodynamic Jet Printing and Its Electrical Characterization. *Electrostatics* 2007 142

[115] Son S, Lee S, Choi J. 2014. Fine metal line patterning on hydrophilic non-conductive substrates based on electrohydrodynamic printing and laser sintering. *Journal of Electrostatics* 72:70-5

[116] Lee H, Seong B, Kim J, Jang Y, Byun D. 2014. Direct Alignment and Patterning of Silver Nanowires by Electrohydrodynamic Jet Printing. *Small* 10:3918-22

[117] Kang J, Jang Y, Kim Y, Cho S, Suhr J, et al. 2015. An Ag-grid/graphene hybrid structure for large-scale, transparent, flexible heaters. *Nanoscale* 7:6567-73

[118] Pan C, Yang T, Chen Y, Su C, Ju S, et al. 2015. Fibers and Conductive Films Using Silver Nanoparticles and Nanowires by Near-Field Electrospinning Process. *Journal of Nanomaterials*

[119] Wang K, Paine M, Stark J. 2009. Freeform fabrication of metallic patterns by unforced electrohydrodynamic jet printing of organic silver ink. *Journal of Materials Science-Materials in Electronics* 20:1154-7

[120] Wang K, Stark J. 2010. Direct fabrication of electrically functional microstructures by fully voltage-controlled electrohydrodynamic jet printing of silver nano-ink. *Applied Physics a-Materials Science & Processing* 99:763-6

[121] Wang K, Paine M, Stark J. 2010. Novel electrohydrodynamic jet-printing of organic silver ink in unforced form. *Optoelectronics and Advanced Materials-Rapid Communications* 4:365-8

[122] Yu J, Kim S, Hwang J. 2007. Effect of viscosity of silver nanoparticle suspension on conductive line patterned by electrohydrodynamic jet printing. *Applied Physics a-Materials Science & Processing* 89:157-9

[123] Choi J, Kim Y, Lee S, Son S, Ko H, et al. 2008. Drop-on-demand printing of conductive ink by electrostatic field induced inkjet head. *Applied Physics Letters* 93

[124] Choi K, Zubair M, Dang H. 2014. Characterization of flexible temperature sensor fabricated through drop-on-demand electrohydrodynamics patterning. *Japanese Journal of Applied Physics* 53

[125] Wang K, Stark J. 2010. Deposition of colloidal gold nanoparticles by fully pulsed-voltage-controlled electrohydrodynamic atomisation. *Journal of Nanoparticle Research* 12:707-11

[126] Corbin E, Millet L, Pikul J, Johnson C, Georgiadis J, et al. 2013. Micromechanical properties of hydrogels measured with MEMS resonant sensors. *Biomedical Microdevices* 15:311-9

[127] Rahman K, Ali K, Muhammad N, Hyun M, Choi K. 2013. Fine resolution drop-on-demand electrohydrodynamic patterning of conductive silver tracks on glass substrate. *Applied Physics a-Materials Science & Processing* 111:593-600

[128] Prasetyo F, Yudistira H, Nguyen V, Byun D. 2013. Ag dot morphologies printed using electrohydrodynamic (EHD) jet printing based on a drop-on-demand (DOD) operation. *Journal of Micromechanics and Microengineering* 23

[129] Wang X, Xu L, Zheng G, Cheng W, Sun D. 2012. Pulsed electrohydrodynamic printing of conductive silver patterns on demand. *Science China-Technological Sciences* 55:1603-7

[130] Wang K, Stark J. 2010. Voltage effects on the nanoelectrospray characteristics in fully voltage-controlled atomisation of gold nanocolloids. *Analytica Chimica Acta* 679:81-4

[131] Samarasinghe S, Pastoriza-Santos I, Edirisinghe M, Reece M, Liz-Marzan L. 2006. Printing gold nanoparticles with an electrohydrodynamic direct-write device. *Gold Bulletin* 39:48-53

[132] Samarasinghe S, Edirisinghe M. 2008. Synthesis, processing and forming gold structures from a 0.1 wt. % concentration solution. *Gold Bulletin* 41:284-95

[133] Han Y, Wei C, Dong J. 2014. Super-resolution electrohydrodynamic (EHD) 3D printing of micro-structures using phase-change inks. *Manufacturing Letters* 2:96-9

[134] Wang D, Edirisinghe M, Jayasinghe S. 2006. Solid freeform fabrication of thin-walled ceramic structures using an electrohydrodynamic jet. *Journal of the American Ceramic Society* 89:1727-9

[135] Wang D, Duan H, Li J, Liang J, Liu C. 2011. Electrohydrodynamic atomization deposition and patterning of a carbon nano-suspension. *Proceedings of the Institution of Mechanical Engineers, Part N: Journal of Nanoengineering and Nanosystems* 225:149-54

[136] Wang D, Jayasinghe S, Edirisinghe M. 2005. High resolution print-patterning of a nano-suspension. *Journal of Nanoparticle Research* 7:301-6

[137] Ahmad Z, Thian E, Huang J, Edirisinghe M, Best S, et al. 2008. Deposition of nano-hydroxyapatite particles utilising direct and transitional electrohydrodynamic processes. *Journal of Materials Science-Materials in Medicine* 19:3093-104

[138] Ahmad Z, Nangrejo M, Rasekh M, Stride E, Edirisinghe M. 2013. Novel electrically driven direct-writing methods with managed control on in-situ shape and encapsulation polymer forming. International Journal of Material Forming 6:281-8

[139] Vishwanath S, Kim D, Kim J. 2014. Electromagnetic interference shielding effectiveness of invisible metal-mesh prepared by electrohydrodynamic jet printing. Japanese Journal of Applied Physics 53

[140] Jeong J, Kim H, Kim J. 2014. Invisible Ag grid embedded with ITO nanoparticle layer as a transparent hybrid electrode. Solar Energy Materials and Solar Cells 125:113-9

[141] Shin D, Seo J, Tak H, Byun D. 2015. Bimodally dispersed silver paste for the metallization of a crystalline silicon solar cell using electrohydrodynamic jet printing. Solar Energy Materials and Solar Cells 136:148-56

[142] Wang X, Zheng G, He G, Wei J, Liu H, et al. 2013. Electrohydrodynamic direct-writing ZnO nanofibers for device applications. Materials Letters 109:58-61

[143] Chang J, Liu Y, Kwang H, Lee B, Lee S, Lin L. 2013. DIRECT-WRITE N- AND P-TYPE GRAPHENE CHANNEL FETS. 26th Ieee International Conference on Micro Electro Mechanical Systems (Mems 2013):201-4

[144] Lee Y, Kim T, Min S, Xu W, Jeong S, et al. 2014. Individually Position-Addressable Metal-Nanofiber Electrodes for Large-Area Electronics. *Advanced Materials* 26:8010

[145] Hwang S, Min S, Bae I, Cho S, Kim K, et al. 2014. Non-Volatile Ferroelectric Memory with Position-Addressable Polymer Semiconducting Nanowire. *Small* 10:1976-84

[146] Song C, Rogers J, Kim J, Ahn H. 2015. Patterned Polydiacetylene-Embedded Polystyrene Nanofibers Based on Electrohydrodynamic Jet Printing. *Macromolecular Research* 23:118-23

[147] Tan Y, Sutanto E, Alleyne A, Cunningham B. 2014. Photonic crystal enhancement of a homogeneous fluorescent assay using submicron fluid channels fabricated by E-jet patterning. *Journal of Biophotonics* 7:266-75

[148] Poellmann M, Barton K, Mishra S, Johnson A. 2011. Patterned Hydrogel Substrates for Cell Culture with Electrohydrodynamic Jet Printing. *Macromolecular Bioscience* 11:1164-8

[149] Poon H, Saville D, Aksay I. 2008. Linear colloidal crystal arrays by electrohydrodynamic printing. *Applied Physics Letters* 93

[150] Zheng G, Pei Y, Wang X, Zheng J, Sun D. 2014. Electrohydrodynamic direct-writing of conductor-insulator-conductor multi-layer interconnection. *Chinese Physics B* 23

[151] Choi K, Mustafa M, Rahman K, Jeong B, Doh Y. 2012. Cost-effective fabrication of memristive devices with ZnO thin film using printed electronics technologies. *Applied Physics a-Materials Science & Processing* 106:165-70

[152] Choi K, Duraisamy N, Awais M, Muhammad N, Kim H, Jo J. 2013. Investigation on switching behavior of ZrO<sub>2</sub> thin film for memory device applications. *Materials Science in Semiconductor Processing* 16:1285-91

[153] Awais M, Kim H, Doh Y, Choi K. 2013. ZrO<sub>2</sub> flexible printed resistive (memristive) switch through electrohydrodynamic printing process. *Thin Solid Films* 536:308-12

[154] Choi K, Awais M. 2012. Versatile resistive switching (memristive) behavior in an ITO/ZRO(2)/AG sandwich fabricated using electrohydrodynamic printing. *Journal of the Korean Physical Society* 61:119-23

[155] Duraisamy N, Muhammad N, Kim H, Jo J, Choi K. 2012. Fabrication of TiO<sub>2</sub> thin film memristor device using electrohydrodynamic inkjet printing. *Thin Solid Films* 520:5070-4

[156] Khan S, Doh Y, Khan A, Rahman A, Choi K, Kim D. 2011. Direct patterning and electrospray deposition through EHD for fabrication of printed thin film transistors. *Current Applied Physics* 11:S271-S9

[157] Lee YG, Choi W-S. 2014. Electrohydrodynamic Jet-Printed Zinc–Tin Oxide TFTs and Their Bias Stability. *ACS Applied Materials & Interfaces* 6:11167-72

[158] Lee S, Kim J, Choi J, Park H, Ha J, et al. 2012. Patterned oxide semiconductor by electrohydrodynamic jet printing for transparent thin film transistors. *Applied Physics Letters* 100

[159] Kwon J, Hong S, Suh YD, Yeo J, So H-M, et al. 2015. Direct Micro Metal Patterning on Plastic Substrates by Electrohydrodynamic Jet Printing for Flexible Electronic Applications. *ECS Journal of Solid State Science and Technology* 4:P3052-P6

[160] Zheng G, Yu Z, Zhuang M, Wei W, Zhao Y, et al. 2014. Electrohydrodynamic direct-writing of three-dimensional multi-loop nanofibrous coils. *Applied Physics a-Materials Science & Processing* 116:171-7

[161] Yudistira H, Tenggara A, Nguyen V, Kim T, Prasetyo F, et al. 2013. Fabrication of terahertz metamaterial with high refractive index using high-resolution electrohydrodynamic jet printing. *Applied Physics Letters* 103

[162] Park H, Byun S, Jeong H, Lee J, Seo D. 2013. Photoreactive Spacer Prepared Using Electrohydrodynamic Printing for Application in a Liquid Crystal Device. *Ecs Solid State Letters* 2:R52-R4

[163] Fuh Y, Chen P, Huang Z, Ho H. 2015. Self-powered sensing elements based on direct-write, highly flexible piezoelectric polymeric nano/microfibers. *Nano Energy* 11:671-7

[164] Pan C, Yen C, Liu Z, Li H, Kuo S, et al. 2014. Poly(gamma-benzyl alpha, l-glutamate) in Cylindrical Near-Field Electrospinning Fabrication and Analysis of Piezoelectric Fibers. *Sensors and Materials* 26:63-73

[165] Chen D, Guo X, Wang Z, Wang P, Chen Y, Lin L. 2011. Polyaniline nanofiber gas sensors by direct-write electrospinning. 2011 *Ieee 24th International Conference on Micro Electro Mechanical Systems (Mems)*:1369-72

[166] Di Camillo D, Fasano V, Ruggieri F, Santucci S, Lozzi L, et al. 2013. Near-field electrospinning of light-emitting conjugated polymer nanofibers. *Nanoscale* 5:11637-42

[167] Yang T, Pan C, Chen Y, Lin L, Wu I, et al. 2015. Synthesis and fabrication of silver nanowires embedded in PVP fibers by near-field electrospinning process. *Optical Materials* 39:118-24

[168] Lei T, Lu X, Yang F. 2015. Fabrication of various micro/nano structures by modified near-field electrospinning. *Aip Advances* 5

[169] Biagi G, Holmgard T, Skovsen E. 2013. Near-field electrospinning of dielectric-loaded surface plasmon polariton waveguides. *Optics Express* 21:4355-60

[170] Lameiro R, Sencadas V, Lanceros-Mendez S, Correia J, Mendes P, et al. 2011. Large Area Microfabrication of Electroactive Polymeric Structures Based on Near-Field Electrospinning. *Eurosensors Xxv* 25

[171] Liu Z, Pan C, Lin L, Lai H. 2013. Piezoelectric properties of PVDF/MWCNT nanofiber using near-field electrospinning. *Sensors and Actuators a-Physical* 193:13-24

[172] Rinaldi M, Ruggieri F, Lozzi L, Santucci S. 2009. Well-aligned TiO(2) nanofibers grown by near-field-electrospinning. *Journal of Vacuum Science & Technology B* 27:1829-33

[173] Ruggieri F, Di Camillo D, Lozzi L, Santucci S, De Marcellis A, et al. 2013. Preparation of nitrogen doped TiO<sub>2</sub> nanofibers by near field electrospinning (NFES) technique for NO<sub>2</sub> sensing. *Sensors and Actuators B-Chemical* 179:107-13

[174] Duan Y, Huang Y, Yin Z, Bu N, Dong W. 2014. Non-wrinkled, highly stretchable piezoelectric devices by electrohydrodynamic direct-writing. *Nanoscale* 6:3289-95

[175] Huang Y, Duan Y, Ding Y, Bu N, Pan Y, et al. 2014. Versatile, kinetically controlled, high precision electrohydrodynamic writing of micro/nanofibers. *Scientific Reports* 4

[176] Bajaj B, Yoon S, Park B, Lee J. 2012. Coiled Fibers of Poly (Amide-Co-Imide) PAI and Poly (Trimellitic Anhydride Chloride-Co-4, 4'-Methylene Dianiline) (PTACM) By Using Mechano-Electrospinning. *Journal of Engineered Fibers and Fabrics* 7:37-41

[177] Bajaj B, Kim B, Yoon S, Lee J, Park B. 2014. One-Step Continuous Coating of Silver Nanoparticles on Well Aligned Fibers of PAI/PTACM. *Fibers and Polymers* 15:47-56

[178] Hochleitner G, Hümmer JF, Luxenhofer R, Groll J. 2014. High definition fibrous poly(2-ethyl-2-oxazoline) scaffolds through melt electrospinning writing. *Polymer* 55:5017-23

[179] Brown T, Dalton P, Hutmacher D. 2011. Direct Writing By Way of Melt Electrospinning. *Advanced Materials* 23:5651

[180] Wei C, Dong J. 2013. Direct fabrication of high-resolution three-dimensional polymeric scaffolds using electrohydrodynamic hot jet plotting. *Journal of Micromechanics and Microengineering* 23

[181] Brown T, Slotosch A, Thibaudeau L, Taubenberger A, Loessner D, et al. 2012. Design and Fabrication of Tubular Scaffolds via Direct Writing in a Melt Electrospinning Mode. *Biointerphases* 7

[182] Farrugia B, Brown T, Upton Z, Hutmacher D, Dalton P, Dargaville T. 2013. Dermal fibroblast infiltration of poly(epsilon-caprolactone) scaffolds fabricated by melt electrospinning in a direct writing mode. *Biofabrication* 5

[183] Brown T, Edin F, Detta N, Skelton A, Hutmacher D, Dalton P. 2014. Melt electrospinning of poly(epsilon-caprolactone) scaffolds: Phenomenological observations associated with collection and direct writing. *Materials Science & Engineering C-Materials For Biological Applications* 45:698-708

[184] Wei C, Dong J. 2014. Hybrid hierarchical fabrication of three-dimensional scaffolds. Journal of Manufacturing Processes 16:257-63

[185] Bu N, Huang Y, Duan Y, Ding Y, Yin Z. 2015. Near-field behavior of electrified jet under moving substrate constrains. Aip Advances 5

[186] Pikul J, Graf P, Mishra S, Barton K, Kim Y, et al. 2011. High Precision Electrohydrodynamic Printing of Polymer Onto Microcantilever Sensors. Ieee Sensors Journal 11:2246-53

[187] Griffith L, Sipe J, Kelley C, McNicol L. 2002. Emerging design principles in Biomaterials and scaffolds for tissue engineering. Reparative Medicine: Growing Tissues and Organs 961:83-95

[188] Vogel V, Baneyx G. 2003. THE TISSUE ENGINEERING PUZZLE: A Molecular Perspective. Annual Review of Biomedical Engineering 5:441-63

[189] Siebers M, ter Brugge P, Walboomers X, Jansen J. 2005. Integrins as linker proteins between osteoblasts and bone replacing materials. A critical review. Biomaterials 26:137-46

[190] Scneider G, Burridge K. 1994. Formation of focal adhesions by osteoblasts adhering to different substrata. *Experimental Cell Research* 214:264-9

[191] McFarland C, Mayer S, Scotchford C, Dalton B, Steele J, Downes S. 1999. Attachment of cultured human bone cells to novel polymers. *Journal of Biomedical Materials Research* 44:1-11

[192] Anselme K. 2000. Osteoblast adhesion on biomaterials. *Biomaterials* 21:667-81

[193] Hirsch M, Lunsford L, Trinkaus-Randall V, Svoboda K. 1997. Chondrocyte survival and differentiation in situ are integrin mediated. *Developmental Dynamics* 210:249-63

[194] Kaazempur Mofrad MR, Abdul-Rahim NA, Karcher H, Mack PJ, Yap B, Kamm RD. 2005. Exploring the molecular basis for mechanosensation, signal transduction, and cytoskeletal remodeling. *Acta Biomaterialia* 1:281-93

[195] Sipe J, Kelley C, McNicol L. 2002. Tissue engineering and reparative medicine. *Reparative Medicine: Growing Tissues and Organs* 961:1-9

[196] Nam Y, Yoon J, Park T. 2000. A novel fabrication method of macroporous biodegradable polymer scaffolds using gas foaming salt as a porogen additive. *Journal of Biomedical Materials Research*, 53: 1-7

[197] Yoon J. 2003. Dexamethasone-releasing biodegradable polymer scaffolds fabricated by a gas-foaming/salt-leaching method. *Biomaterials*, 24:2323-2329

[198] Yeong W, Chua C, Leong K, Chandrasekaran M. 2004. Rapid prototyping in tissue engineering: challenges and potential. *Trends in Biotechnology*, 22: 643-52

[199] Tellis B, Szivek J, Bliss C, Margolis D, Vaidyanathan R, Calvert P. 2008. Trabecular scaffolds created using micro CT guided fused deposition modeling. *Materials Science & Engineering C-Biomimetic and Supramolecular Systems* 28:171–178.

[200] Hutmacher D, Sittlinger M, Risbud M. 2004. Scaffold-based tissue engineering: rationale for computer-aided design and solid free-form fabrication systems. *Trends in Biotechnology* 22:354–362.

[201] Ovsianikov A, Malinauskas M, Schlie S, Chichkov B, Gittard S, Narayan R, Lobler M, Sternberg K, Schmitz KP and Haverich A. 2011. Three-dimensional laser micro- and nano-

structuring of acrylated poly(ethylene glycol) materials and evaluation of their cytotoxicity for tissue engineering applications. *Acta Biomaterialia* 7:967–974.

[202] Pirlo R, Wu P, Liu J, Ringeisen B. 2012. PLGA/hydrogel biopapers as a stackable substrate for printing HUVEC networks via BioLP (TM). *Biotechnology and Bioengineering* 109:262–273

[203] Wüst S, Müller R, Hofmann S. 2011. Controlled positioning of cells in bio-materials – approaches towards 3D tissue printing. *Journal of Functional Biomaterials* 2:119–154.

[204] Boland T, Xu T, Damon B and Cui X. 2006. Application of inkjet printing to tissue engineering. *Biotechnology Journal* 1:910–917.

[205] Vepari C, Kaplan D. 2007. Silk as a biomaterial. *Progress in Polymer Science*. 32: 991–1007

[206] Jin, H, Kaplan D. 2003. Mechanism of silk processing in insects and spiders. *Nature*, 424, 1057–1061.

[207] L.G. Griffith. Polymeric biomaterials, *Acta Materialia* 48 (2000) 263-277.

[208] Sun H, Mei L, Song C, Cui X, Wang P. 2006. The in vivo degradation, absorption and excretion of PCL-based implant. *Biomaterials* 27:1735-40

[209] Pankajakshan D, Agrawal D. 2010. Scaffolds in tissue engineering of blood vessels. *Canadian Journal of Physiology and Pharmacology* 88:855-73

[210] Zhou F, Hubbard P, Eichhorn S, Parker G. 2011. Jet deposition in near-field electrospinning of patterned polycaprolactone and sugar-polycaprolactone core–shell fibres. *Polymer* 52:3603-10

[211] Pham Q, Sharma U, Mikos A. 2006. Electrospun poly(epsilon-caprolactone) microfiber and multilayer nanofiber/microfiber scaffolds: Characterization of scaffolds and measurement of cellular infiltration. *Biomacromolecules* 7:2796-805

[212] Zhang Y, Wang X, Feng Y, Li J, Lim C, Ramakrishna S. 2006. Coaxial electrospinning of (fluorescein isothiocyanate-conjugated bovine serum albumin)-encapsulated poly(epsilon-caprolactone) nanofibers for sustained release. *Biomacromolecules* 7:1049-57

[213] Gibson HW. 1969. Chemistry of formic acid and its simple derivatives. *Chemical Reviews* 69:673-92

[214] Tundo P, Selva M. 2002. The Chemistry of Dimethyl Carbonate. *Accounts of Chemical Research* 35:706-16

[215] Levy G, Schindel R, Kruth J .2003. Rapid manufacturing and rapid tooling with layer manufacturing (LM) technologies, state of the art and future perspectives. *Cirp Annals-Manufacturing Technology* 52: 589-609.

[216] Hutmacher D .2000. Scaffolds in tissue engineering bone and cartilage. *Biomaterials* 21: 2529-2543.

[217] Lewis J, Gratson G .2004. Direct writing in three dimensions. *Materials Today* 7: 32-39.

[218] Berman B .2012. 3-D printing: The new industrial revolution. *Business Horizons* 55: 155-162.

[219] Sherman L .2009. Additive manufacturing: New capabilities for rapid prototypes and production parts. *Plastics Technology* 55: 35-45.

[220] Cohen D, Malone E, Lipson H, Bonassar L. 2006. Direct freeform fabrication of seeded hydrogels in arbitrary geometries. *Tissue Engineering* 12: 1325-1335.

[221] Khalil S, Nam J, Sun W. 2005. Multi-nozzle deposition for construction of 3D biopolymer tissue scaffolds. *Rapid Prototyping Journal* 11: 9-17.

[222] Xu T, Binder K, Albanna M, Dice D, Zhao W. 2013. Hybrid printing of mechanically and biologically improved constructs for cartilage tissue engineering applications. *Biofabrication* 5.

[223] Wang D, Jayasinghe S, Edirisinghe M. 2005. Instrument for electrohydrodynamic print-patterning three-dimensional complex structures. *Rev Sci Instrum* 76.

[224] Han T, Reneker D, Yarin A. 2007. Buckling of jets in electrospinning. *Polymer* 48:6064-6076

[225] Chen C.H, Saville D.A, and Aksay I.A, Scaling laws for pulsed electrohydrodynamic drop formation, *Applied Physics Letters* 89: 124103 1-3

[226] Wang X, Zhao H, Turng L, Li Q. 2013. Crystalline Morphology of Electrospun Poly( $\epsilon$ -caprolactone) (PCL) Nanofibers, Industrial & Engineering Chemistry Research 52:4939-4949.

[227] Li J, Cai Y, Guo Y, Fuh J, Sun J, Hong G, Lam R, Wong Y, Wang W, Tay B, Thian E. 2014. Fabrication of three-dimensional porous scaffolds with controlled filament orientation and large pore size via an improved E-jetting technique, Journal of Biomedical Materials Research Part B: Applied Biomaterials 102 : 651-658.

[228] Flemming R, Murphy C, Abrams G, Goodman S, Nealey P. 1999. Effects of synthetic micro- and nano-structured surfaces on cell behavior, Biomaterials 20: 573-588.

[229] Park A, Cima L. 1996. In vitro cell response to differences in poly-L-lactide crystallinity, Journal of Biomedical Materials Research 31 :117-130.

[230] Cai S, Xu H, Jiang Q, Yang Y. 2013. Novel 3D Electrospun Scaffolds with Fibers Oriented Randomly and Evenly in Three Dimensions to Closely Mimic the Unique Architectures of Extracellular Matrices in Soft Tissues: Fabrication and Mechanism Study. Langmuir 29:2311-8

[231] McClure MJ, Sell SA, Simpson DG, Walporth BH, Bowlin GL. 2010. A three-layered electrospun matrix to mimic native arterial architecture using polycaprolactone, elastin, and collagen: A preliminary study. *Acta Biomaterialia* 6:2422-33